TROPOSPHERIC EMISSION SPECTROMETER (TES)

LEVEL 2 ALGORITHM THEORETICAL BASIS DOCUMENT

Version 1.99
June 30, 2004

Jet Propulsion Laboratory
California Institute of Technology
Pasadena, California

TROPOSPHERIC EMISSION SPECTROMETER (TES)

LEVEL 2 ALGORITHM THEORETICAL BASIS DOCUMENT

Reinhard Beer	Jet Propulsion Laboratory
Kevin W. Bowman	Jet Propulsion Laboratory
Patrick D. Brown	Atmospheric and Environmental Research Inc.
Shepard A. Clough	Atmospheric and Environmental Research Inc.
Annmarie Eldering	Jet Propulsion Laboratory
Aaron Goldman	University of Denver
Daniel J. Jacob	Harvard University
Michael Lampel	Raytheon
Jennifer A. Logan	Harvard University
Mingzhao Luo	Jet Propulsion Laboratory
Frank J. Murcray	University of Denver
Gregory B. Osterman	Jet Propulsion Laboratory
David M. Rider	Jet Propulsion Laboratory
Curtis P. Rinsland	NASA Langley Research Center
Clive D. Rodgers	University of Oxford
Stanley P. Sander	Jet Propulsion Laboratory
Mark Shepard	Atmospheric and Environmental Research Inc.
Susan Sund Kulawik	Jet Propulsion Laboratory
Eugene Ustinov	Jet Propulsion Laboratory
Helen M. Worden	Jet Propulsion Laboratory
John Worden	Jet Propulsion Laboratory

Approved by:
Reinhard Beer
TES Principal Investigator

Version 1.99
July 7, 2004

Jet Propulsion Laboratory
California Institute of Technology
Pasadena, California

This document was prepared at the Jet Propulsion Laboratory, California Institute of Technology, under a contract from the National Aeronautics and Space Administration

TABLE OF CONTENTS

THIS PAGE INTENTIONALLY LEFT BLANK.

I LIST OF ACRONYMS

ABSCO	Absorption coefficient
ADEOS	Advanced Earth Observing Satellite
AER	Atmospheric and Environmental Research Inc.
AERI	Atmospheric Emitted Radiation Interferometer
AES	Airborne Emission Spectrometer
AIRS	Atmospheric Infrared Sounder
ARM	Atmospheric Radiation Measurements
ASTER	Advanced Spaceborne Thermal Emission and Reflection Radiometer
ATBD	Algorithm Theoretical Basis Document
ATMOS	Atmospheric Trace Molecule Spectrometer
CAMEX	Convection and Moisture Experiment
CART	Cloud and Radiation Test (site)
CDC	Climate Diagnostics Center
CFC	chlorofluorocarbon
CHEM	Chemistry Mission (EOS third spacecraft)
CKD	Clough, Kneizys, and Davies
DAAC	Distributed Active Archive Center
DAO	Data Assimilation Office
DEM	Digital Elevation Model
ECMWF	European Center for Medium Range Weather Forecasting
ENVISAT	ESA Environmental Satellite
EOS	Earth Observing System
ETOPO5	Global digital elevation model on a 5-minute grid
FEV	fraction of explained variance
FFT	Fast Fourier Transform
FOV	field of view
GTOPO30	Global digital elevation model on a 30-arc second grid produced by the U. S. Geological Survey's EROS Data Center in Sioux Falls, South Dakota
HCFC	Hydrogenated Chlorofluorocarbon
HDF	Hierarchical Data Format
HFC	Hydrogenated Fluorocarbon
HIS	High resolution Interferometric Sounder
HITRAN	The molecular spectroscopic database
ILS	instrument line shape
IMG	Interferometric Monitor of Greenhouse Gases
ISAMS	Improved Stratospheric and Mesospheric Sounder
JPL	Jet Propulsion Laboratory
LaRC	Langley Research Center
LBLRTM	Line By Line Radiative Transfer Model
LIMS	Limb Infrared Monitor of the Stratosphere

LOS	line of sight
LRIR	Limb Radiance Inversion Radiometer
MIPAS	Michelson Interferometer for Passive Atmospheric Sounding
NASA	National Aeronautics and Space Administration
NAST-I	NPOESS Aircraft Sounder Testbed – Interferometer
NMC/NCEP	National Meteorological Center/National Center for Environmental Prediction
NOAA	National Oceanic and Atmospheric Administration
OD	optical depth
SCF	Science Computing Facility
TES	Tropospheric Emission Spectrometer
TOA	top of atmosphere
TOVS	TIROS N Operational Vertical Sounder
UARS	Upper Atmosphere Research Satellite
VMR	volume mixing ratio

II TES NOTATION AND STANDARD UNITS

General

Both symbols and units are given in the lists below. The first column is the unit to be used in code, and in files unless there is good reason to use other (well documented) units. If other units are used in files, the data should be converted to the recommended unit on input. SI under the heading *docs* means any conventional SI unit, with standard prefixes for powers of 10^3. Where no unit is given, the quantity is dimensionless.

		code & files	*docs*
Thermodynamics & mass distribution			
T	(level) temperature	K	SI
$\overline{T}$	layer mean temperature	K	SI
P	pressure	Pa	SI, hPa
$\overline{P}$	layer mean pressure	Pa	SI, hPa
P_m	partial pressure of gas g	Pa	SI, hPa
ζ	log pressure parameter		
ρ	(mass) density	kg m^{-3}	SI
H	pressure scale height	m	SI
g	acceleration due to gravity	m s^{-2}	SI
M_m	molar mass of gas g	kg $mole^{-1}$	SI
q_m	volume mixing ratio of gas g	fractional	*ppxv
$\overline{q}_m$	volume mixing ratio layer mean	fractional	*ppxv
			*x is m, b, t, etc.

Geometry

z	height	m	SI
r	radius from a center	m	SI
R_e	Earth radius to geoid	m	SI
R_c	Earth radius of curvature at geoid	m	SI
R_s	Earth center to satellite	m	SI
R_{cs}	Radius of curvature to satellite	m	SI
ψ	Angle at center of curvature between path element and tangent point	rad	deg
ψ_s	Angular position of satellite	rad	deg
ϕ	latitude	rad	deg
λ	longitude	rad	deg
θ	zenith angle of a ray	rad	deg
s	distance along ray	m	SI

Indexing

i	frequency index
j,k	level index
l	layer index

Levels indices are numbered 0 to N, bottom to top.
Corresponding layers are numbered from 1 to N

Spectroscopy

S	line intensity	cm^{-1} $molec^{-1}$ cm^2	cm^{-1} $molec^{-1}$ cm^2
$f(\nu)$	line shape	$1/cm^{-1}$	$1/cm^{-1}$
χ_ν	spontaneous emission line shape	$1/cm^{-1}$	$1/cm^{-1}$
ϕ_ν	absorption and stimulated emission line shape	$1/cm^{-1}$	$1/cm^{-1}$
ρ_n	number density	molec cm^{-3}	SI
$\tilde{C}_s, \tilde{C}_f$	self and foreign continuum functions	cm^{-1} $molec^{-1}$ cm^2 atm^{-1}	

[Warning: the units recommended here are not SI because the HITRAN data base is not in SI. Care must be taken when combining them with other quantities.]

Radiative Transfer

ν	wavenumber	cm^{-1}	cm^{-1}
n	refractive index		
L	spectral radiance	W m^{-2} sr^{-1}/cm^{-1}	*W m^{-2} sr^{-1}/cm^{-1}
$L^{\uparrow}$	up radiance, etc	W m^{-2} sr^{-1}/cm^{-1}	*W m^{-2} sr^{-1}/cm^{-1}
$\mathcal{F}$	flux	W m^{-2}/cm^{-1}	*W m^{-2} $/cm^{-1}$
B	Planck function	W m^{-2} sr^{-1}/cm^{-1}	*W m^{-2} sr^{-1}/cm^{-1}
J	source function	W m^{-2} sr^{-1}/cm^{-1}	*W m^{-2} sr^{-1}/cm^{-1}
τ_l	optical depth of layer l		
$\mathcal{T}_l$	transmittance of layer l		
τ_{ik}	optical depth of path from level i to level k		
$\mathcal{T}_{ik}$	transmittance of path from level i to level k		
u_l	layer amount (number)	molec m^{-2}	SI
u_{il}	column amount (number)	molec m^{-2}	SI
κ_g	absorption coefficient of gas g	m2 molec-1	SI
ε	emissivity		
α	albedo		
$\mathcal{R}_{BRDF}$	Bidirectional Reflectance Distribution Function		
Φ	Instrument line shape	1/cm-1	1/cm-1
R_{FOV}	Field of view function	rad-1	deg-1
r_ℓ, r_u	ratios of NLTE to LTE state populations		
g_ℓ, g_u	state degeneracies for upper and lower states		
n_ℓ, n_u	occupation numbers for upper and lower states		
Δ	LTE vibrational Boltzmann factor		
C_ν	Non-LTE correction function		
R_ν	Volumetric radiation function	W m^{-2} sr^{-1} $/cm^{-1}$	*W m^{-2} sr^{-1} $/cm^{-1}$
		* with SI-style prefix (□, m, etc)	

Retrieval

Matrices are upper case bold. Column vectors are lower case bold. Superscript T (e.g. A^T) indicates transpose

x	full state vector
	– $\mathbf{x}_c$ for constraint vector on full state grid
	– $\mathbf{x}_0$ for first guess
	– $\hat{\mathbf{x}}_i$ for i'th iteration
z	retrieval state vector
	-- $\mathbf{z}_c$ for constraint vector

– $\mathbf{z}_0$ for first guess
– $\mathbf{z}_i$ for i'th iteration

$\mathbf{y}$	measurement vector
$\mathbf{n}$	measurement error
$\mathbf{b}$	forward model parameters
$\mathbf{F}$	generic forward model
$\mathbf{S}$	covariance matrices. Subscript determines which.
	– $\mathbf{S}_n$ for the measurement error covariance matrix
	– $\mathbf{S}_a$ for the climatological covariance matrix
	– $\mathbf{S}_x$ for the error covariance matrix
	-- $\mathbf{S}_b$ for the systematic error covariance matrix
$\mathbf{K}$	Jacobian
$\mathbf{K}_z$	Jacobian on retrieval grid
$\mathbf{K}_b$	Jacobian of non-retrieved parameters
$\mathbf{M}$	mapping matrix
$\mathbf{A}_{xx}$	averaging kernel on full state grid
$\mathbf{G}_z$	gain matrix
Λ	constraint matrix
γ	Levenberg-Marquardt parameter
$\mathbf{I}_n$	unit matrix (order n optional)
$\mathbf{O}_n$	zero matrix (order n optional)
σ	standard deviation
z_r	correlation length
C	cost function

Physical constants

k_B	Boltzmann constant
c	speed of light
h	Planck constant
N	Avagadro constant
σ	Stefan-Boltzmann constant
c_1	First radiation constant
c_2	Second radiation constant
R	Molar gas constant

THIS PAGE INTENTIONALLY LEFT BLANK.

III LIST OF FIGURES

IV LIST OF TABLES

Error! No table of figures entries found.

THIS PAGE INTENTIONALLY LEFT BLANK

1 BACKGROUND

1.1 EXPERIMENT OBJECTIVES

The Tropospheric Emission Spectrometer (TES), selected for flight on the EOS AURA mission, will provide the first global view of the chemical state of the troposphere (the lowest region of the atmosphere, extending from the surface to about 10-15 km altitude). The investigation will focus on mapping the global distribution of tropospheric ozone and on understanding the factors that control ozone concentrations.

Ozone is produced in the troposphere by photochemical oxidation of carbon monoxide (CO) and hydrocarbons in the presence of nitrogen oxides (NO_x) and water vapor. These ozone precursors have both natural and anthropogenic sources. The chemistry of ozone is complex and tightly coupled to the atmospheric transport of both ozone and the precursors.

Tropospheric ozone has three major environmental impacts:

1) AS AN AIR POLLUTANT. Ozone in surface air is toxic to humans, animals and vegetation. It is the principal harmful component of smog.

2) AS A CLEANSING AGENT. Photolysis of ozone in the presence of water vapor is the primary source of the hydroxyl radical (OH), which is the main oxidant in the atmosphere. Reactions with OH in the lower and middle troposphere are the principal sink for a large number of environmentally-important species including air pollutants (carbon monoxide), greenhouse gases (methane), and gases depleting the stratospheric ozone layer (HCFC's, methyl halides).

3) AS A GREENHOUSE GAS. Ozone in the middle and upper troposphere is an efficient greenhouse gas. Perturbation of ozone in this region of the atmosphere results in heterogeneous radiative forcing with complicated implications for climate.

The troposphere contains only about 10% of the total ozone in the atmosphere -the bulk is in the stratosphere. The environmental implications of tropospheric ozone are very different from those of stratospheric ozone. The ozone layer in the stratosphere shields the Earth's surface from solar UV-B radiation, and thinning of this layer as a result of human activities is a matter of grave concern. Tropospheric ozone, by contrast, has increased as a consequence of human activity (primarily because of combustion processes). Whether this increase in tropospheric ozone is beneficial (cleansing agent) or harmful (air pollutant, greenhouse gas) depends to a large extent on its altitude. It is very important, therefore, to map the global 3-dimensional distribution of tropospheric ozone and its precursors in order to improve our understanding of the factors controlling ozone in different regions of the troposphere.

The specific Standard Products that TES will produce are global-scale vertical concentration profiles (0 - ~33 km) of ozone, water vapor, carbon monoxide, methane and nitric acid (the latter in the mid- and upper troposphere only). Essential by-products of the analysis are atmospheric temperature profiles and surface temperature and emissivity.

1.2 RELEVANCE TO EARTH SYSTEM SCIENCE

One of the primary EOS themes is 'Atmospheric Ozone Research.' TES directly addresses this theme.

1.3 INSTRUMENT CHARACTERISTICS

TES is an infrared, high resolution, Fourier Transform spectrometer covering the spectral range 650 - 3050 cm^{-1} (3.3 - 15.4 μm) at a spectral resolution of 0.1 cm^{-1} (nadir viewing) or 0.025 cm^{-1} (limb viewing). The two observation modes are essential because many of the spectral features that TES observes are very weak and limb-viewing markedly enhances their measurability (with the deficiency that cloud interference is much more likely than in nadir viewing, where TES has relatively good spatial resolution).

In order to improve signal-to-noise ratio and improve collection efficiency, TES is (as far as possible) radiatively cooled to ~180K, and it divides the spectral range into 4 sub-regions, each observed with a separate 1x16 array of detectors (identified as 1A, 1B, 2A, and 2B) actively cooled to 65K. The bandwidth is further restricted to ~250 cm^{-1} by interchangeable filters. With these arrays, 16 altitudes in the troposphere and lower stratosphere are observed simultaneously with a height separation of 2.3 km or, alternatively, 16 contiguous areas (each 0.5 x 5 km) are observed on the ground. Table 1-1 shows the available filter ranges and their identifiers. A complete description of TES can be found as an appendix to the L1B ATBD [JPL D-16479, Oct.1 1999].

Table 1-1: TES Filter Bandpasses (nominal)

Filter ID	Lower 50% Point, cm^{-1}	Upper 50% Point, cm^{-1}
1A1	1900	2250
1A2	2200	2450
1A3	2425	2650
1A4	2600	2850
1A5	2800	3050
1B1	820	1050
1B2	950	1150
2A1	1100	1325
2A2	1300	1550
2A3	1500	1750
2A4	1700	1950
2B1	650	900

Note: Any combination of 1Ax, 1By, 2Az and 2B1 is allowable (1 per detector array) with the proviso that, normally, only limited switching among 1Ax and 2Az filters can occur between successive scans. The actual arrangement of the filters in the filter wheels has been optimized for expected observation scenarios.

The filters actually employed for the Global Surveys are shown in Table 1-2. Sequences "A" and "B" alternate every 81.9 seconds for 16 orbits (~1 day) for a total of 1152 sequences (= number of profile sets). Note also that the pairs of nadir observations in each sequence are co-located.

Table 1-2: TES Global Survey Filters

Sequence	Scan No.	Type	Array 1A	Array 1B	Array 2A	Array 2B
A	1	Space	1A1	1B1	2A1	2B1
A	2	Black Body	1A1	1B1	2A1	2B1
A	3	Nadir	1A1	1B2	2A1	2B1
A	4	Nadir	1A1	1B2	2A1	2B1
A	5	Limb	1A1	1B1	2A1	2B1
A	6	Limb	1A1	1B2	2A4	2B1
A	7	Limb	1A1	1B2	2A4	2B1
B	1	Space	1A1	1B2	2A2	2B1
B	2	Black Body	1A1	1B2	2A2	2B1
B	3	Nadir	1A1	1B2	2A1	2B1
B	4	Nadir	1A1	1B2	2A1	2B1
B	5	Limb	1A1	1B1	2A2	2B1
B	6	Limb	1A1	1B2	2A4	2B1
B	7	Limb	1A1	1B2	2A4	2B1

In the limb mode, TES measures the infrared thermal emission from the atmosphere. In the nadir mode, the measurement is of the surface emission, downward directed atmospheric emission scattered from the surface, and further emission and absorption by the atmosphere. In a limited spectral range, under sunlit conditions, there may also be solar radiation scattered from the atmosphere and the surface.

TES obtains its data in 4 seconds (nadir) or 16 seconds (limb) plus calibrations in a sequence: 2 calibrations followed by 2 nadir observations followed by 3 limb observations. The entire cycle requires 81.9 seconds and is repeated continuously every other day, interspersed with major calibration-only sequences (essential for this type of instrument) and occasional targets-of-opportunity such as volcanic eruptions, biomass burning regions or regional ozone episodes for which TES has unique capabilities (but note that these are Special, not Standard, Products and are not further considered in this document).

It is a property of a Fourier Transform Spectrometer that it must be used in a so-called 'staring' mode (that is, the target location or altitude must be tracked). Accordingly, TES is equipped with a precision pointing system.

1.4 STANDARD PRODUCTS

TES Standard Products (and their data sources) are shown in Table 1-3.

Table 1-3: TES Standard Products

Product	Nadir	Limb
Atmospheric Temperature, T	√	√
Surface Temperature, T_s	√	
Ozone (O_3) VMR	√	√
Water Vapor (H_2O) VMR	√	√
Carbon Monoxide (CO) VMR	√	√
Methane (CH_4) VMR	√	√
Nitric Acid (HNO_3) VMR		√

Standard Products will be reported at the pressure levels shown in Table 1-4 (note that the corresponding altitudes are approximate). Nadir and limb data are nearly co-located.

Each output file will be accompanied by a header containing information such as the time, date, latitude, longitude, and solar zenith angle at acquisition, plus a set of data quality indicators (such as the averaging kernels).

Table 1-4: TES Product Reporting Levels [= UARS Standard Levels]

Index	Pressure hPa	US S.A. Altitude km	Delta Altitude km
0	1000.0	0.100	
1	681.3	3.175	3.075
2	464.2	6.100	2.925
3	316.2	8.825	2.725
4	215.4	11.350	2.525
5	146.8	13.800	2.450
6	100.0	16.200	2.450
7	68.1	18.650	2.450
8	46.4	21.100	2.500
9	31.6	23.600	2.500
10	21.5	26.100	2.500
11	14.7	28.600	2.600
12	10.0	31.200	2.600
13	6.8	33.800	2.600
14	4.6	36.600	2.800

"Delta Altitude" at level *i* is the difference between Level *i* and Level *i*-1

1.5 SPECIES INCLUDED IN RETRIEVALS

In order to retrieve the Standard Products listed in Table 1-3, it is necessary to account for many more species in the process. These are often called "interferents" but, in fact, some will be retrieved as controls (e.g., N_2O), some flagged for Special Processing (e.g., heavy hydrocarbons) and some fixed. For example, in order to retrieve HNO_3, it is essential to include both CCl_3F (CFC11) and CCl_2F_2 (CFC12) whose bands overlap the nitric acid signature.

The primary source of spectral information is the HITRAN database [Rothman *et al.*, 1998]. Not all of the species in the list are pertinent to TES but those that are, are shown in Table 1-5 (line data) and Table 1-6 (cross-section data). In addition, some modifications and additions to the list are discussed elsewhere in this document and it should be noted that certain isotopomers *must* be treated as separate molecules because their concentrations relative to the parent are known to be height-variable (HITRAN assumes a fixed ratio). Finally, Table 1-7 lists some species that are likely to be important to TES but for which little or no useful spectral data are available (i.e., they are candidates for laboratory study in the very near future).

Table 1-5: HITRAN Line List Species Used by TES

HITRAN [TES] Index No.	Molecule	Comments
1	H_2O	HDO & $H_2{}^{17}O$ Separated
[1a]	HDO	
[1b]	$H_2{}^{17}O$	
2	CO_2	
3	O_3	$^{16}O^{17}O^{16}O$ & $^{17}O^{16}O^{16}O$ Separated
[3a]	$^{16}O^{17}O^{16}O$	

HITRAN [TES] Index No.	Molecule	Comments
[3b]	$^{17}O^{16}O^{16}O$	
4	N_2O	
5	CO	
6	CH_4	CH_3D Separated
[6a]	CH_3D	
7	O_2	
8	NO	
9	SO_2	
10	NO_2	
11	NH_3	
12	HNO_3	
13	OH	
14	(HF)	** Not Used **
15	HCl	
16 **	(HBr)	** Not Used **
17 **	(HI)	** Not Used **
18	ClO	
19	OCS	

HITRAN [TES] Index No.	Molecule	Comments
20	HCOH	
21	HOCl	
22	N_2	
23	HCN	
24	CH_3Cl	
25	H_2O_2	
26	C_2H_2	
27	C_2H_6	
28 **	(PH_3)	** Not Used **
29	COF_2	
30	SF_6	Also need X-sections
31	H_2S	
32	HCOOH	
33 **	(HO_2)	** Not Used **
34 **	(O)	** Not Used **
35	$ClONO_2$	Also need X-sections
36 **	(NO+)	** Not Used **
37 **	(HOBr)	** Not Used **

Table 1-6: HITRAN Cross-Section Species Used by TES

Molecule	Common Name
CCl_4	Carbon Tetrachloride
CCl_3F	CFC-11
CCl_2F_2	CFC-12
$CClF_3$	CFC-13
CF_4	CFC-14
$CHCl_2F$	HCFC-21
$CHClF_2$	HCFC-22
$C_2Cl_3F_3$	CFC-113
$C_2Cl_2F_4$	CFC-114
C_2ClF_5	CFC-115
N_2O_5	Dinitrogen Pentoxide
HO_2NO_2	Peroxynitric Acid*
SF_6	Sulfur Hexafluoride
$ClONO_2$	Chlorine Nitrate

* Seriously incomplete

Table 1-7: Additional Cross-Section Species Needed by TES

Molecule	Common Name
C_6H_6	Benzene
C_2H_4	Ethylene
C_3H_8	Propane
$CH_3C(O)CH_3$	Acetone
CH_3OH	Methyl Alcohol
$CH_3C(O)NO_2$	Peroxyacetyl Nitrate (PAN)
HO_2NO_2	Peroxynitric Acid*
CH_3COOH	Acetic Acid
CH_3OOH	Methyl Hydroperoxide

* For bands not in HITRAN

2 ALGORITHM VERIFICATION

2.1 END-TO-END CLOSURE EXPERIMENTS

The purpose of the end-to-end closure experiments using the TES reference and operational software is to test the robustness of TES level 2 retrieval algorithms and the operational software and to identify any problems either in the algorithm or in coding. This procedure will also be helpful for algorithm validations. A single step end-to-end simulation would be to add noise to the model radiance and then to execute a step retrieval defined in the TES retrieval strategies. A full end-to-end closure experiment would be to generate a full one-day global survey set of radiances with added noise and clouds and then to carry out the one-day retrieval processing.

Establishing a profile/parameter database which consists collections of measured atmospheric temperature and constituent profiles and surface parameter data by all means of observations, sonde, balloon, aircraft, satellite, etc. is one of the key activities for the pre-launch closure experiments. These profiles/parameters along with model simulated profiles allow us to compile the baseline initial guesses and the *a priori* (see sections 3.5.3 and 3.5.4), to simulate the observed spectral radiance, and to evaluate the retrieval results for all the possible atmospheric conditions including extreme cases. Global cloud coverage data will also be obtained so that the simulated TES global pixel measurements will be more realistic.

The end-to-end closure experiments will follow three procedures: (1) simulate the TES observations using collected measurement profiles/surface parameters/cloud coverage as the true atmospheric full state with added noise, (2) generate TES retrieval products using a defined initial guess, and (3) examine and evaluate the retrieval results and error analysis by comparing with the "smoothed true profiles" and their statistical variance. Since the level 2 software will be developed in steps from a single profile retrieval to automated four-day data retrieval, the end-to-end experiment can be performed at each step.

2.2 VALIDATION

Validation, in the sense used here, differs from validation of the TES measurements in that we will use pre-existing data that have already been analyzed by others. The objective is to ensure that the TES algorithm either produces identical results or there are plausible reasons why it does not. Measurement validation will employ near-concurrent and co-located measurements and is not further discussed in this document (although, of course, it is a crucial part of the overall TES experiment).

Data sources currently identified that are (or will be) appropriate for this purpose are

1) Airborne Emission Spectrometer (AES). AES operated in both a downlooking mode from a variety of aircraft and uplooking from the surface. It was specifically designed to cover the same spectral region at the same resolution as TES and is therefore a prime data source for validation exercises. Downlooking data are very similar to the TES nadir mode and uplooking data are a useful surrogate for TES limb data.

2) AERI (Atmospheric Emitted Radiation Interferometer). AERI is a well calibrated, 1 cm^{-1} spectral resolution, uplooking , Michelson interferometer covering the range 550 to 1700 and 2000 to 2500 cm^{-1}. Several copies of the instrument are operational – the one of primary interest for TES validation is located at the Central facility of the ARM Cloud And Radiation Test (CART) site in northern Oklahoma. The AERI-X (eXtended resolution AERI) is also located at the central facility. It has 0.1 cm^{-1} spectral resolution, but only covers 550 to 1600 cm^{-1}. The ARM program provides good temperature and water vapor information about the atmosphere overhead. Information about ozone and other stratospheric gases, as well as aerosol optical depth, is available from solar absorption instruments at the site.

3) HIS (High Resolution Interferometric Sounder). HIS is an autonomous FTS that flies on the ER2 in a variety of campaigns with the goal of temperature and water vapor sounding. Some of the more recent campaigns have been in support of tropospheric chemistry missions, where independent measurements may also be available. Although the spectral resolution is lower, the data are from an altitude that is more "space-like" than the AES data.

4) IMG (Interferometric Monitor of Greenhouse Gases). IMG, a nadir sounder developed by the Japanese, flew on the ADEOS mission (which failed in June 1997). Nevertheless, it represents the only available source of real space-based nadir-viewingdata with spectral coverage and resolution very close to that of TES. Some tests using IMG data are already ongoing and more are planned.

5) MIPAS (Michelson Interferometer for Passive Atmospheric Sounding). MIPAS was launched on the ENVISAT mission in 2002. It is a limb sounder with slightly poorer spectral resolution than TES but is nevertheless the only available source of space-based limb emission data prior to TES, so it will is a very valuable validation tool.

6) NAST-I (NPOESS Aircraft Sounder Testbed – Interferometer). NAST-I is a nadir-viewing instrument that has flown on several ER2 missions, including CAMEX-3, with correlative radiosonde measurements. It has a spectral resolution of 0.25 cm^{-1} covering the spectral regime 590-2810 cm^{-1}. As a testbed to the NPOESS candidate instruments, it has been used to simulate "space-like" ground coverage views for the validation of key meteorological species.

3 ALGORITHM DESCRIPTION

3.1 ALGORITHM OVERVIEW

TES standard data processing falls naturally into 3 groups:

1) At Level 1A the raw data from the spacecraft are decommutated and the instrument outputs (called *interferograms*) reconstructed. File headers also contain important ancillary data such as time, date, spacecraft and target location, and instrument pointing. The target location is determined by a geolocation algorithm at Level 1A that uses the instrument pointing and spacecraft coordinates along with the Digital Elevation Model (DEM) and earth ellipsoid and geoid models.

2) At Level 1B, the interferograms are converted to spectra, radiometrically-calibrated and resampled onto a common frequency grid. Certain data quality flags are added to the header at this juncture and the results passed to Level 2 [JPL D-16479, 1999].

3) At Level 2, vertical concentration profiles of the selected species are extracted from the data through the process of *retrieval* that is the topic of this document.

Although this document is primarily concerned with standard products, we also expect to use the same algorithm for special products so we have retained generality in some sections to support these additional functions. This additional functionality will be maintained in the Reference Forward Model. We therefore describe the deliverable version as the Operational Forward Model.

Figure 3-1 shows an overall flow chart for the forward model and retrieval process.

In Global Survey mode, observations are made in sequences made up of calibration scans, two nadir observations and three limb observations. Observation sets may be binned together to be processed in batches containing all observations made each day at the same time after an equator crossing, i.e. at the same latitude. This would enable savings to be made in disk accesses for quantities that depend on latitude only. This includes climatological information used for the first guess and *a priori* information, which are likely to be zonally averaged.

Each observation set will be retrieved in several stages, with each stage using a selection of the results of a previous stage as *a priori,* or as a first guess, or as updated forward model parameters, as appropriate. For example, in both the nadir and the limb retrievals, temperature could be retrieved first, and the results used as forward model parameters for constituent retrievals. Although we will perform the retrievals using spectral ranges (referred to as 'microwindows') that are selected to minimize the errors from 'interferent' species on the retrieved parameters, we must still account for these interferents. Thus, the constituent retrievals will be carried out in an appropriate order so that an already retrieved quantity can be included as a forward model parameter ('interferent') for subsequent retrievals. Some quantities may be retrieved jointly. In particular, the final profile for the temperature and water vapor fields will be obtained from a joint retrieval.

Each retrieval will use the same inverse algorithm comprising the following stages:

(1) Full state vector construction for generating the forward model, including initial guess for retrieved parameters
(2) *a priori* vector and covariance, or other constraint construction;
(3) optimal estimate by numerically minimizing a cost function.
(4) error estimate for retrieved parameters

The optimal estimate will be obtained by a nonlinear least squares process with constraints. It will minimize a cost function, which includes contributions from both the departure of the measured spectrum from the calculated spectrum and the departure of the retrieved state from constraints imposed through the *a priori* state. (The *a priori* is not in general the same as the first guess, which is a state selected as a starting point for a non-linear iteration). An appropriate subset of the measured spectrum will be used for each parameter retrieved. This may comprise a microwindow or a large segment of spectrum.

Finally, the complete spectrum will be calculated for quality control. At this point, the atmosphere will be determined as well as possible, but the individual retrievals will not have covered the complete spectrum, so there will be gaps in the surface emissivity (nadir case) or aerosol optical depth (limb case). This necessitates a final retrieval using the entire spectrum, with fixed atmospheric parameters. The results will be the desired spectra, along with spectra of the surface emissivity or aerosol optical depth as by-products.

The optimal estimation process requires a numerical model to generate the spectrum expected for a particular atmospheric condition. Below, we describe the parameters necessary to carry out the calculation (3.2), the forward model (3.3), and the derivatives of the spectrum with respect to the desired parameters (3.4). The actual retrieval process is detailed in 3.5.

3.1.1 TES Retrieval Algorithm: Earth Limb and Nadir Operational Retrieval (ELANOR)

Most of the algorithm elements discussed in this document have been coded and tested at the TES SCF in the TWPR (TES Working Prototype Retrieval Algorithm) and now ELANOR, which is the operational retrieval code designed based on TWPR. Prototyping efforts continue to test the speed and accuracy of ideas as they are put forward by the members of the Science Team. The retrieval algorithm is validated using simulated data as discussed in chapter 4.0, and whenever possible, using real data from AES (Airborne Emission Spectrometer), HIS (High Resolution Interferometer Sounder) and IMG (Interferometric Monitor of Greenhouse Gases). These instruments all have spectral resolution and coverage similar to TES, albeit nadir viewing only. When MIPAS (Michelson Interferometer for Passive Atmospheric Sounding) limb data become available, they will be used for the same purpose. It is our intention to continue improving ELANOR, with releases that meet pre-launch testing needs, at launch requirements and post-launch adjustments or added capabilities.

Figure 3-1: TES Level 2 Retrieval Flow

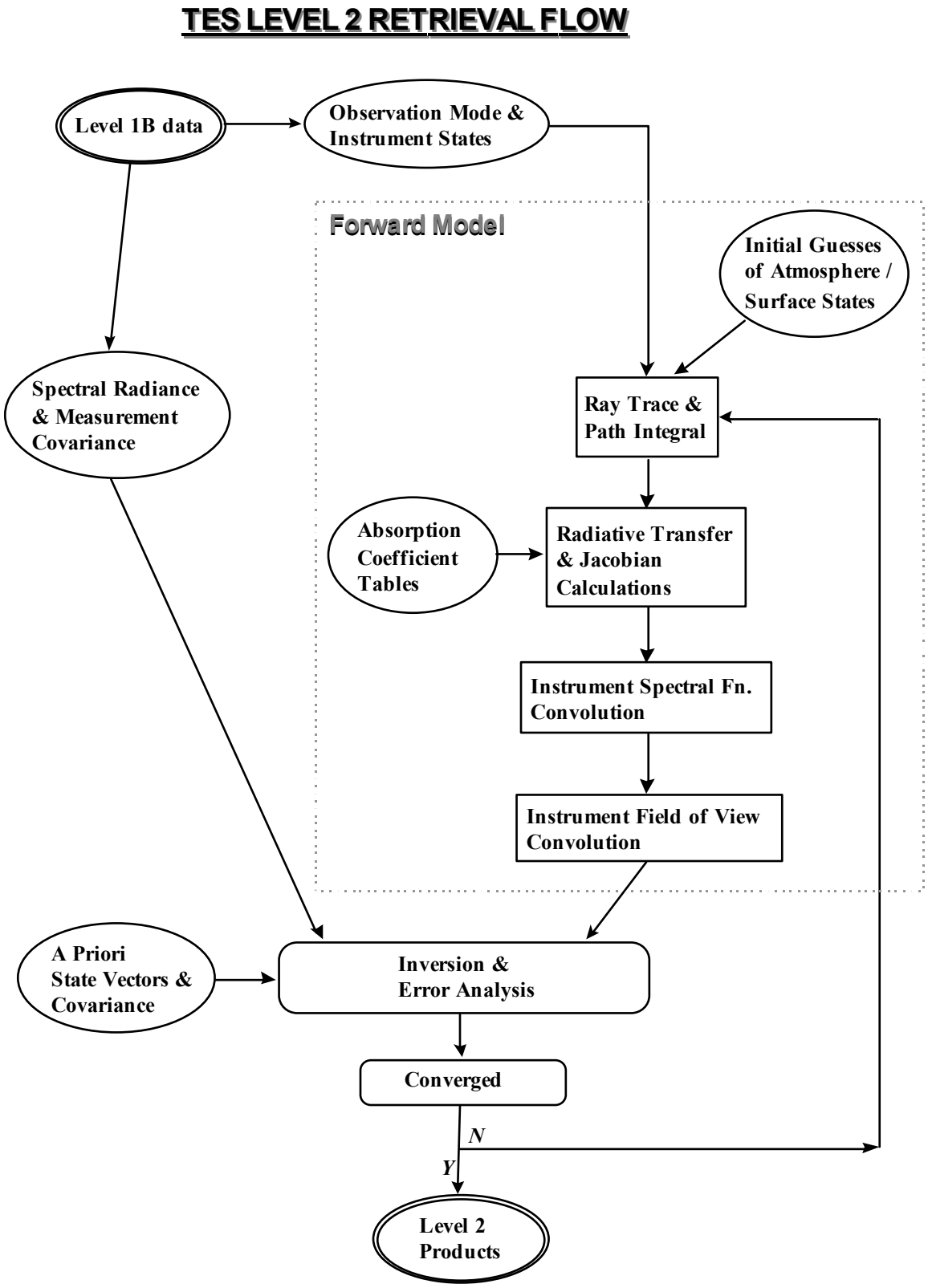

3.2 STATE VECTORS

3.2.1 Terminology

A *state vector* specifies those aspects of the state of the atmosphere being measured, and of the instrument measuring it, which together determine the value of the resulting measurement. We will use the term *full state vector* to indicate the complete set of parameters required by the forward model (Section 3.3) to simulate a measurement to the necessary accuracy, and the term *retrieval state vector* or simply *retrieval vector* to indicate the subset of the full state vector that is a target for retrieval. The remaining elements will either be predetermined (*forward model parameters*) or be determined by interpolation where the forward model requires a finer grid for numerical purposes.

3.2.2 Full State Vector Elements

The following elements comprise the full state vector for calculating nadir radiance:

- surface pressure
- temperature on a specified pressure grid
- constituent mixing ratios on a specified pressure grid
- aerosol extinction coefficients on specified pressure and wavenumber grids
- surface radiating temperature
- surface optical properties corresponding to each detector element on a specified wavenumber grid:
  - emissivity
  - albedo/reflectivity
  - bi-directional reflectivity distribution function
- nadir view angle
- nadir view location
- sun angle at the nadir location
- instrument line shape
- field of view function

The following elements comprise the full state vector for calculating limb radiance:

- temperature on a specified pressure grid
- constituent mixing ratios on a specified pressure grid
- aerosol extinction coefficients on specified pressure and wavenumber grids
- spacecraft position
- look angle of the boresight from the spacecraft
- sun angle at the tangent point location
- altitude of one pressure level
- instrument line shape
- field of view function

In this we assume that the atmosphere is hydrostatically balanced and radially symmetric. For the limb view, it may be necessary to include some representation of horizontal gradients of some of the elements.

There are several other quantities that should formally be part of the full state vector, but are best considered as constants, and treated separately by the forward model. These include

- Constituent absorption coefficients on a wavenumber, pressure and temperature grid.
- Digital elevation model
- Surface characterization map (Global land cover database)

3.2.3 Pressure Level Grids

The natural vertical grid for nadir forward model is based on pressure levels, as this is one in which the Jacobeans have a particularly simple form. In order to combine results from the nadir and limb views, both must be on compatible grids, so this choice requires us to use a pressure grid for the limb view as well. We have chosen to use log(P) as the basic vertical coordinate, and to make the grid spacing compatible with that established for UARS.

The full state vector will be defined on the *full grid*, which is a superset of the retrieval grid:

$$\log_{10}(P_i) = 5 - i/6m \qquad (3.1)$$

where P_i is the pressure in pascals of level index i and the `superset factor' m is an integer. The UARS grid corresponds to m=1, with a spacing of 6 levels per decade of pressure. The value of m will be determined by the accuracy requirements of the numerical method, and may vary with height.

The pressure grids for the retrieved state vectors will be subsets of those for the full state. The elements of the retrieval state vector that comprise profiles will be defined on a *retrieval grid*,

$$\log_{10}(P_i) = 5 - i/6n \qquad (3.2)$$

The value of n will be a submultiple of m, chosen so that the full information content of the measurements can be represented. The range of levels used will vary with the quantity retrieved. The choice of the retrieval pressure levels for each TES product molecule and temperature are key investigation activities which involve the physical constraints used for profile retrieval and the trade-offs between the retrieval vertical resolution and the product accuracy.

Values of the profiled quantities between retrieval grid levels will be determined by the following interpolations:

(1) Temperature is linearly interpolated in log(P).
(2) Logarithms of constituent mixing ratios and aerosol extinction coefficients are interpolated and extrapolated linearly in log(P), and linearly extrapolated above the top level at the same gradient as in the top layer.

As an example, for the full state vector of the prototype forward we have constructed an 86-layer atmosphere model for simulations and for the absorption coefficient table pressure and temperature grids. This 86-layer atmosphere has 87 pressure levels between about 1211.53 hPa and 0.1 hPa. The pressure levels (in hPa) are defined up to 1 hPa as

$$P_k = 1000 \times 10^{-(k-2)/24} \quad k = 0 \ldots 74; \tag{3.3}$$

and above 1 hPa as

$$P_k = 1000 \times 10^{-(k-38)/12} \quad k = 75 \ldots 86; \tag{3.4}$$

In the troposphere, the layer thickness calculated using hydrostatic equation and for US standard atmosphere is about 0.83 km (surface) to 0.6 km (tropopause). Between 100 hPa and 1 hPa, the layer thickness is about 0.6-0.8 km; while above 1 mb, it is about 1.5 km.

3.2.4 Spectral Grids

The spectral grid for the monochromatic radiative transfer calculations over the spectral domain associated with a specific filter is determined by the mean Doppler width at the top of the atmosphere. Studies of the dependence of errors in radiative transfer on spectral sampling indicate that for pressure broadened lines, a sampling grid of four points per Lorentz halfwidth is required, [Clough and Kneizys, 1979]. Extension of this analysis to the Doppler and Voigt line shapes leads to essentially the same conclusion. The spectral sampling based on this criterion, in addition to being appropriate for the stratosphere, provides proper spectral sampling of the narrow water lines in the atmospheric window regions and of the line coupling effects of the carbon dioxide Q branches in the pressure broadening regime. Because the spectral grid is based on the Doppler width, the grid, though fixed for a given filter, is frequency dependent by filter (coarser at higher wavenumber values).

Based on studies of computational efficiency and accuracy, a decision has been made to utilize a fixed spectral grid over the domain of a given filter. Use of a fixed spectral grid also facilitates the computation of the forward model radiances and Jacobians by allowing the computation to be easily sub-divided into small spectral “chunks” that can fit in the memory of off-the-shelf computers. Two sets of absorption coefficient files have been computed, (1) a “fine” spectral grid that can sample lines at the top of the atmosphere in our 87-level forward model atmosphere at four points per half-width and (2) an operational grid that, for now, is at half the resolution of the fine grid. The operational grid absorption coefficient tables are computed by convolving a 3-point triangular filter with the fine-grid tables. We find that the radiances computed using this operational grid are accurate to within 0.001% as compared to the radiances computed using the fine spectral grid. Table 3-1 describes the operational spectral grid for each filter.

Table 3-1: Operational spectral grid for TES filters

Filter ID	Lower 50% Point, cm^{-1}	Upper 50% Point, cm^{-1}	Operational Spectral Grid (cm^{-1})	Reference Grid (cm^{-1})
1A1	1900	2250	0.0008	0.0004
1A2	2200	2450	0.0008	0.0004
1A3	2425	2650	0.0008	0.0004
1A4	2600	2850	0.0008	0.0004
1A5	2800	3050	0.0008	0.0004
1B1	820	1050	0.0004	0.0002
1B2	950	1150	0.0004	0.0002
2A1	1100	1325	0.0004	0.0002
2A2	1300	1550	0.0004	0.0002
2A3	1500	1750	0.0004	0.0002
2A4	1700	1950	0.0004	0.0002
2B1	650	900	0.0002	0.0001

State vector elements specified on other spectral grids are interpolated by a four-point Lagrangian to the operation spectral grid. Nominal values of other spectral grid spacings are:

- Heavy molecules (e.g., CFC's) 0.0025 cm^{-1}
- H_2O, N_2, and O_2 continua 0.1 cm^{-1}
- Clouds and aerosols 1 cm^{-1}
- Surface emissivity 10 cm^{-1}
- Surface albedo/reflectivity 10 cm^{-1}
- Surface bi-directional reflectivity distribution function 10 cm^{-1}

3.3 FORWARD MODEL: ATMOSPHERE

3.3.1 Radiative Transfer

The spectral radiance received by TES can be expressed by the radiative transfer equation. Under clear conditions, the radiance received in a downlooking mode includes four contributions: upwelling atmospheric emission, attenuated reflected downwelling atmospheric emission, attenuated surface emission and attenuated reflected solar radiation. In order to show the influence of the sensor on the signal, the radiance must be convolved with the absolute instrument line shape (ILS). For a single ray, we obtain Equation (3.5):

$$L(\Omega,\nu)=\int_0^{\infty}\Phi(\nu,\nu')\left\{\int_{z_0}^{\infty}B(\nu',T(z))\frac{\partial\mathcal{T}(\Omega,z,z_0,\nu')}{\partial z}dz\right.$$

(Instrument) *(Upwelling atmospheric emission term)*

$$+\alpha(\nu')\cdot\mathcal{T}(\Omega,z_0,\infty,\nu')\int_{2\pi}\mathcal{R}_{BRDF}(\Omega,-\Omega',\nu')\int_{\infty}^{z_0}B(\nu',T(z))\frac{\partial\mathcal{T}(-\Omega',z,z_0,\nu')}{\partial z}dz\,d\Omega'$$

(*Downwelling*, *back – reflected*, *atmospheric emission term*)

$$+\varepsilon(\Omega,\nu')\cdot B(\nu',T_{surf})\cdot\mathcal{T}(\Omega,z_0,\infty,\nu')$$

(*Surface emission term*)

$$\left.+\alpha(\nu')\cdot\mathcal{R}_{BRDF}(\Omega,-\Omega_0,\nu')\cdot E_s(\nu')\cdot\Omega_s\cdot\mathcal{T}(-\Omega_0,\infty,z_0,\nu')\cdot\mathcal{T}(\Omega,z_0,\infty,\nu')\right\}d\nu'$$

(Reflected sunlight term)

(3.5)

where

$L(\Omega,\nu)$ = radiance at frequency ν into upward, directed, solid angle Ω
$\Phi(\nu,\nu')$ = ILS, i.e. spectral response at frequency ν due to incident radiance at ν'
$B(\nu,T)$ = Planck function for temperature T at frequency ν
T_{surf} = surface (skin) temperature
$\mathcal{T}(\Omega,z,z',\nu')$ = atmospheric transmittance at frequency ν' in a direction Ω between altitudes z and z'
$\alpha(\nu')$ = surface albedo at frequency ν'
$\mathcal{R}_{BRDF}(\Omega,-\Omega',\nu')$ = surface biconical reflectance function for incident (downward) solid angle $-\Omega'$ and emergent (upward) solid angle Ω
$\varepsilon(\Omega,\nu')$ = surface emittance at frequency ν' into solid angle Ω
$E_s(\nu')$ = disk-average solar radiance at frequency ν'
Ω_s = solar solid angle at Earth

The same equation holds for limb emission sounding if the last three (surface-related) terms are omitted. While the equation, therefore, seems much simpler, the geometry of the light path (especially in the lower atmosphere) becomes much more complicated because of significant refraction effects.

In the next section, a numerical radiative transfer model that was developed for TES will be described. This *forward model* uses atmospheric temperature and constituent profiles and the surface properties as inputs. The integrations in Equation (3.5) are carried out numerically by dividing the atmosphere into thin layers (by pressure). The layer effective quantities, such as the layer effective temperature and pressure and the layer molecular column amount, are calculated

in the ray tracing and path integrals step.

3.3.1.1 Ray Tracing and Path Integrals

The lines of sight through the atmosphere must be traced, allowing for the detailed geometry and possible refraction effects. Full details will be found in Appendix 3.3.1.1. The basic principles are described here.

The non-sphericity of the Earth is accommodated by using a coordinate system with origin at the center of curvature, at a nominal tangent point, of a reference geoid. In the plane of the ray (refraction horizontally is ignored) the atmosphere is described in terms of functions of radius r and angle ψ of the line from the center to the ray element. Quantities in a radially symmetric atmosphere are assumed to be independent of ψ.

For integrating the hydrostatic equation, a full latitude/altitude model is used for the variation of the acceleration of gravity. The air density is calculated from an equation of state that includes the effect of water, and is not simplified to the perfect gas law. (Appendix 3.3.1.1.7)

For the quasi-nadir case, the ray tracing is evaluated from simple trigonometry, ignoring refraction. Integrals of absorber amounts and temperature are carried out analytically over full grid layers, assuming that $\ln(q)$ and T are linear in $\ln(P)$. This is a change.

For the limb case, the approach used is based on that of Kneizys *et al.*(1983). The coordinate $x = r\cos\theta$ is used along the ray to avoid the singularity at the tangent point. The zenith angle of the ray, θ, is obtained from Snell's law for spherical symmetry, $rn(r)\sin\theta(r)$ = constant, and the distance element ds along the ray is related by $dr = \sin\theta\, ds$. This can be shown to give

$$ds = dx/[1+(r/n)(\partial n/\partial r)\sin^2\theta(r)] \qquad (3.6)$$

which can be used to integrate path integrals with respect to x, an explicit function of r, rather than s. The integrals are evaluated by dividing each full grid layer into sub-layers in x, such that all quadrature intervals are smaller than a given length, and using a trapezium or higher order quadrature.

When the atmosphere is not radially symmetric, the above ray tracing technique does not apply because we can no longer assume that $nr\sin\theta$ = constant. In this case we can use a more general approach and construct a set of three coupled ordinary differential equations in $r(s)$, $\theta(s)$ and $\psi(s)$ to describe the ray trajectory. These are integrated forwards from an assumed tangent point to the satellite altitude. The horizontal location of the tangent point as expressed by $\psi(0)$ is then iterated so that the ray reaches the location of the satellite. Path integrals are evaluated in the same way as for the radially symmetric case, but using the same quadrature points in s as are used by differential equation integration.

3.3.1.2 Ray Tracing (Surface Layer)

The pressure boundaries of the forward model atmospheric layer above the Earth's surface must be redefined for every TES observation. This layer will be thinner than or equal to the TES

standard forward model layers near the surface**.** The sea surface pressure will be obtained from fields obtained from available meteorological data (Section 3.5.2.2). The earth surface pressure (the lower pressure boundary for the surface layer) will be calculated from the sea surface pressure using the hydrostatic equation at the TES identified elevation (Section 3.3.2.2).The top pressure boundary for the surface layer will be a TES fixed pressure level.

3.3.1.3 Simultaneous Multiple Rays

The angular radiation field measured by the TES detectors is discretized with a bundle of rays that span the TES field-of-view. Each ray is traced through the atmosphere to the TES sensors. A simplification in this ray tracing can be made, for those rays that do not intersect a boundary such as the earth or a cloud, by specifying that each ray must correspond to a tangent point of one of the TES forward model pressure levels. A tangent point is defined as the location where a ray is coincident and parallel to a level. Radiances for each ray are computed using the approach discussed in Section 3.3.1.6. Each ray spectra is then convolved with the TES instrument-line-shape (ILS) function to account for the TES spectral resolution. Then, the radiances from the bundle of rays are integrated over the angular response of each detector to compute the expected angular radiance for each of the TES detectors (see Section 3.3.6). As discussed in the DFM 1405, titled "Ray Table Update And Implementation Steps", ray levels (or tangent levels) are specified in a ray table. For the study presented in this section, each ray is designated as "CLEAR", that is, the ray tracing and radiative transfer algorithm would assume a clear-sky when modeling the ray. Other categories include:

1) Surface: rays that intersect the terrestrial boundary or a cloud.
2) Scattering: A ray that accounts for scattering
3) Detector: This type indicates that the forward model is to swap a modeled radiance with a measured detector radiance in order to account for a cloudy radiance field (see section 3.3.3)

The ray table specifies which levels are to be used for discretizing the angular radiance field. There are 32 rays total in this ray table. The modeled detector radiances using this set of rays is subsequently compared to the modeled detector radiances using a finer discretization of 64 rays (Figure 3-2 and Figure 3-3).

Figure 3-2: Comparison of Radiances for 2A1. The top panel shows the limb angular radiances across all 16 TES detectors. The bottom panel shows that difference between radiances if 64 rays is used for the forward model calculation versus 32 rays. This figures shows that the difference is much less than the expected 2A1 NESR hence we can conclude that 32 rays is sufficient discretization.

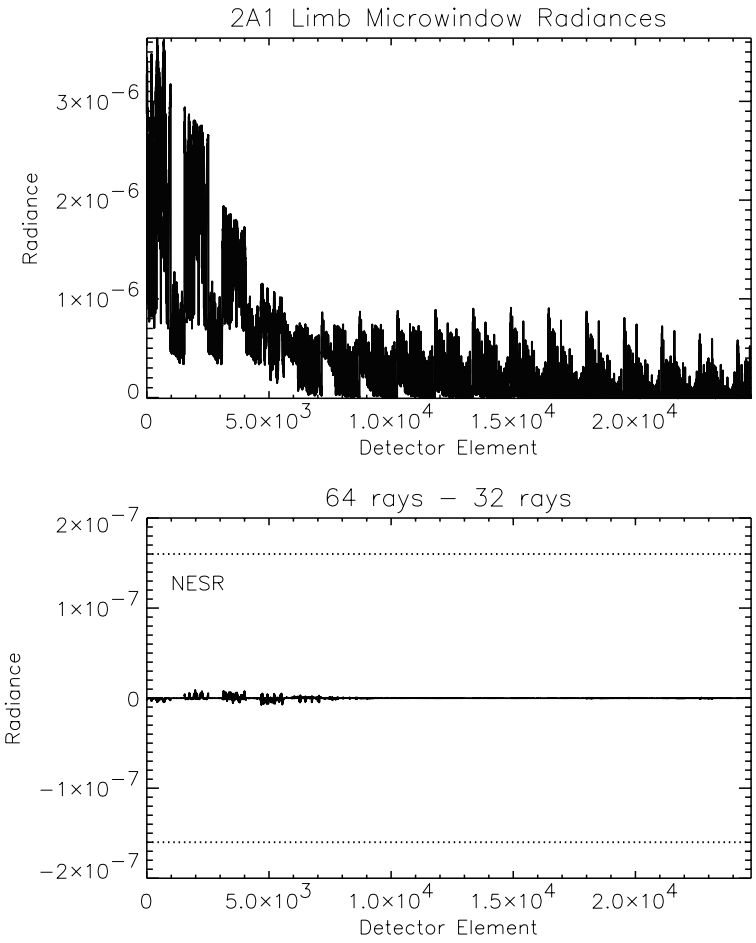

Figure 3-3: This figure is the same as in Figure 3-2 except it is for the 1B2 filter. Again, 32 rays is sufficient for computing forward model radiances.

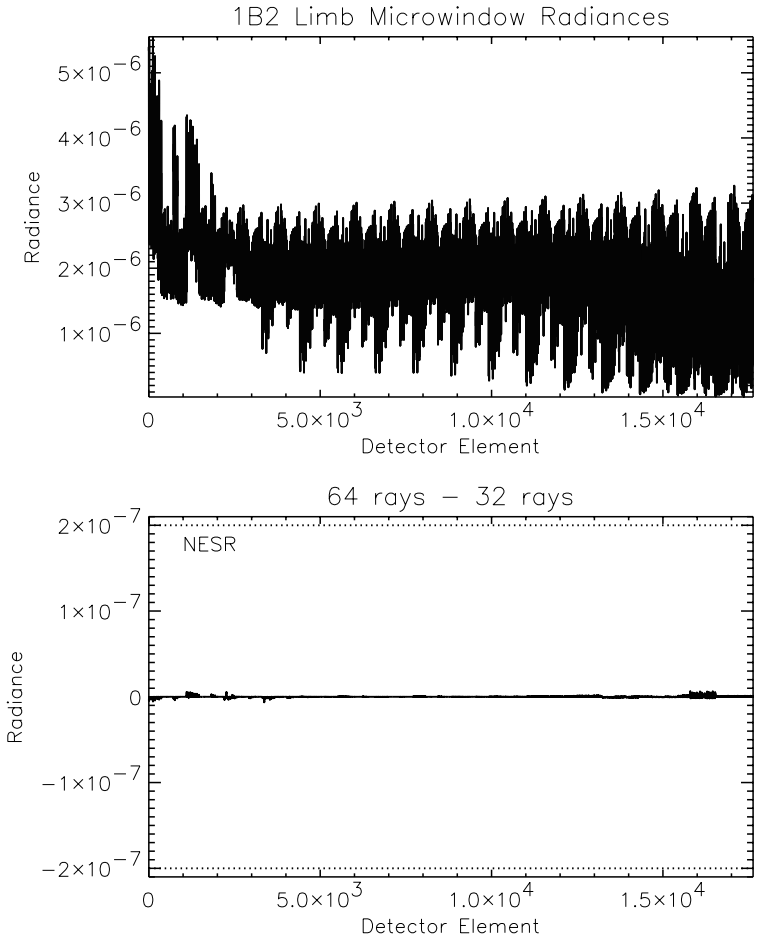

3.3.1.4 Optical Depth

The optical depth (OD) along the line of sight for a given layer *l* is calculated as

$$\tau(\nu)_l = \sum_m u_{m,l}\ k_m\left(\overline{T}, \overline{P}, \nu\right) \tag{3.7}$$

where the sum is over species, $u_{m,l}$ is the layer molecular amount for absorber m, and $k_m(\overline{T}, \overline{P}, \nu)$ is the absorption coefficient for molecule m. $u_{m,l}$, $\overline{T}$, and $\overline{P}$ are calculated in the ray-trace and path integral step. Although we will still keep the option of using a line-by-line model to calculate absorption coefficients, for most molecules $k_m(\overline{T}, \overline{P}, \nu)$ will be pre-calculated at fixed P/T grids and stored in files (ABSCO Tables). Section 3.3.7 describes the ABSCO Table generation and discusses the $k_m(\overline{T}, \overline{P}, \nu)$ interpolations in temperature / pressure / H_2O VMR. The frequency grid spacing of $\tau(\nu)$ for the line species in the HITRAN list is defined in Table 3-1.

The cross-section, continuum, and cloud absorption coefficients (Section 3.5 and 3.6) will be stored and calculated on a coarser frequency grid spacing (Section 3.2.4). This is mostly determined by the representative spectral structures shown in some cross-section species, and this coarser frequency spacing is the TES tier 2 spacing.

The total layer optical depth is then calculated by the sum of the tier 1 OD and the interpolated tier 2 OD. The tier 2 to tier 1 interpolation is performed using a 4-point Lagrange interpolation scheme.

3.3.1.5 Calculation Of Absorption Coefficients And Optical Depths For Multiple Rays

Calculation of optical depths is computationally expensive. However, computation of molecular absorption coefficients and total optical depth can be reduced for computing the angular radiance field with multiple rays because absorption coefficients for any given layer are approximately the same for all rays traced through the layer. If the average pressure and temperature of a layer for some ray traced through the layer is within 0.1% and 0.1 K respectively of that from a reference ray then the absorption coefficients can be reused for the optical depth and Jacobian calculation, that is:

$$\begin{aligned} \left|1-\overline{P}_{\ell}^{ray} / \overline{P}_{\ell}^{ray-ref}\right| &< 0.01 \\ \left|\overline{T}_{\ell}^{ray} - \overline{T}_{\ell}^{ray-ref}\right| &< 0.1K \end{aligned} \tag{3.8}$$

where *ray-ref* indicates a reference ray for which molecular absorption coefficients and optical depths have been computed, $\overline{P}_{\ell}^{ray}$ and $\overline{T}_{\ell}^{ray}$ are the average pressure and temperature respectively for layer ℓ and ray-index *ray*.

Furthermore, the total optical depth of a layer for some ray can be scaled from the total optical depth of a reference ray (with less than 0.1% loss in accuracy for the radiance calculation) if the above condition is met along with the subsequent condition:

$$\begin{aligned} &\left|1-R_{\ell,avg}^{ray} / R_{\ell,species}^{ray}\right| < 0.001 \\ &where \\ &R_{\ell,avg}^{ray} = \sum_{i=1}^{N_{species}} u_{\ell,i}^{ray} / \sum_{i=1}^{N_{species}} u_{\ell,i}^{ray-ref} \\ &R_{\ell,species}^{ray} = u_{\ell,species}^{ray} / u_{\ell,species}^{ray-ref} \end{aligned} \tag{3.9}$$

and $u_{\ell,species}^{ray}$ is the column amount for some *species* at layer ℓ and ray index *ray*. The total optical depth for a given ray and layer ℓ can be computed by multiplying the optical depth from *ray-ref* and layer ℓ by the scaling factor: $R_{\ell,avg}^{ray}$.

3.3.1.6 Atmospheric Radiance

The spectral radiance at the satellite is given in Equation (3.5). By neglecting the reflected sunlight term the monochromatic radiance may be summarized as

$$L_{sat} = L_L^{\uparrow} + \varepsilon B\left(T_{sfc}\right)\mathcal{T}_{0,L} + \alpha L_0^{\downarrow}\mathcal{T}_{0,L} \tag{3.10}$$

in which $L^{\uparrow}_L$ is the upwelling radiance contribution of the atmosphere from the surface to the level at the top of the atmosphere (TOA), $\mathcal{T}_{0,\mathrm{L}}$ is the transmittance of the atmosphere and $L^{\downarrow}_0$ is the downwelling radiance of the surface. For a specularly reflecting surface, $L^{\downarrow}_0$ is calculated for the same zenith angle as $L^{\uparrow}_{\mathrm{L}}$ and α is the appropriate bidirectional reflectance. For a Lambertian surface, $L^{\downarrow}_0$ is calculated at the diffusivity angle, the downwelling radiation scattered by the surface is taken to be isotropic and α is the albedo.

In the limb case, there is no surface term. $L^{\uparrow}_{\mathrm{L}}$ is then the radiance contribution from the portion of the atmosphere from the tangent to the satellite and $L^{\downarrow}_0\mathcal{T}_{0,\mathrm{L}}$ would be the radiance contribution from the atmosphere from the far-side space to the tangent along the line of sight.

The upwelling term, $L^{\uparrow}_{\mathrm{L}}$, the downwelling radiance, $L^{\downarrow}_0$, and the total transmittance $\mathcal{T}_{0,L}$ are calculated recursively in a layer loop. For example, in the case that the calculation starts from Earth's surface to satellite, $L^{\uparrow}_{\mathrm{L}}$, $L^{\downarrow}_0$, and $\mathcal{T}_{0,L}$ are initialized as 0.0, 0.0, and 1.0. At each layer step (l), they are updated, as illustrated in Figure 3-4),

$$L^{\uparrow}_{l+1} = L^{\uparrow}_l\mathcal{T}_l + \left(1-\mathcal{T}_l\right)B_{eff} \tag{3.11}$$

$$L^{\downarrow}_{l+1} = L^{\downarrow}_l + \left(1-\mathcal{T}_l\right)B_l\mathcal{T}_{0,l} \tag{3.12}$$

$$\mathcal{T}_{0,l+1} = \mathcal{T}_{0,l}\mathcal{T}_l \tag{3.13}$$

where $\mathcal{T}_l$ is the layer transmittance which is not necessarily the same for upwelling and downwelling cases ; B_l and B_{eff} are the Planck function at layer mean temperature T_l and the layer effective Planck function defined below.

Figure 3-4: Illustration of the recursive radiative transfer calculations

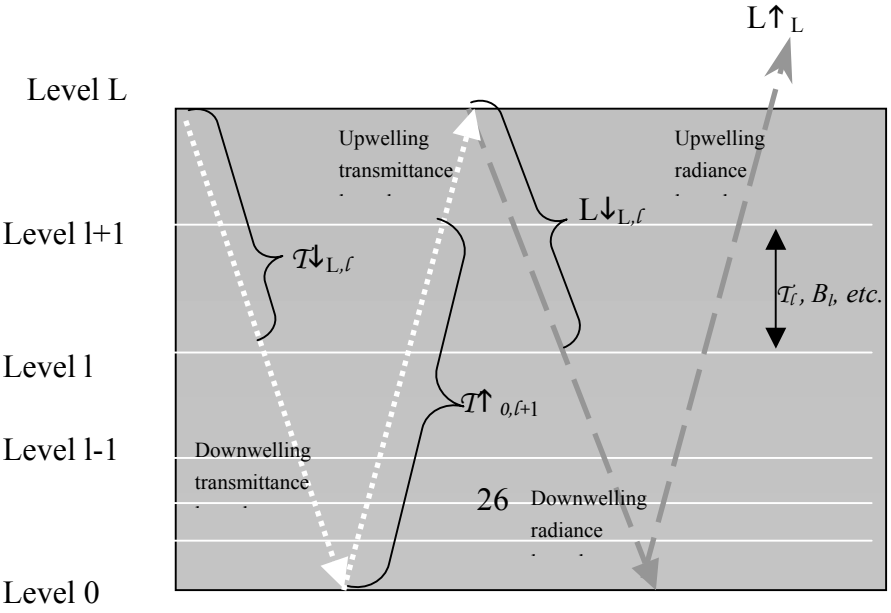

The layer transmittance $\mathcal{T}_l$ is calculated as

$$\mathcal{T}_l = \exp\left(-\tau_l\right) \tag{3.14}$$

where τ_l is the layer optical depth, as described in 3.3.1.3. Since the exponential calculation is relatively expensive, it is pre-computed and tabulated.

In order to simulate the contribution of the layer emission to the total radiance more accurately, we apply the "linear-in-tau" approximation [Clough et al., 1992]. The source term in Equation (3.11) uses an effective Planck function defined as

$$B_{eff}(\overline{T_l}, T_{l+1}, \tau_l) = B(\overline{T_l}) + \left[B(T_{l+1}) - B(\overline{T_l})\right]\left\{1 - 2\left[\frac{1}{\tau_l} - \frac{\mathcal{T}_l}{1-\mathcal{T}_l}\right]\right\} \tag{3.15}$$

where $B(T_{l+1})$ is the Plank function calculated using the layer upper level temperature, T_{l+1},. The function

$$F(\tau_l) = 1 - 2\left[\frac{1}{\tau_l} - \frac{\mathcal{T}_l}{1-\mathcal{T}_l}\right] \tag{3.16}$$

and its derivative with respect to optical depth are pre-calculated and tabulated for computation efficiency (Figure 3-5). For small optical depth, $F(\tau_l) \to \frac{\tau_l}{6}$ for $\tau_l \to 0$, which can be shown either graphically or by expanding $F(\tau)$ to 2nd order terms. This effective Planck function has the desired behavior at the two extremes, e.g., optically thin layers, $B_{eff} \approx B(\overline{T_l})$ and optically thick layers, $B_{eff} \approx B(T_{l+1})$.

The calculation of Plank function as a function of frequency at the forward model frequency grids is very time consuming. We therefore implemented a piecewise continuous approximation in this calculation. The accurate Plank function is calculated at coarser frequency grids (Section 3.2.4) and a linear interpolation is done for the grids in between.

Figure 3-5: Linear in Tau function and its derivative.

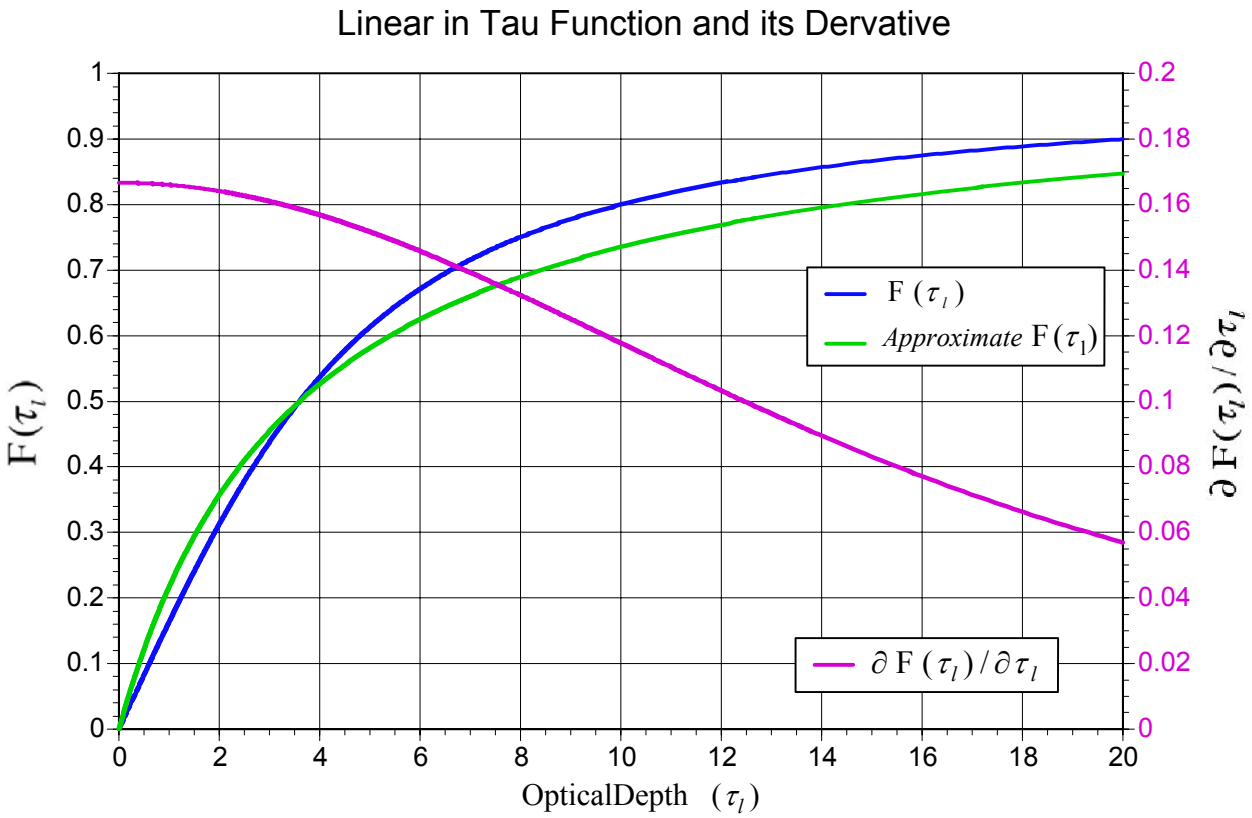

3.3.1.7 Non-LTE

In certain circumstances it is necessary to make allowances for departures of the source function *J* from the Planck function. This will be most important for the case of nitric oxide, which has significant non-thermal emission from the thermosphere, particularly in the presence of solar activity. This emission can be a significant fraction of the total measured NO signal. To account for Non-LTE the forward model must be able to accept the populations of the individual vibrational levels affected relative to the Boltzmann population, which depends only on temperature. The algorithm to be implemented in the forward model for the calculation of NLTE radiances is provided in Appendix A3.3.1.5.

Two approaches are being explored to obtain NLTE state populations for the TES spectral measurements:

(1) Estimate the populations of the excited states, using existing models and climatological temperature and solar irradiance values. This will provide a non-LTE climatology to be included as forward model parameters. For NO, retrieve only the mixing ratio in the troposphere and lower stratosphere.

(2) Retrieve the populations of the affected vibrational levels at all relevant altitudes, as well as the mixing ratio distribution. This would proceed in the same way as retrieval of any other parameter, by including the relative populations in the state vector, and computing the Jacobians for them.

3.3.1.8 Radiative Transfer for the Solar Contribution

The contribution to the radiance at the satellite due to scattered solar radiation must be taken into account in the spectral region 2000-3050 cm^{-1}. Experience with HIS spectra suggests that, under solar conditions, there is almost always some solar scattering due to atmospheric clouds and aerosols (see Section 3.3.3) in addition to the scattering from the surface. Empirical techniques will be developed and utilized to address scattered solar effects in the affected microwindows in addition to the treatment of the scattered radiation from the surface. For the nadir case, the radiative transfer including the surface scattering is given as

$$L_{\text{sat}} = L_L^{\uparrow} + \varepsilon B(T_{\text{sfc}})\mathcal{T}_{0,L} + \alpha L_0^{\downarrow} T_{0,L} + \mathcal{R}_{\text{BRDF}}(90,\theta_{\text{sun}}) J_{\text{sun}} \mathcal{T}_{\text{sun}_{0,L}} \mathcal{T}_{0,L} \qquad (3.17)$$

where J_{sun} is the solar source function at the top of the atmosphere, $\mathcal{T}_{\text{sun}_{0,L}}$ is the transmittance of the atmosphere along the solar refracted path and $\mathcal{R}_{\text{BRDF}}(90,\theta_{\text{sun}})$ is the surface bidirectional reflectance.

The solar contributions will be calculated at the monochromatic wavenumber grid. The appropriate Doppler shift due to Earth's rotation and orbit, and radiance adjustment due to the distance of the Earth to the sun will be taken into account. Treatment of these effects involves minimal computation time.

The method of calculation will be to use an effective secant for the solar path in each layer, thus making use of the optical depth calculation being done for the upwelling atmospheric radiation. The reference radiative transfer model will have the capability to treat solar scattering in the single scattering approximation at each layer given a profile of scatterers and their optical properties. The initial approach for the limb will be to remove spectra that are strongly contaminated by solar scattering in the 2000-3050 cm^{-1} spectral domain, recognizing that if strong aerosol conditions exist, appropriate methods will be applied to extract as much information as possible for species optically active in this region [Rinsland *et al.,* 1994].

3.3.1.9 Surface Contribution

The radiance at the satellite including the effects of scattering and reflection at the surface may be written as,

$$L_{\text{sat}} = L_L^{\uparrow} + \varepsilon B(T_{\text{sfc}})\mathcal{T}_{0,L} + \alpha L_0^{\downarrow} T_{0,L} + \mathcal{R}_{\text{BRDF}}(90,\theta_{\text{sun}}) J_{\text{sun}} \mathcal{T}_{\text{sun}_{0,L}} \mathcal{T}_{0,L} \qquad (3.18)$$

where J_{sun} is the solar source function at the top of the atmosphere, $\mathcal{T}_{\text{sun}_{0,L}}$ is the transmittance of the atmosphere along the solar refracted path and $\mathcal{R}_{\text{BRDF}}$ $(90, \theta_{sun})$ is the surface bidirectional reflectance. The terms associated with the upwelling radiance of the atmosphere, the surface emitted radiance and the surface reflected solar radiance can be treated rigorously assuming that the surface emittance is isotropic with emissivity ε and that $\mathcal{R}_{\text{BRDF}}$ $(90, \theta_{\text{sun}})$ properly describes the solar scattering by the surface. The radiance due to the surface scattering of the downwelling irradiance is a rather more complex problem. First, this term is assured not to be large: if the

atmosphere is in the optically thin regime then the downwelling flux is small, and is further reduced by the surface albedo so that the radiance at the satellite is dominated by the surface emitted radiance attenuated by the satellite. In the optically thick regime, there is no contribution from other than upwelling radiance of the atmosphere. As a consequence of this perspective, the accuracy of the forward model radiance at the satellite is not highly dependent on the accuracy of the value for the albedo or on the accuracy of the calculation of the downwelling irradiance.

The scattering due to the surface is characterized as either Lambertian or specular. For the Lambertian case, the downwelling irradiance, $L_{\vartheta}^{\downarrow}$ is required. This is obtained by performing the radiance calculation along the diffusivity ray (secant = 1.66) [Chandrasekhar, 1960, Goody and Yung, 1989]. The product of this radiance and the albedo provides an excellent approximation to the scattered upwelling isotropic radiance at the surface. The motivation for this approach is the low computational cost with acceptable accuracy. The layer optical depth for the diffusivity angle is obtained by multiplying the nadir layer optical depth by the secant angle. Although an additional exponential is required, this approach is faster than alternative methods. In general, the albedo will be taken as 1-ε with ε a retrieved parameter but could also be retrieved directly.

In the case of specular reflection, α assumes the role of a bidirectional reflectance, e.g. $\mathcal{R}_{\mathrm{BRDF}}$ (90, 90) for the nadir case. The downwelling radiance is calculated for the same secant as the upwelling (secant = 1 in the nadir case) and the same layer transmittances are used for both the upwelling and downwelling radiances. This calculation is fast and has full accuracy.

3.3.1.10 Horizontal Inhomogeneity

At the limb, the path length through the tangent layer can be many tens of kilometers. Consequently, the assumption that the atmosphere is homogeneous in composition and physical state may not be valid. It further follows that the ensuing discussion is tentative and subject to "lessons learned" once we are on orbit.

The approaches that we shall investigate (in order) are

1) Ignore Line-of-Sight (LOS) gradients in the forward model, retrieve a single profile from a single set of spectra, and include the effect in the error analysis (*i.e.* if a gradient exists, the residuals will increase).

2) Assume some known LOS gradients in the forward model. For temperature/pressure this can come from meteorological data. For constituents it can come from a first pass using method (1). This approach has been used by LRIR, LIMS, and ISAMS.

3) First perform a "nadir-type" retrieval (but with cold space rather than the Earth's surface as background) *along the LOS*. The weighting and contribution functions will be strongly peaked in the tangent layer, but this is where inhomogeneity will have most of its impact. Use the results (one for each pixel) as a first guess for the standard limb retrieval.

4) Retrieve the 2-D distribution (or at least a mean profile and a profile of the LOS gradient) from a single set of spectra. If horizontal inhomogeneity has a measurable effect on the radiances, then there is, in principle, information about it from which it might be retrieved. However this information might also alias into something else. Only numerical experiments can tell the difference.

5) Simplified tomography by sequential estimation. For example, consider successive profiles at the locations corresponding to three successive measurements. Call them A, B, and C in time order. Set up an *a priori* (see later). Use the B spectra to retrieve all three profiles jointly. The result gives the final retrieval for the A profile. The retrievals so far for B and C become *a priori* for the next cycle, and *a priori* for D, the next location, are obtained by a combination of, for example, climatology and extrapolation. Now use the C spectra to retrieve B, C, and D jointly. This gives the final retrieval for B and the C and D *a priori* for the next cycle. Repeat.

3.3.2 Surface Model

3.3.2.1 Surface Radiative Properties

TES nadir data will have many spectral regions that contain information about the surface radiative properties, ("window" regions). As discussed in 3.3.1, unless we have additional information about the bi-directional reflectance, the surface model must choose either a Lambertian or specular reflectance approximation for the forward model calculation. For either case, we will assume that the albedo is $1-\varepsilon$, where ε is the emissivity. For any forward model frequency, ν, the emissivity is calculated from a linear interpolation. We can then model the surface contribution with a single "skin" temperature and the emissivity spectrum, which gives us the flexibility to adjust the emissivity structure for specific target types.

The *a priori* emissivity values will be generated using the seasonal land characteristics for the target spot and weighted emissivity spectra for the specific materials (e.g., deciduous trees or dry grass) that are likely to be present. Note that the preponderance of our nadir targets are either water or ice, which have reasonably well known emissivities [Wu and Smith, 1997, Smith *et al.,* 1996 and Masuda *et al.,* 1988] (See Figure 3-6).

In order to arrive at a reasonable first guess of emissivity, or where appropriate, the bi-directional reflectance for a target surface scene, we will need an up-to-date estimate of the seasonal land cover for the latitude and longitude of each pixel in a given nadir view. Since the footprint of an individual pixel is approximately 0.5 by 5 km, a database with spatial resolution of order 1 km (or 32 arc-seconds) should suffice. An existing database of land cover characteristics with 1 km resolution is described in Appendix 3.5.2.1

For the TES Level 2 algorithm to access this type of data efficiently, the global maps will likely need to be reformatted from separate seasonal images to a look-up table of land cover type vs. season or month, latitude and longitude. The land cover type from the table would then specify the emissivity function to be used in the first guess of the surface model parameters. If a particular land cover type required further differentiation, such as snow/ice or dry/wet grasslands, additional information, if available, could be employed. If no additional information

were available, default values for the emissivity of the ambiguous land cover type would be used.

Figure 3-6: Sea water emissivity [Wu and Smith, 1997].

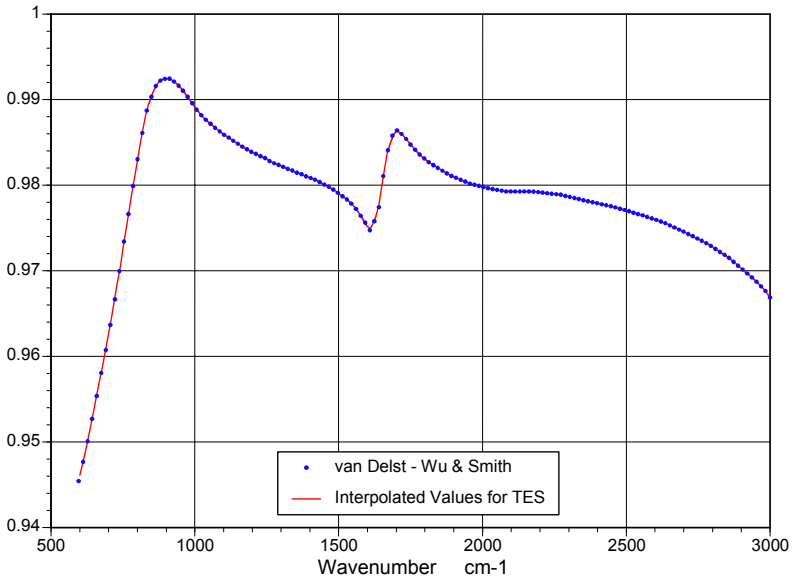

3.3.2.2 Digital Elevation Model

The digital elevation map (DEM), together with NCEP sea level pressures and the hydrostatic equation, are used to estimate the surface pressure at the location of an observation for nadir retrievals. The DEM simply provides the difference in altitude between the location of an observation and sea-level pressure reference geoid. Integration of the hydrostatic equation, using this elevation difference and the *a priori* temperature profile, gives an estimate of the surface pressure.

There are a number of global DEMs available. The only issue is horizontal resolution and vertical accuracy. The highest spatial resolution DEMs with global coverage are limited to latitude-longitude bins of 5 arc-minutes. At the equator this corresponds to an area of 9.28 x 9.28 km^2, somewhat larger than the 8.5 km along track by 5.5 km cross-track nadir footprint of (i.e. the coverage of a 16-pixel TES detector array). The altitude at the pixel is estimated from a 2 dimensional linear fit and interpolation of the DEM elevations along the spacecraft track.

The requirements for DEM altitude accuracy is driven by the requirement that errors in total column density be less than 0.5%. This translates into a maximum allowable elevation error of about 42 m near sea level.

The principle candidate data set is the GTOPO30:

http://www.ngdc.noaa.gov/seg/globsys/globe.html

under development at NOAA's National Geophysical Data Center. It improves upon the ETOPO5 map with increased horizontal resolution (30-arc-second or 1 km grid). Currently, this map covers about 60% of the Earth's land surface. It is anticipated that this data set will cover the Earth's complete land surface before launch of the CHEM platform.

The EOS Product Generation Software Tool-Kit provides routines to extract the elevation data from both of this DEM.

3.3.3 Radiative Transfer for Clouds and Aerosols

The capability to treat cloud aerosol radiative effects is an important aspect of the radiative transfer to be included in the forward model. Clouds and aerosols differ from gases not only because their light extinction behavior varies slowly with frequency, but also because they are scattering and absorbing, not simply absorbing like gases. The principal contributions to the radiative transfer associated with aerosols are somewhat different for the nadir and limb viewing modes. The general radiative transfer equation including scattering and ignoring solar radiation terms and downwelling reflected atmospheric emission is as follows.

$$L(\Omega,\nu)=\int_0^{\infty}\Phi(\nu,\nu')\left\{(1-\omega_\nu)\int_{z_0}^{\infty}B(\nu',T(z))\frac{\partial\mathcal{T}(\Omega,z,z_0,\nu')}{\partial z}dz\right.$$

$$\left.+\varepsilon(\Omega,\nu')\cdot B(\nu',T_{surf})\cdot\mathcal{T}(\Omega,z_0,\infty,\nu')\right\}d\nu'$$

$$+\frac{\omega_\nu}{2}\int_{z_0}^{\infty}\int_{-1}^{1}\mathrm{P}(\mu,\mu')L(\Omega,\nu,z)\frac{\partial\mathcal{T}(\Omega,z,z_0,\nu')}{\partial z}d\mu dz \qquad (3.19)$$

This equation differs from Equation (3.5) in the following ways:

- The transmittance now includes transmittance due to aerosols and clouds.
- The atmospheric emission term is now multiplied by $(1-\omega_\nu)$, where ω is the single scattering albedo, defined as $\omega_\nu = \sigma(\nu) / (\sigma(\nu) + \kappa_\nu)$ where $\sigma(\nu)$ is the scattering cross section and κ_ν is the absorption cross section. It should be noted that the single scattering albedo will be a function of frequency, as it is a measure of the scattering coefficient compared to the total extinction. When the gas optical depth is large, the single scattering albedo will be small.
- There is an additional term (the third term) that is the source function for scattering – this represents radiation that is scattered into the line of sight. Under single scattering conditions (small single scatter albedo), this term is insignificant. The importance of this term will also be dependent on the viewing geometry due to the angular dependence of the phase function.

3.3.3.1 Radiative Transfer for Aerosol in Nadir View

The general radiative transfer equation presented above will not be solved generally for operational analysis. Instead, a subset of tractable cases will be considered.

If no clouds or aerosols are present, the single scattering albedo is zero, and this equation becomes (3.5), the radiative transfer equation presented in Section 3.3.1.

When the optical thickness of the cloud or aerosols is small, the single scattering albedo is small and single scattering dominates. The scattering source function can be ignored and the extinction effects of the cloud can be approximated by absorption. This is accomplished by assuming that the single scattering albedo is zero and using 'pseudo extinction coefficients' – absorption coefficients for the cloud or aerosol that result in the same radiative transfer effects as scattering and absorption. For an example of this approach, see Echle *et al*. (1998)

When microwindows are used for the radiative transfer, an assumption of linearity can be made for the cloud or aerosol pseudo-extinction spectra dependence. To implement such a strategy, two cross section species will be created, one with a positive slope, the other with a negative slope. Profile of these two species will be retrieved. The ratio of the two species can vary and allow for any slope. The overall magnitude of the two retrieved profiles is an indication of the overall optical depth of the cloud or aerosol layer. There is a risk that the sensitivity of these cross section species to the cloud height is not large, and the cloud retrieval will interfere with the retrieval of other species that have linear spectral dependence across microwindows, such as the water vapor continuum. This will be investigated.

There may be cases where the optical thickness of the cloud is quite large. In this extreme, T of the cloud is so small (the optical depth is so large) that the surface term and the atmospheric emission terms below the cloud layer do not contribute to the TOA radiance. Given the fact that clouds have a fairly well defined upper surface, it is natural to redefined the surface as the upper boundary of the cloud. In cases where the cloud optical depth is large (greater than 7, or 8) the transmittance through the cloud is quite small (9×10^{-4} or 3×10^{-4}) and rather uniform across the spectra. With the surface redefined as the cloud top height, the first and second terms of the above RT equation remain, and it becomes the original RT equation discussed in Section 3.3.1.

Intermediate cases where the scatter source function term is important will not be considered in routine processing.

3.3.3.2 Radiative Transfer in the Limb with Scatterers

In the case of limb viewing geometry, the surface emission term is not present.

In the case of optically thick aerosols and clouds, where backside radiation is removed with more than 99.99% efficiency, one may consider the cloud or aerosol as the surface. Unfortunately, there is great uncertainty as to the actual location of the cloud – with the placement along the line of sight poorly known, it would be quite difficult to define the radiative transfer problem in a tractable way. Therefore, in the case of optically thick aerosols or clouds, the surface will be

redefined to the lowest pixel not effected by the aerosol or cloud (see 3.5.5 pixel categorization section for more details).

In some cases, it may be possible to include a parameterized form of the term for the scattered source.

For limb measurements, it will be important to account for the effects of stratospheric sulfuric acid aerosols. Under background conditions (sufficient long time after a volcanic eruption), this will be a low optical depth layer at altitudes roughly from 17 to 24 km. No surface term is needed and the scattering source term can be ignored. As was done in the nadir, 'pseudo extinction' coefficients can be used to treat the aerosol effects as absorption with linear dependence across the microwindows. (Echle *et al*. (1998)). This will be achieved with the two linear cross section species described in Section 3.3.3.1.

3.3.4 Solar Source Function

Extraterrestrial solar radiance will contribute to the TES observed radiance in the 2000-3050 cm^{-1} spectral regime. In order to accurately model the impact of the solar source radiance in the spectrum, the solar source function of Kurucz [1995, 1992, 1984], shown in Figure 3-7, is used in the forward model. It is the result of a radiative transfer calculation based upon solar measurements, including those of ATMOS [Gunson *et al.,* 1996], with a resolution of 0.0040 cm^{-1} at 2000 cm^{-1} and 0.0061 at 3050 cm^{-1}. The spectra are interpolated and stored on the operational monchromatic frequency grid.

Given the solar function J_{SUN}, total transmittance through the atmospheric path $\mathcal{T}_{0,L}$, and surface albedo α, the solar contribution to the radiance observed at the satellite L_{SUN} is given as

$$L_{sun} = J_{sun}\mathcal{T}_{0,L}\alpha \qquad (3.20)$$

where α=1 in limb viewing mode. This source function results from a spatial integration over the solar disk and is provided at monochromatic resolution. For radiative transfer calculations using the solar source function, the proper Doppler shifts between the scattering medium (nadir view) and the sun must be applied to the spectrum. Initially we would assume a static solar source function, but we may need to investigate the effects of the solar cycle.

Figure 3-7: Monochromatic solar spectrum over the spectral region relevant to TES (Kurucz, 1995).

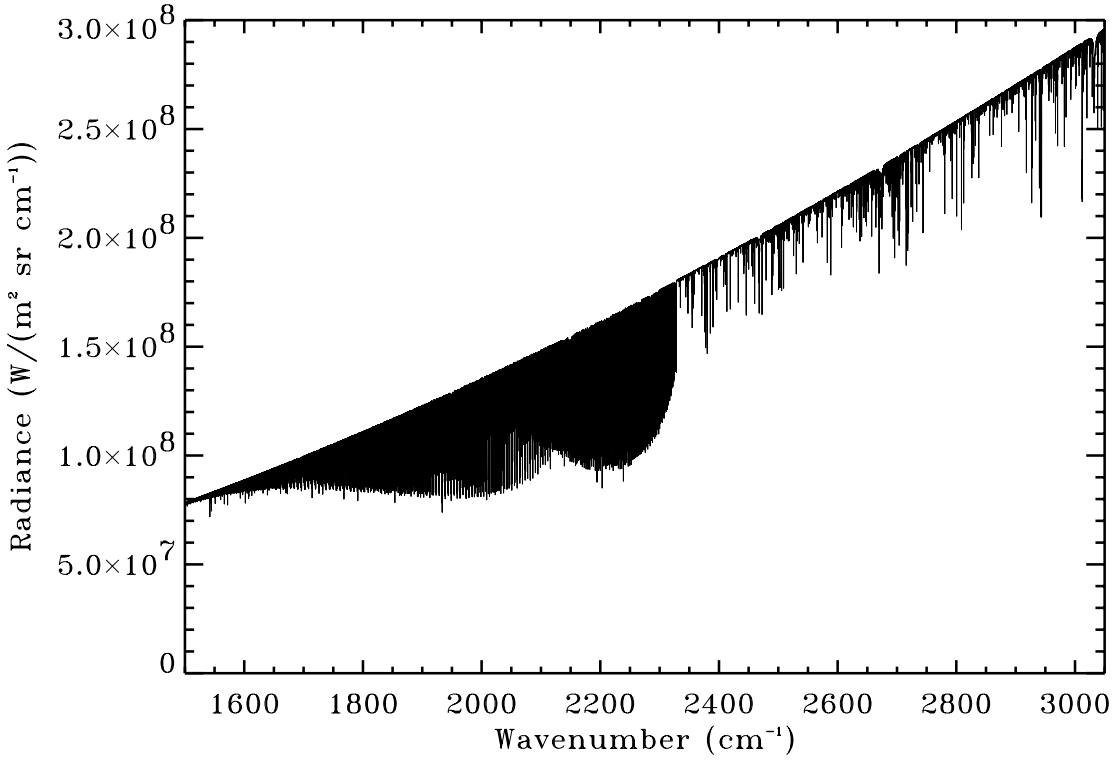

3.3.5 Instrumental Line Shape Spectral Convolution and Apodization

In order to compare with the measured spectra, the calculated monochromatic spectra at very fine spectral grids described in previous sections need to be convolved, or smoothed, with the instrument line shape (ILS) function. This convolution is described as

$$L_C(\nu) = \int_{-\infty}^{\infty} L_M(\nu')\, \Phi(\nu - \nu')\, d\nu', \tag{3.21}$$

where L_M and L_C are the monochromatic and convolved spectral radiances respectively, and Φ is the ILS function which ideally is a *sinc* function.

An efficient way of performing the above convolution is to multiply the Fourier transforms of the L_M and Φ and then transform the result back to the frequency domain. This method directly simulates the operation of a FTS. The monochromatic radiance is transformed into an interferogram, then it is apodized, and transformed back to obtain the convolved spectra.

The spectral range for L_M (the integration boundaries in Equation (3.21)) calculated in the forward model needs to be extended beyond the range of L_C in use. Study shows that this

extension should be over 160 *sinc* halfwidths so that the error in L_C due to this truncation becomes insignificant (Gallery and Clough, 1992). In cases where microwindows are used for retrievals, this extension of the monochromatic spectra could make the forward model calculations more computationally expensive. For example, a ±6 cm^{-1} extension is needed for TES nadir simulations. Norton-Beer apodization would reduce this frequency extension. For the general case, 160 halfwidths corresponds to a *sinc* function amplitude decrease of 0.0035. Therefore, we have estimated the extension needed for the Norton-Beer apodization functions based on the fractional amount in frequency space where these decrease to 0.0035 of their maximum values compared to the *sinc* function defined on the same frequency index scale. Table 3-2 lists the spectral resolutions and the minimum extensions for L_M to derive L_C based on four different apodizations.

Table 3-2: Resolution and suggested forward model extension values.

Apodization Case	Resolution Factor	Nadir Resolution (cm^{-1})	Nadir Extension (cm^{-1})	Limb Resolution (cm^{-1})	Limb Extension (cm^{-1})
None (box function)	1.0	0.07143	6.0	0.01786	1.5
Norton-Beer Week	1.2	0.08571	3.36	0.02143	0.84
Norton-Beer Medium	1.4	0.10000	1.44	0.02500	0.36
Norton-Beer Strong	1.6	0.11429	0.48	0.02857	0.12

Although we expect the line shape to be asymmetric due to the off-axis geometry of the TES detectors (Bowman, *et al*., 2000), this effect was not observable above the noise level in averaged, high-resolution gas cell spectra taken during instrument calibration (Beer, et al., 2003). Therefore, we do not need to model this effect in L2 as previously assumed. A sinc function corresponding to the maximum optical path difference (max OPD) will suffice for the instrument line shape. Interferogram self-apodization due to off-axis detectors will be corrected in L1B for high resolution spectra, as described in the TES L1 ATBD. Off-axis asymmetry, as well as other frequency grid interpolation errors, are mitigated by applying Norton-Beer apodization to the L1B spectra. As discussed above, apodization is applied to the L2 forward model in order to minimize the frequency range needed for the monochromatic calculation, and must therefore be applied to the L1B spectra as well.

3.3.6 Field-of-View Spatial Integration

The TES forward model derives the effective radiative response of a pixel at the satellite by performing a trapezoidal integration of the Field Of View (FOV) function with the representation of the radiance field provided by multiple rays originating at specified tangent points. The set of refracted path radiances, $L(\theta_k)$, is obtained by running the forward model over TES prescribed tangent pressure levels, k=0, … N_{ray}, with corresponding zenith angles at the TES boresight, θ_k. (See Figure 3-8). The TES instrument spatial FOV function for detector d, $R_{FOV,d}$ is stored on an angular grid θ_j, j = 0, … N_{FOV} appropriate for the trapezoidal integration.

The forward model radiances, $L(\theta_k)$, are interpolated to match the $\mathsf{R}_{FOV,d}$ grid using a four point Lagrange method for unequally spaced points with continuous first derivatives and are then integrated with $\mathsf{R}_{FOV,d}$ to obtain the effective radiance at the detector. (For the top and bottom rays, three point Lagrange interpolation is used.) The calculated radiance for detector d at the satellite L_{sat} is given as

$$L_{sat}\left(\theta_d\right) = \sum_{j=0}^{N_{FOV}} L\left(\theta_j\right)\mathsf{R}_{FOV,d}\left(\theta_j - \theta_d\right)\Delta\theta_j \tag{3.22}$$

where $\theta_d = \theta_p + \Delta\theta_d$; θ_p is the instrument pointing angle, which corresponds to the TES boresight, (defined as the 2B detector array center point), $\Delta\theta_d$ is the fixed angular difference between this point and the center of detector d, and $\Delta\theta_j = \frac{1}{2}\left(\theta_{j+1} - \theta_{j-1}\right)$. The interpolated radiances corresponding to the angular grid of the FOV function are

$$L(\theta_j) \;=\; a_{j,\text{-}1}\, L(\theta_{k\text{-}1}) + a_{j,0}\, L(\theta_k) + a_{j,1}\, L(\theta_{k+1}) \;+\; a_{j,2}\, L(\theta_{k+2}) \tag{3.23}$$

with Lagrange coefficients $a_{j,-1}$, $a_{j,0}$, $a_{j,1}$, and $a_{j,2}$ defined as follows:

$$a_{j,\text{-}1} = p(\text{-}1+2p-p^2)/(1+c_1) \tag{3.24}$$
$$a_{j,0} = 1 + p^2[2p\text{-}3+(1\text{-}p)/(1+c_2)]$$
$$a_{j,1} = p^2(3\text{-}2p) + p(1\text{-}2p+p^2)/(1+c_1)$$
$$a_{j,2} = p^2(p\text{-}1)/(1+c_2)$$

with

$$p = (\theta_j - \theta_k)/(\theta_{k+1} - \theta_k)$$

$$c_1 = (\theta_k - \theta_{k\text{-}1})/(\theta_{k+1} - \theta_k)$$
$$c_2 = (\theta_{k+2} - \theta_{k+1})/(\theta_{k+1} - \theta_k)$$

To implement this integration efficiently, we switch the order of interpolation and summation over FOV angles to obtain frequency-independent coefficients that are then applied to the ray radiances. Since each $L(\theta_j)$ interpolation uses 4 rays, we can form the following coefficients:

$$a_{d,k,m} = \sum_j a_{j,m}\left(\theta_j\right)\mathsf{R}_{FOV,d}\left(\theta_j - \theta_d\right)\Delta\theta_j \tag{3.25}$$

where $k \to k+1$ when $\theta_j > \theta_{k+1}$, *i.e.*, each $a_{d,k,m}$ is the sum over the FOV angles that use the same group of 4 rays. We then reduce this set of coefficients to ray coefficients by combining terms common to each ray, *e.g.*:

$$\text{for } k \geq 3, \qquad b_{d,k} = \sum_{m=-1}^{2} a_{d,k+m-1,m} \tag{3.26}$$

This allows a significant portion of the FOV calculation to be performed after ray-tracing, when the ray angles are available, but before the radiative transfer, *i.e.*, without frequency dependence. The radiance at each detector is then given by the sum over rays:

$$L_{sat}\left(\theta_d\right) = \sum_{k}^{N_{ray}} b_{d,k} L\left(\theta_k\right) \tag{3.27}$$

The analytic partial derivatives of L_{sat} with respect to θ_p for each detector can be calculated at little computational cost from the above expressions. These jacobians are used for the retrieval of the pointing angle.

Figure 3-8: Diagram for TES pointing geometry and FOV convolution in limb mode

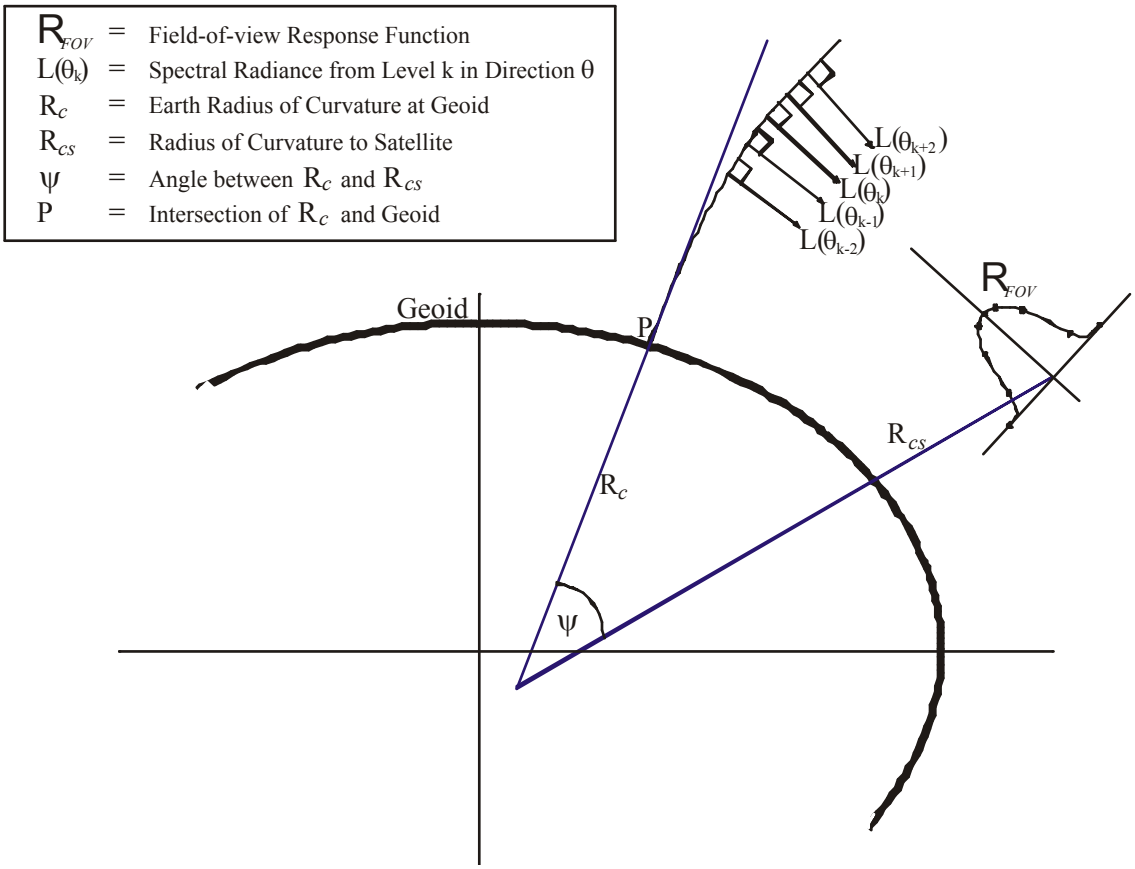

3.3.7 Absorption Coefficient (ABSCO) Tables

3.3.7.1 ABSCO Table Generation (Using LBLRTM)

The absorption coefficients for a given molecular species as functions of pressure, temperature, and frequency will be pre-calculated and stored using TES LBL (a line-by-line code described in next section) without any line rejection approximation. The corresponding pressures will be the TES forward model layer effective pressures pre-calculated using US standard global average temperature profile. At each pressure, about ten temperatures are calculated at every 10 K. A ±60 K temperature band centered at the US standard atmospheric temperature profile [1976 US Standard] is used to limit the temperature grids at a given layer.

Temperature interpolation for total layer optical depth, which is the sum of the layer optical depths for all the molecules considered, will be performed to interpolate OD at pre-defined temperature grids to the TES retrieved atmospheric layer effective temperature. The interpolation scheme will be a three-point Lagrangian method. The pressure interpolation for the layer optical depth will not be required except for the surface layer in the nadir case and for the tangent layer in the limb case. Detailed discussions and validations of this pressure interpolation issue are in Section 3.3.7.4.

In the case of tropospheric water vapor, the self-broadening effect cannot be neglected. The H_2O volume mixing ratio (q) is therefore another variable in the ABSCO tables for tropospheric H_2O. Since the dependence of the H_2O absorption coefficient on its q is nearly linear for a given temperature and pressure, we use linear interpolation/extrapolation in q to calculate the H_2O absorption coefficient for the associated three temperature values. The temperature interpolation is performed as described above. The two tabulated q grids are for extremely dry air, $q_{dry} = 10^{-8}$, and for 90% of the saturation q at the given temperature and pressure grid, $q_{wet} = 0.9*q_{sat}$.

In general, by comparison to real time line-by-line calculations of ABSCO, the advantage of table lookup is to greatly speed up the calculation of the required spectral optical depths. However, there are spectral regions in which lines are sparse for a given molecular species. In these cases, the computational cost of the line-by-line calculation may be comparable or faster. TES team has started to study the data storage issue. In the light of using spectral microwindows for TES retrievals and the advancing of the computing technology, the required storage for TES ABSCO table files should be met without much difficulty.

The effect of interpolations (temperature, pressure, and tropospheric q) on TES retrievals is being examined thoroughly. Preliminary studies for a nadir case show that comparing to the spectral radiance calculated by line-by-line code, the radiance differences are less than 0.5%. A significant advantage of the ABSCO approach is that the accuracy of the absorption coefficient calculation is not limited in any way by computational cost considerations. In addition, the spectral absorption coefficients are readily amenable to empirical adjustment as atmospheric measurements may suggest for improved retrievals.

3.3.7.2 TES Line-by-Line Optical Depth Code

The line-by-line model to be used to calculate spectral absorption coefficients is TES (TES_LBL), an advanced version of the module performing the comparable operation in LBLRTM (e.g. Clough *et al.,* 1995) which itself is based on the FASCODE line by line model [Clough *et al.,* 1981]. These models have a long history of validation in the spectral radiative transfer community. TES_LBL will be used to calculate the spectral absorption coefficients with high algorithmic accuracy. The model is reasonably efficient and is written such that the connection between the physics and the coding is apparent. TES_LBL will be (1) run off line for the generation of absorption coefficients for a lookup table to be used subsequently in the radiative transfer calculation; or (2) incorporated directly into the forward model to be used as part of the online radiative transfer calculation. In the latter case options may invoked to accelerate the calculation with some negligible, acceptable loss of accuracy, e.g. line rejection.

TES_LBL includes the following important attributes: (1) the Voigt line shape is used at all atmospheric levels with an algorithm based on a linear interpolation between precalculated Armstrong [Armstrong, 1967] Voigt functions; (2) all relevant parameters from line databases including HITRAN are utilized including the pressure shift coefficient, the halfwidth temperature dependence and the coefficient for the self-broadening of water vapor; (3) an improved version of the TIPS (Total Internal Partition Sum) program is used for the temperature dependence of the line intensities [Gamache *et al.,* 1990]; (4) the effects of line coupling are treated to second order with the coefficients for carbon dioxide in the 600 - 800 cm^{-1} region included explicitly [Hoke *et al.,* 1988]; (5) the effects of line coupling are treated to first order with coefficients for CO_2 following from Strow et.al, 1994 for the Q-branch regions of 1932, 2076, 2093 and 2193cm^{-1} ; (6) capability to compute quantities for atmospheric layers that are not in local thermodynamic equilibrium(LTE); (7) an explicit formulation is included to address the non-Lorentzian behavior of the wings of carbon dioxide lines. For molecules having an associated continuum, the spectral absorption coefficient calculation utilizes a line shape such that the result of combining the line and continuum contributions provides the correct result.

There have been extensive validations of the LBLRTM model against both upward and downward radiance observations taken by a number of different instruments for a range of atmospheric conditions [Tjemkes *et al*., 2002, Tobin *et al.,* 1999; Mlawer *et al.,* 1997; Clough and Iacono, 1995; Clough *et al.,* 1992]. The assessment of this model has principally been accomplished under the DoE ARM program. In general, the spectral residuals from these validations have been acceptably low for the purposes of TES. There are spectral regimes where continuing evaluation and improvement is required, including the 650-800 cm^{-1} carbon dioxide region, the methane region at 1300 cm^{-1}, and the carbon dioxide bandhead at 2385 cm^{-1}. The magnitude of the residuals is such that errors including the specification of atmospheric state, line parameters and instrument function are of similar order as those of the model errors presenting a significant challenge to model improvement.

Figure 3-9: Observed HIS spectrum and LBLRTM calculated results in equivalent brightness temperature for CAMEX case (a) and observed-calculated differences (b). The nadir measurement was taken from 20 km on the NASA ER2.

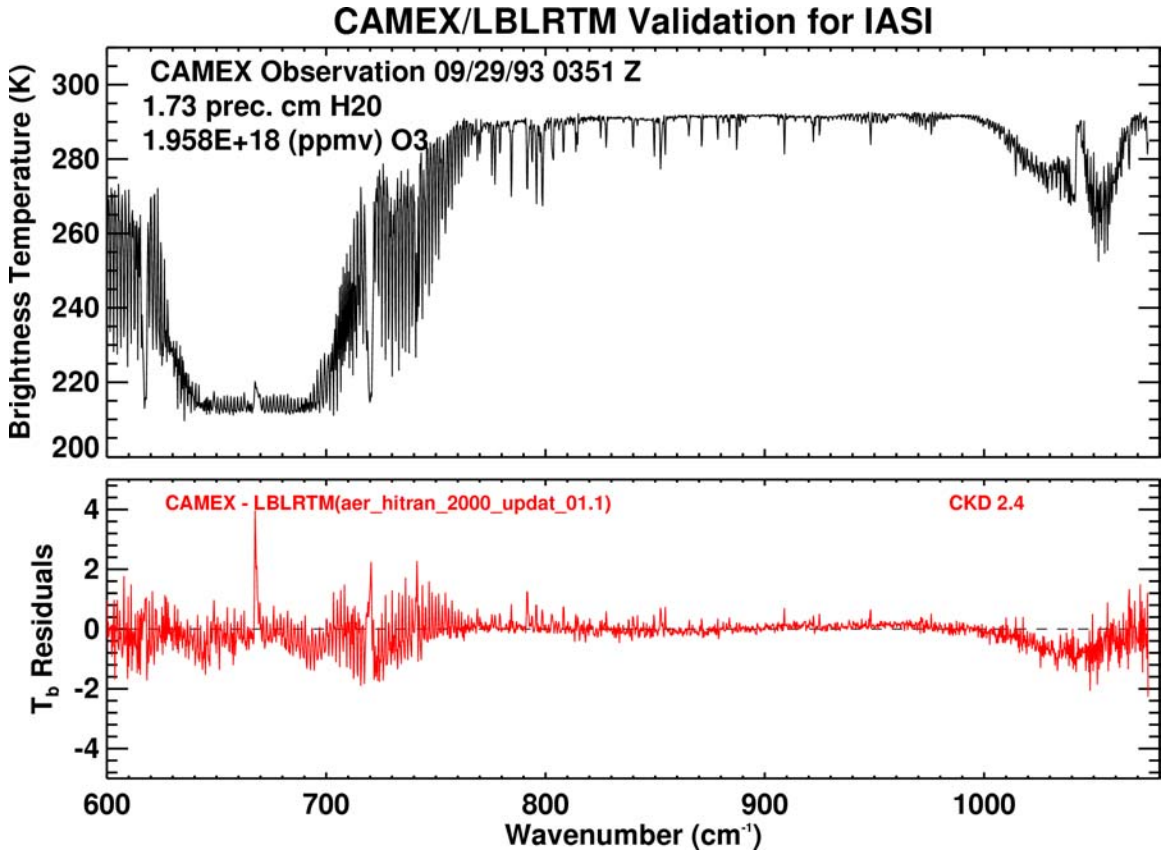

As an indication of the current level of model performance for a portion of the longwave spectral region, we provide in Figure 3-9a radiance spectrum in equivalent brightness temperature obtained with the U. of Wisconsin High-resolution Interferometer Sounder (HIS). The data were taken from the NASA ER2 aircraft during the 1993 Convection and Moisture Experiment (CAMEX) aircraft at an altitude of 20 km in a nadir view over the ocean. The resolution of the unapodized spectrum is 0.22 cm^{-1} (hwhm). The absolute radiometric calibration is better than 1K with the relative calibration better than 0.5K. In Figure 3-9b we indicate the difference between the brightness temperature spectrum of Figure 3-9a and a calculated spectrum utilizing LBLRTM with a version of HITRAN2000 line parameter database with updates (aer_hitran_2000_updat_01.1), [for HITRAN96 refer to Rothman *et al.,* 1998]. Despite the limitation that the atmosphere utilized for the validation was obtained from radiosonde data that was neither co-spatial nor co-temporal, the comparison is extremely good. The surface temperature and emissivity have been adjusted to minimize the brightness temperature differences in the atmospheric window region. The ozone residuals in the 1000-1100 cm^{-1} region have been improved by utilizing a retrieved ozone profile obtained from the spectral data. The effects of heavy molecules including CCl_4, CFC11 and CFC12 have been into account. Carbon dioxide line coupling effects in this region have been accounted for using the temperature dependent first and second order coupling coefficients of Hoke *et al.* [1988]. The

sharp spectral residual at 668 cm^{-1} is actually due to warmer carbon dioxide in the instrument area rather than to line coupling effects. The regularly spaced spectral residuals in the 600- 650 cm^{-1} and 700-760 cm^{-1} regions are an active area of research as this is the region used for temperature retrieval by TES. The residuals are associated with carbon dioxide and are either due to remaining issues with carbon dioxide line parameters or with problems with the characterization of the instrument function. Since this residual signature is also seen in validations with other sensors (i.e. Scanning-HIS AFWEX spectra) it is currently thought that there are remaining issues more with the carbon dioxide spectroscopy. A contribution to the spectral residuals undoubtedly results from errors in the atmospheric temperature and humidity profiles. Of particular note is the high quality of the spectral radiance data in terms of the photometric calibration, the noise and the spectral calibration.

3.3.7.3 Cross-Section Code

Similar to the table look up / temperature interpolation strategy used for the absorption coefficients of line molecules, the cross-section data table for heavy molecules will also be pre-generated at pre-defined pressure and temperature grids. These layer pressure and temperature grids will be the same as the grids used for the line species (Section 3.3.7.1). The 3-point Lagrangian interpolation scheme will also be used for temperature interpolation and the associated appendix discussed the method used for temperature/pressure interpolations from the laboratory measurement grids to the TES table *T/*P grids.

3.3.7.4 Pressure Interpolation

An advantage of using fixed pressure levels bounding the TES forward model atmospheric layers is the ability to ignore the interpolation of species absorption coefficients in pressure at all layers except two: the layer nearest the Earth's surface in the nadir case, and the tangent layer in the limb case. We have conducted a study to examine the changes in layer effective pressures for all the possible layer atmospheric temperature gradients and the effect of pressure interpolation on the simulated spectral radiance.

With a fixed layer boundary pressure, the change in the layer effective pressure ($\overline{P}$) depends mainly on the changes of the boundary temperatures and on the instrument viewing direction. Fifteen averaged temperature profiles of 1997 are calculated using data obtained from the NOAA CDC site (http://www.cdc.noaa.gov/cdc/reanalysis): global averaged, global maximum, global minimum, four seasons for tropics, four seasons for mid-latitude, and four seasons for the polar region. We also constructed an extreme temperature profile: ± 20 K on odd and even levels of the global averaged temperature points, respectively. These temperature profiles are used to calculate the layer effective pressures for 24 atmospheric layers between 1000 and 10 hPa for three TES viewing modes: nadir angle = 0, nadir angle = 45°, and a limb viewing case. A standard $\overline{P}$ profile is calculated using the global average temperature profile and for the nadir angle = 0 case. This standard layer effective pressure profile is the pressure profile used to generate the species absorption coefficient tables.

In the two nadir cases, the layer $\overline{P}$ for the considered temperature profiles are seen to be extremely close to the standard $\overline{P}$ profile. The unrealistic temperature profile results in less than

0.3% differences in $\overline{P}$, and all the other realistic temperature profiles result even small differences in $\overline{P}$ (less than 0.11%).

In the limb case, the largest disagreement in $\overline{P}$ occurs at the tangent layer (~3.2%) for all the temperature profiles, comparing to the nadir standard $\overline{P}$. The differences in the layer next to the tangent layer are reduced to about 0.5%. We also found that the effect of different temperature profiles on the limb tangent layer $\overline{P}$ is very small, which means that we may need a standard limb tangent layer $\overline{P}$ profile for the limb case if the ~3.2% difference is a problem in the level 2 process.

In conclusion, the standard $\overline{P}$ profile calculated using global averaged temperature profile for TES nadir ($\theta = 0^0$) mode can be used as the pressure grids for the absorption coefficient tables, and the interpolation in pressure is not needed for most cases. The two exceptions are the limb tangent layer and the surface layer. In the case of the limb tangent layer, the absorption coefficient table at the standard limb tangent layer $\overline{P}$ profile calculated using global averaged temperature profile for TES limb mode may be needed. In the case of the surface layer, which will be thinner than our fixed layers near the surface, the option would be to perform pressure interpolation if it is necessary. The preliminary comparisons of spectral radiances using the standard $\overline{P}$ profile and the "real" $\overline{P}$ profiles strongly support this conclusion (the radiance differences for the nadir case are less than 0.05% and for the limb case are less than 0.1%).

3.3.7.5 Isotopes

The spectral line intensities used by TES are weighted by its natural terrestrial isotopic abundance as in HITRAN 2000 (Table 3-3). The selection of a particular molecular species will include the contribution of all associated isotopes at their respective natural terrestrial abundances independent of altitude. To study the dependence of a given isotopes with altitude, e.g. HDO (162), that isotope will be treated as a separate molecular species.

Table 3-3: Isotopic Abundances incorporated in TES line parameters from HITRAN 2000

Molecule Number	Molecule	Isotope	Fractional Abundance	Spectral region (cm^{-1})
1	H_2O	161	0.997317	0-22657
		181	0.00199983	6-13901
		171	0.000372	6-11144
		162	0.00031069	0-5508
		182	0.000000623	1173-1685
		172	0.000000116	1234-1599
2	$C0_2$	626	0.98420	442-9649

Molecule Number	Molecule	Isotope	Fractional Abundance	Spectral region *(cm* ^{1})
		636	0.01106	497-8105
		628	0.0039471	507-8133
		627	0.000734	554-6962
		638	0.00004434	567-4947
		637	0.00000825	584-3642
		828	0.0000039573	615-3670
		728	0.00000147	626-2359
3	0_3	666	0.992901	0-4061
		668	0.00398194	0-1178
		686	0.00199097	1-1146
		667	0.000740	0-821
		676	0.000370	0-823
4	N_20	446	0.990333	0-5132
		456	0.0036409	5-3463
		546	0.0036409	4-3474
		448	0.00198582	555-3464
		447	0.000369	586-3483
5	CO	26	0.98654	3-8465
		36	0.01108	3-6279
		28	0.0019782	3-6267
		27	0.000368	3-6339
		38	0.00002222	3-6124
		37	0.00000413	1807-6197
6	CH_4	211	0.98827	0-6185
		311	0.01110	0-6070
		212	0.00061575	7-3307
7	O_2	66	0.995262	0-15927
		68	0.00399141	1-15852

Molecule Number	Molecule	Isotope	Fractional Abundance	Spectral region *(cm ^{1})*
		67	0.000742	0-14537
8	NO	46	0.993974	0-3967
		56	0.0036543	1609-2061
		48	0.00199312	1601-2039
9	$S0_2$	626	0.94568	0-4093
		646	0.04195	2463-2497
10	$N0_2$	646	0.991616	0-3075
11	NH_3	4111	0.9958715	0-5295
		5111	0.0036613	0-5180
12	$HN0_3$	146	0.989110	0-1770
13	OH	61	0.997473	0-19268
		81	0.00200014	0-7
		62	0.00015537	0-2
14	HF	19	0.99984425	41-11536
15	HCl	15	0.757587	20-13458
		17	0.242257	20-10995
16	HBr	19	0.50678	16-9759
		11	0.49306	16-9758
17	HI	17	0.99984425	12-8488
18	ClO	56	0.75591	0-1208
		76	0.24172	0-1200
19	OCS	622	0.93739	0-4119
		624	0.04158	0-4116
		632	0.01053	0-4013
		623	0.007399	509-4116
		822	0.001880	0-4042
20	H_2CO	126	0.98624	0-2999
		136	0.01108	0-73

Molecule Number	Molecule	Isotope	Fractional Abundance	Spectral region (cm^{-1})
		128	0.0019776	0-48
21	HOCl	165	0.75579	0-3800
		167	0.24168	0-3800
22	N_2	44	0.9926874	1922-2626
23	HCN	124	0.98511	2-3422
		134	0.01107	2-98
		125	0.0036217	2-101
24	CH_30	215	0.74894	679-3173
		217	0.23949	674-3162
25	H_20_2	1661	0.994952	0-1500
26	C_2H_2	1221	0.97760	604-3359
		1231	0.02197	613-3375
27	C_2H_6	1221	0.97699	720-3001
28	PH_3	1111	0.99953283	708-1411
29	COF_2	269	0.98654	725-1982
30	SF_6	29	0.95018	940-953
31	H_2S	121	0.94988	2-4257
		141	0.04214	5-4172
		131	0.007498	5-4099
32	HCOOH	126	0.983898	1060-1162
33	$H0_2$	166	0.995107	0-3676
35	$ClON0_2$	5646	0.74957	763-798
		7646	0.23970	765-791
36	NO^+	46	0.993974	1634-2531
38	$C2H_4$	221	0.9773	701-3243
		231	0.02196	2947-3181

3.3.8 ABSCO Databases

3.3.8.1 Line Parameters

The line-by-line portion of the TES spectroscopic database contains transitions for individual infrared active molecular species and their isotopomers within the spectral range defined by the TES nadir and limb observations. The numbering of the species, the format and definition of the parameters, and the contents of the TES spectral parameters database are currently identical to those in the 1996 HITRAN compilation [Rothman *et al.,* 1998]. The status and quality of the HITRAN parameters have been reviewed by Rothman *et al.* [1998]. Here we highlight the known, key limitations of the 1996 HITRAN parameters for the molecules and spectral regions of importance to TES, laboratory work in progress, and published results not incorporated in HITRAN. As was done for the ATMOS project [Brown *et al.,* 1996], the TES spectroscopic database will be updated to satisfy the specific needs of the TES project. The discussion, shown in Appendix 3.3.8.1, proceeds on a molecule-by-molecule basis, with the anticipated changes described for each molecule in ascending wavenumber order.

3.3.8.2 Cross-Sections

For heavy molecular species such as chlorofluorocarbons (CFC's), hydrochlorofluorocarbons (HCFCs), SF_6, N_2O_5, and, in part, $ClONO_2$, spectral absorption cross-sections measured at atmospheric conditions are required [Massie *et al.,* 1985; Camy-Peyret *et al.,* 1987 and Massie and Goldman, 1992]. This is essential, since the small rotational constants, low vibrations and strong hot bands of such molecules preclude complete modeling of the individual line transitions. The 1986 and 1992 editions of the HITRAN compilation introduced temperature-dependent cross-sections but neglected the effect of pressure broadening [Ballard *et al.,* 1988, McDaniel *et al.,* 1991; Massie *et al.,* 1991; Cantrell *et al.,* 1988]. Moré recently, pressure-temperature cross-sections sets have become available [Varanasi *et al.,* 1992a; Varanasi, 1992b; Varanasi, 1992c].

The absorption cross-section, κ_ν, is defined as

$$\kappa_\nu = (-\ln \mathcal{T}_\nu)/nL \qquad (3.28)$$

in terms of the spectral transmittance $\mathcal{T}$ at wavenumber ν, temperature T and pressure P, of column density n along an optical path of length L (cm). It is presented at several (T,P) combinations representing atmospheric layers given in commonly tabulated atmospheric models as well as conditions encountered in the polar regions.

Table 3-4 shows the datasets that have been adapted for TES, from an updated set of measurements provided by Varanasi [private communication, 1997]. These form an extension of the cross-sections of CFC-11, CFC12, HCFC-22, and SF_6 provided by Varanasi for 1996 HITRAN [Varanasi and Nemtchinov, 1994; Li and Varanasi, 1994; Varanasi *et al.,* 1994; Rothman *et al.,* 1998], and also include CF_4. The cross-sections of CCl_4 listed in 1996 HITRAN, which originate from the work of Orlando *et al.* [1992] have been replaced by those of Varanasi, for TES. These cross-sections were measured using a high-resolution Fourier-transform spectrometer. For these species, a spectral resolution of 0.03 cm^{-1} was used for most of the

broadening pressures used in the experiments, while at 40 torr and lower 0.01 cm^{-1} was used. The data were obtained at temperatures between 180 and 296 K and are free from instrumental distortion, since the spectra were recorded at a spectral resolution that was sufficiently high at each broadening pressure used.

Table 3-4: IR cross-section data prepared for TES

Molecule	*Wavenumber Range (1/cm)*	*Temperature Range (K)*	*Pressure Range (torr)*	*Number of P,T sets*
CCl_4	770-812	208-297	8-760	32
CFC-11	810-880	190-296	8-760	55
(CCl_3F)	1050-1120	190-296	8-760	55
CFC-12	810-965	190-296	8-760	51
(CCl_2F_2)	1040-1200	190-296	8-760	51
HCFC-22	760-860	216-294	40-760	7
($CHClF_2$)				
SF_6	925-955	216-295	25-760	7
CF_4	1250-1290	180-296	8-760	54
HFC134a	1000-1350	253-287	0	3
(CFH_2CF_3)				

For the purpose of TES codes, the cross-sections, which are originally given at different spacings (chosen according to resolution and pressure) were interpolated to a constant step of 0.0025 cm^{-1}. A special P-T interpolation was devised for conditions different from the laboratory data. Table 3-4 shows the data sets prepared on the TES system and Appendix 3.3.8.2 describes the P-T interpolation program XSFINT.

The data are stored in HITRAN format, i.e. as separate files for each individual molecule. Each portion of the file corresponding to a particular temperature-pressure pair begins with a header that contains information on the wavenumber (cm^{-1}) range, number of cross-section data in this set, temperature (K), and pressure (torr). The maximum value of the absorption cross-section (cm^2/molecule) and additional information containing the reference to that observation are also presented in each header. The wavenumber spacing of the cross-section listings is uniform for each of the pressure-temperature sets, and is determined by taking the difference between the maximum and minimum wavenumber and dividing by the number of points (cross-section data in this set).

The rest of the molecular cross-sections sets are taken from the 1996 HITRAN database, which, compared to 1992 HITRAN, provides an update for $ClONO_2$. In addition to the $ClONO_2$ ν_4 line parameters, new cross-sections for the $ClONO_2$ in the 1265-1325 cm^{-1} region at 201, 211, and 222 K are available from 1996 HITRAN, as provided by Orphal *et al.* [1994].

The increased use of hydrofluorocarbons (HFCs), which are expected to replace CFCs and HCFCs in many applications in order to reduce the deleterious effects of released chlorine on the atmospheric ozone layer, will add another absorber in the IR 'window' region, 8-12 μm. Cross-

sections data for a number of HCFCs have become available [Clerbaux *et al.,* 1993; Smith *et al.,* 1996]. Moré recently, Smith *et al.* [1998] determined the cross-sections of HFC-134 (CHF_2CHF_2) and HFC-143a (CF_3CH_3). All of these data are already available on the GEISA database [Jacquinet-Husson *et al.,* 1998] and will also be available on a future edition of HITRAN. At this time we prepared in TES format the cross-sections of HFC-134a (from Clerbaux *et al.,* 1993) which is considered as one of the most popular HCFC's.

3.3.8.3 Aerosols

The HITRAN 1996 compilation [Rothman *et al.,* 1998] contains auxiliary tables in ASCII for various atmospheric particles. The index of refraction tables include water and ice (the composition of cloud particles), aqueous sulfuric acid (the composition of volcanic aerosols), and nitrate acid trihydrate and aqueous HNO_3/H_2O (possible compositions of polar stratospheric clouds). The tables have individual wavenumber ranges, increments, and data formats. A description of the individual files is reported in Table 10 of Rothman *et al.* [1998]. Massie [1994] reviewed the indices of refraction which form the basis of the files on HITRAN 1996 [Rothman *et al.,* 1998]. Note that most of the available measurements were obtained only at room temperature.

The emission measurements obtained by TES will display enhanced radiances due to the scattering and absorption by aerosol particles. As is well known, sulfate aerosol injection into the stratosphere after a major volcanic eruption will greatly increase radiance levels. At such times, strong aerosol bands appear throughout infrared limb spectra [Rinsland *et al*., 1994].

3.3.8.4 MT_CKD Continuum

A new continuum model has been developed for TES, which includes continua due to water vapor, carbon dioxide, oxygen and nitrogen. The water vapor continuum [Mlawer *et al.,* 2003; Clough *et al.,* 1989] and carbon dioxide continua are developed and utilized such that when the continuum contribution is added to the line by line component, agreement with observation is achieved. These continua have slow spectral dependence and known thermodynamic scaling. The continua for oxygen [Thibault *et al.,* 1996] and nitrogen [Lafferty *et al.,* 1996] are due to collision induced effects resulting from collisions with the respective molecule and the molecules comprising the air.

The water vapor continuum plays an important role in atmospheric radiative transfer providing increased opacity between spectral lines over the full spectral region from the microwave to the visible. The continuum is important to the physical solution of the inverse problem, the remote sensing of atmospheric state to retrieve temperature, water vapor, and trace species profiles as well as surface properties. There are two components to the continuum: the self-broadened continuum (C_s), dependent on the square of the partial pressure of water vapor, and the foreign-broadened continuum (C_f), dependent on the product of the water vapor partial pressure and the dry air pressure. As a consequence the self-broadened continuum tends to be more important in the lower atmosphere while the foreign-broadened continuum tends to be more important in the middle to upper troposphere. The general formulation for the absorption coefficient associated with the continuum is given by

$$\kappa_c = \nu \tanh(hc\nu / 2k_B \mathrm{T}) \left[(\rho_{H_2O} / \rho_0) \tilde{C}_s(\mathrm{T}) + (\rho_{air} / \rho_0) \tilde{C}_f(\mathrm{T}) \right] \qquad (3.29)$$

with the usual definitions.

The current water vapor continuum model, MT_CKD_1.0 [Mlawer *et al.,* 2003] has evolved from the CKD approach [Clough *et al.,* 1989] to modeling the continuum, which utilitized a single line shape for all water vapor transitions from the microwave to the visible. The CKD model had been modified a number of times from its original version to provide improved agreement with measurements. Examples of such observationally-based modifications include: (1) the measurement of the downwelling radiance at Kavieng, New Guinea by Han *et al.* [1997] which indicated that the self-broadened continuum gave rise to an 8K error in brightness temperature at 950 cm^{-1} for an atmosphere with ~6 precipitable cm of water vapor; (2) a clear indication that the foreign continuum was in error in the wings of the 1600 cm^{-1} water vapor band as observed by Revercomb and colleagues at the U. of Wisconsin; and (3) a measurement of the downwelling radiance in the cold, dry conditions of the arctic [Tobin *et al.*, 1999] indicated that the foreign continuum had significant errors from 400-600 cm^{-1}. The first two of these modifications are significant in the context of remote sensing from space. Of interest is the fact that the spectral character of the continuum in the 900-950 cm^{-1} window has the effect of decoupling the atmospheric radiance of the moist atmosphere in the boundary layer from the surface emission, thereby significantly improving the accuracy with which boundary layer water vapor and surface brightness temperature can be retrieved (given the spectral emissivity of the surface). Examples of the role of the continuum for atmospheric observations may be found in Clough *et al.* [1992] and Mlawer *et al.* [1997]. The CKD continuum models have provided generally acceptable results in measurement-model comparisons in a variety of spectral regions (e.g. Clough, 1995).

As a result of more stringent accuracy requirements for remote sensing applications and with the availability of improved atmospheric observations, an entirely new water vapor continuum formulation has been developed [Mlawer *et al.,* 2003]. The MT_CKD continuum is based on a new formulation in which the self and foreign continuum models are each based on the contributions from two components: a collision induced component and a line shape component. This change in perspective has resulted from the difficulty in developing a line shape formalism, such as in CKD, based on sound physics that explains the magnitude of the increased absorption in the intermediate wing over that provided by the impact approximation. The two components in MT_CKD are applied consistently to all water vapor lines from the microwave to the visible, and the results summed to obtain self and foreign continuum coefficients from 0-20,000 cm^{-1}. Eight and seven parameters are needed to specify the two components for the self and foreign continua, respectively, which are sufficient to generate the entire continuum spectrum over this spectral domain. The ratio of the self continuum at 296 K to that at 260 K has been kept the same as in the CKD model. The only temperature dependence for the foreign continuum arises from the radiation term as with CKD. The MT_CKD model (as with CKD) should be regarded as a semi empirical model with strong constraints provided by the known physics. The principal consequences for remote sensing are with respect to the foreign continuum, important in the upper troposphere for the retrieval of water vapor and for the background spectral radiance for retrieval of trace species including NO.

3.4 JACOBIANS

The sensitivity of spectral radiance at the satellite to the perturbations of retrieved parameters included in the retrieval vector is the Jacobian matrix, **K**. In general, $\mathbf{K} = \partial\mathbf{F}/\partial\mathbf{x}$, where **F** is the forward model radiance and **x** represents a retrieved parameter, such as temperature at level *l*.. In our retrievals, we cannot assume we are close to a linear solution. Therefore, Jacobians are recalculated for each iteration of a retrieval, using updated parameters.

3.4.1 Finite Difference

Evaluating Jacobians using a finite difference method is straightforward. For example, **K** can be calculated as $[\mathbf{F}(\mathbf{x}+\Delta\mathbf{x}) - \mathbf{F}(\mathbf{x})]/\Delta\mathbf{x}$, where $\Delta\mathbf{x}$ is a small perturbation of parameter **x**. If terms $\mathbf{F}(\mathbf{x}+\Delta\mathbf{x})$ are calculated for all retrieved parameters by carrying out forward model many times, the algorithm is not very efficient considering that many layer quantities (see 3.3.1.3 and 3.3.1.4) will be unnecessarily calculated over and over again. The computation, if not optimized, can be expensive and the accuracy of the derivatives is more prone to numerical error and nonlinear contributions. For these reasons, we compute analytic Jacobians for operational retrievals and retain the finite difference method for validating analytic Jacobians. Although accelerated methods for computing finite difference are possible, they have very low development priority since they would not be used operationally. For validating analytic Jacobians, symmetric finite differences will be used, where the finite difference is computed with both positive and negative perturbations to the retrieval parameter.

3.4.2 Analytical

In evaluating analytic expressions for the terms in the Jacobian matrix, there are some cases where approximations represent a significant computational savings with only marginal impact on accuracy. We have never placed a requirement on the accuracy of analytic jacobians. From experience, accuracy around 5% is sufficient for retrieval convergence to a solution within estimated error, in most cases. However, jacobians are also used to compute retrieval errors, as well as in assimilation (L4) algorithms. Data assimilation would probably place the most stringent requirements on jacobian accuracy, but algorithms have not yet been developed for the assimilation of TES data. A jacobian accuracy requirement is therefore TBD. For this version of the L2 ATBD, we will set a goal of 1% accuracy (at the maximum absolute value in a frequency range) for analytic jacobians as compared to finite difference.

3.4.2.1 Temperature and Gas Concentrations

Due to the form of the radiative transfer equation (3.10), the analytic derivative of the radiance at the satellite with a change in parameter x_l at level l, is most expeditiously obtained in terms of associated layer quantities, so that we have

$$\frac{\partial L_{sat}}{\partial x_l} = \sum_j \frac{\partial L_{sat}}{\partial \bar{x}_j} \frac{\partial \bar{x}_j}{\partial x_l} \tag{3.30}$$

in which x_l is an element of the retrieval vector associated with level l and $\overline{x}_j$ is the associated layer quantity for layer j. Note that in general, x may be mixing ratio (log mixing ratio) or temperature in this context.

In this section we focus on the computation of $\frac{\partial L_{sat}}{\partial \overline{x}_j}$, noting that $\frac{\partial \overline{x}_j}{\partial x_l}$ is independent of wavenumber. (These layer-to-level partial derivatives are discussed in Appendix A3.4.)
For the layer quantities, it is useful to separate the jacobian calculation into partial derivatives with respect to layer total optical depth (τ_l) and Planck function (B_l) via the chain rule. Differentiating Equation (3.10), we obtain

$$\frac{\partial L_{sat}}{\partial \overline{x}_l} = \frac{\partial L_{sat}}{\partial \tau_l} \frac{\partial \tau_l}{\partial \overline{x}_l} \tag{3.31}$$

for gas species, and

$$\frac{\partial L_{sat}}{\partial \overline{T}_l} = \frac{\partial L_{sat}}{\partial \tau_l} \frac{\partial \tau_l}{\partial \overline{T}_l} + \frac{\partial L_{sat}}{\partial B_l} \frac{\partial B_l}{\partial \overline{T}_l} \tag{3.32}$$

for layer temperature $\overline{T}_l$. This approach has the advantage of relatively simple expressions for the derivatives of τ_l with respect to log mixing ratio and temperature. It is also compatible with the modularity designed into our code where quantities associated with optical depth are computed first to determine whether they can be reused from one ray calculation to the next, while quantities associated with layer to layer radiative transfer are used locally in different function. Appendix A3.4 describes the above terms in detail. In summary, the partials for all gas species but H_2O have very simple jacobians, while H_2O has additional terms for line self-broadening, continuum and integrated path amount dependence. Temperature jacobians include terms for gas species line absorption, continuum absorption, dependence of the integrated path amount and Planck (or effective Planck) function dependence. For absorption coefficient tables, the temperature jacobians for species line absorption are a straightforward differentiation of the temperature interpolation coefficients.

3.4.2.2 Surface and Opaque Cloud Boundary Properties

For lower boundaries that are either the earth's surface or opaque clouds, we will retrieve a single "surface" temperature, T_{sfc}, and coarse frequency resolution functions for emissivity, $\varepsilon(\nu)$, and possibly albedo, $\alpha(\nu)$. The Jacobians for these parameters are calculated analytically. Derivations are straightforward given that the surface contribution to the total radiance is a separate term in the radiative transfer equation (3.10). Emissivity and albedo functions will be expressed as tabulated quantities on a course spectral grid (10 cm^{-1} spacing). Assuming piece-wise linear interpolation, for tabulated $\varepsilon(\nu)$ on a frequency grid with any two adjacent table points at ν_a and ν_b, the emissivity at ν, where $\nu_a \le \nu \le \nu_b$, is given by

$$\varepsilon(\nu) = \left[\frac{\nu_b - \nu}{\nu_b - \nu_a}\right]\varepsilon_a + \left[\frac{\nu - \nu_a}{\nu_b - \nu_a}\right]\varepsilon_b \tag{3.33}$$

Assuming the albedo is defined on the same frequency grid, we have the following surface Jacobians:

$$\frac{\partial L_{sat}}{\partial T_{sfc}} = \varepsilon(\nu)\frac{\partial B}{\partial T_{sfc}}\mathcal{T}_{0,L} \tag{3.34}$$

$$\frac{\partial L_{sat}}{\partial \varepsilon_a} = \left[\frac{\nu_b - \nu}{\nu_b - \nu_a}\right] B\left(\nu, T_{sfc}\right)\mathcal{T}_{0,L} \tag{3.35}$$

$$\frac{\partial L_{sat}}{\partial \varepsilon_b} = \left[\frac{\nu - \nu_a}{\nu_b - \nu_a}\right] B\left(\nu, T_{sfc}\right)\mathcal{T}_{0,L} \tag{3.36}$$

$$\frac{\partial L_{sat}}{\partial \alpha_a} = \left[\frac{\nu_b - \nu}{\nu_b - \nu_a}\right] L_0^{\downarrow}\mathcal{T}_{0,L} \tag{3.37}$$

$$\frac{\partial L_{sat}}{\partial \alpha_b} = \left[\frac{\nu - \nu_a}{\nu_b - \nu_a}\right] L_0^{\downarrow}\mathcal{T}_{0,L} \tag{3.38}$$

3.4.2.3 Pointing

In the limb case, retrieving instrument pointing angle needs to be carried out as part of the profile retrievals. Recall that the TES forward model radiances for the rays along the field of view directions starting from pre-defined tangent pressure levels are interpolated in zenith angle and convolved with the instrument field of view function (Section 3.3.6). Only one angle, θ_p, the instrument pointing angle (e. g. the zenith angle for the optical axis) determines the relative "alignment" between the pixel dependent FOV functions and the ray radiances. Since each detector has $\theta_d = \theta_p + \Delta\theta_d$, the derivatives of detector radiance with respect to θ_p are

$$\frac{\partial L_{sat}}{\partial \theta_p} = \frac{\partial L_{sat}}{\partial \theta_d} \tag{3.39}$$

Formulas for this analytic jacobian are given in Appendix A3.4.7. These derivatives with respect to pointing angle have been validated using finite difference jacobians where the finite difference is computed by perturbing the pointing angle, which adjusts the FOV functions relative to the forward model rays, then performing the FOV convolution again. The finite difference jacobian is the change in radiance from the perturbed and reference case divided by the delta angle.

3.5 RETRIEVAL

3.5.1 General Strategy

Our goal is to have a single, flexible, efficient retrieval code that can be used in a variety of ways under control of a strategy table. The approach is to use non-linear least squares spectral fitting of retrieval parameters, based on the so-called optimal estimation technique [Rodgers, 1970]. The retrieval parameters will be retrieved in a series of steps, with retrieved quantities from one

step usually feeding the next as fixed inputs. In some cases, parameters will be retrieved in multiple steps, such as in initial guess refinement (see Section 3.5.1.4).

Each limb or nadir target scene will be treated independently. This is the simplest approach, and allows partial results from incomplete observation sets. Computational gains from parallelization can be achieved by processing multiple target scenes at the same time.

3.5.1.1 Strategy Table Selection

The particular strategy table data that will be used to retrieve a target scene will be selected based on the following information:

- view mode (nadir or limb)
- initial guess override (to specify an initial guess from a previous retrieval result)
- surface type (land, ocean, or cloud)
- meterological data available (first look, late look, or none)

In the future, other table selection parameters may be identified. At present, the basic difference between strategy tables is the retrieval order, species retrieved, and initial guess source. However, different strategy tables may also specify different constraint types, convergence criteria, or retrieval control parameters. The flexibility of the strategy tables is used in production and will also be used for testing and comparing new retrieval strategies.
The Table 3-5 shows some retrieval step scenarios. These steps are specified in the strategy table and their content is flexible, both with regards to what is retrieved and to the parameters controlling the retrieval. These strategies will be modified in the light of experience with real data.

Table 3-5: Sample Retrieval Step Scenarios

Viewing_Mode		NADIR	NADIR	LIMB
Surface		LAND/CLOUD	OCEAN	-
Selected table→		**Table 1**	**Table 2**	**Table 3**
Retrieval steps	1	**TSUR & EMIS**	**TSUR**	**pointing**
↓	2	**TATM**	**TATM**	**TATM**
	3	**H2O**	**H2O**	**H2O**
	4	**TATM & H2O**	**TATM & H2O**	O3
	5	O3	O3	CH4
	6	CH4	CH4	CO
	7	CO	CO	HNO3
	8			NO2

Note: **BOLD** indicates retrieval order is important.

Table 3-5 (columns 2 and 3) show the difference in strategy between a land and an ocean target scenes retrieval. The difference is whether emissivity (EMIS) is retrieved. For TES nadir data taken over water, we would fix the emissivity parameters to the known water emissivity spectrum and retrieve only the "skin" temperature (TSUR). This may also be possible for some well-characterized scenes over ice. For land targets, the emissivity spectrum will be retrieved

using reasonable first guess emissivity values (described in Section 3.3.2.1). We have successfully performed land emissivity retrievals with silicate features using AES data and we found that emissivity parameters need additional constraints so that they are limited to physical values (*i.e.*, they must be less than 1). These constraints can be specified in the strategy table. The Strategy Tables in Table 3-5 are examples that show the flexibility of the Tables to specify any combination of retrieval species in any order.

All the sample tables in Table 3-5 show each species retrieved once. However, O_3 (or any other species) may be retrieved in more than one step. Table 3-6 shows nadir retrieval step scenario using initial guess refinement for O_3. O_3-IG-refine is an initial guess refinement step (see Section 3.5.1.4). This step will have a different map and possibly different microwindows than the second O_3 step, all of which can be specified in the strategy tables. These details are not shown here but are easily specified in the strategy tables.

Table 3-6: Strategy table for O3 initial guess refinement.

Retrieval steps
EMIS & TSUR
TATM
H2O
TATM & H2O
O3-IG-refine
O3
CH4
CO

Additionally, some final steps may be done following the above retrieval steps:

- retrieval of all species simultaneously for more improvement or error analysis
- full filters radiance calculations for quality control

In the limb case, the filters radiance calculation will be done for each pixel. In the nadir case, this will actually be a retrieval of surface emissivity using the already determined atmospheric state.

3.5.1.2 Target-level Suppliers

The task of assembling data to run retrieval steps is divided into conceptual units called suppliers. Each supplier is designed to operate with a degree of independence to accomplish a specific task. The target level suppliers assemble the data needed before the first retrieval step begins, and to create data which be used throughout all the retrieval steps. The step level suppliers assemble the data needed for each retrieval step, and which may vary from step to step. Some suppliers that are conceptually step-level are moved to the target level because their data is needed before the first retrieval step, for example microwindows. Microwindows for all steps are determined at the target level so that all FM species list can be determined and so that the FM radiance can be generated for simulation mode.

A table showing the suppliers and supplier dependencies is shown in Table 3-7.

The target level suppliers are (see appendix for descriptions):

- Strategy Table
- Surface pressure
- Forward model pressure
- Target level full state vector (for initial guess)
- True full state vector (if needed)
- Target level emissivity
- Target level map
- Simulated spectrum
- Measured spectrum
- Target level microwindows definitions
- Target level error covariance

3.5.1.3 Step-level Suppliers

The step level suppliers assemble the data needed for one retrieval step. A step will be defined by the following parameters:

- quantities to be placed in the retrieval vector
- first guess for each of these quantities
- *a priori* for each of these quantities
- quantities to be used as forward model parameters
- forward model parameters
- numerical method to be used to minimize the cost function
- subset of the measured spectrum to be used (may be detector-dependent)
- stopping criteria

These pieces of information will be collected by step level suppliers, or are specified as step control parameters in the strategy table. The step level suppliers are (see appendix for descriptions):

- Step level map
- Step level microwindows definitions
- A priori constraint vector
- A priori constraint matrix
- Microwindows radiances
- Emissivity a priori
- Step level full state vector
- Retrieval levels (subsupplier to Step level map)

The suppliers must collect data in a particular order, because many depend on data from other suppliers. The ordering and dependencies are shown in Table 3-7.

Table 3-7: Supplier Dependencies

Order	Supplier (Sub supplier) → means an either/or case for supplier choice	Dependency
1	Target Scene Attributes	
2	Strategy Table	Target Scene Attributes
3	Target Level Microwindows Definitions	Target Scene Attributes Strategy Table
4	Target Level FMPressures (includes Target Level Surface Pressure)	Strategy Table and initial T_{atm} and H_2O which are needed to calculate surface pressure
5	Target Level Map (includes Target Level Retrieval Levels)	Target Level FMPressures Strategy Table
6	Target Level FSV (includes Target Level Emissivity)	Strategy Table Target Level Microwindows Definitions Target Level FMPressures Target Level Map
7	Target Level TFSV (includes Target Level Emissivity)	Strategy Table Target Level Microwindows Definitions Target Level FMPressures Target Level Map
8	Target Level Error Covariance (includes Emissivity A Priori Climatological Covariance)	Strategy Table Target Level FMPressures
9	→Target Level Full Apodized Measured Spectrum (FAMS) →Target Level Full Apodized Measured Spectrum [*Simulation mode*]	Strategy Table Target Level TFSV Target Level FMPressures Target Level Microwindows Definitions
10	Target Level Cloud	Strategy Table Target Level FSV Target Level Microwindows Definitions
----------below is repeated for every step----------		
11	Step Level Map	Strategy Table Target Level Map
12	Step Level FSV	Target Level FSV
13	Step Level A Priori Constraint Vector (includes Emissivity A Priori Constraint Vector)	Strategy Table Target Level FMPressures Step Level Map Step Level FSV
14	Step Level A Priori Constraint Matrix (includes Emissivity A Priori Constraint Matrix)	Strategy Table Target Level FMPressures Step Level Map Step Level FSV Step Level A Priori Constraint Vector
15	Microindows Radiances	Target Level Microwindows Definitions Target Level FAMS

3.5.1.4 Initial Guess Refinement

The purpose of initial guess refinement is to start the relatively expensive optimal estimator close to the final solution, so that as few iterations as possible are required. Thus a computationally inexpensive *ad hoc* non-optimal retrieval method is used to find the region of the solution. \

In the nadir case, a preliminary retrieval step could be to treat the troposphere and stratosphere as two columns. This step is to fit the measurement spectrum to solve for the two scale factors that would shift the initial guess constituent profile, and this refined profile would then be the initial guess profile used for the full optimal retrieval at more levels [S. Clough *et al*, 1995].

Alternatively, the so-called shape retrieval could be applied to either limb or nadir retrievals. This mapping is constructed to retrieve the broad features of the ozone profile such as the mean and gradient of ozone in the troposphere as well as the peak and width of the stratospheric ozone shape [Clough *et al*, 2002; Bowman *et al*, 2002]. The results of the shape retrieval are then used as the initial guess for a subsequent retrieval based on a finer discretization of the profile.

3.5.1.5 Strategy for Limb Pointing Retrieval

The central problem to be addressed from the spacecraft is the pointing direction of the 2B1 reference focal plane. Once this is known, then the pointing of all pixel elements is established given predetermined focal plane properties. The general strategy will be to utilize the radiance spectrum associated with a pixel having a projection in the upper troposphere to minimize the effects of clouds and to perform a simultaneous retrieval of pointing angle and temperature. The procedure for establishing the radiance field at the satellite and the relevant Jacobians with respect to pointing angle and to temperature is described elsewhere. The initial guess for the pointing angle will be obtained from the encoder associated with the platform spacecraft attitude system. For this stage of the pointing angle retrieval, there will be three elements for the retrieval state vector: (1) the pointing angle, (2) a shift in level temperature for all tangent rays included in the FOV, and (3) a shift in temperature lapse rate for all tangent rays included in the FOV. It will probably be necessary to retrieve temperature profiles somewhat above the tangent layers, but this can be handled in a fashion analogous to the line of sight retrievals appropriate to the nadir case. The spectral region will be that associated with carbon dioxide for which the mixing ratio is assumed known, Figure 3-10, and one in which water vapor plays a minimal role.

Figure 3-10: AFGL Mid Latitude Summer Profiles showing the assumed CO_2 profile.

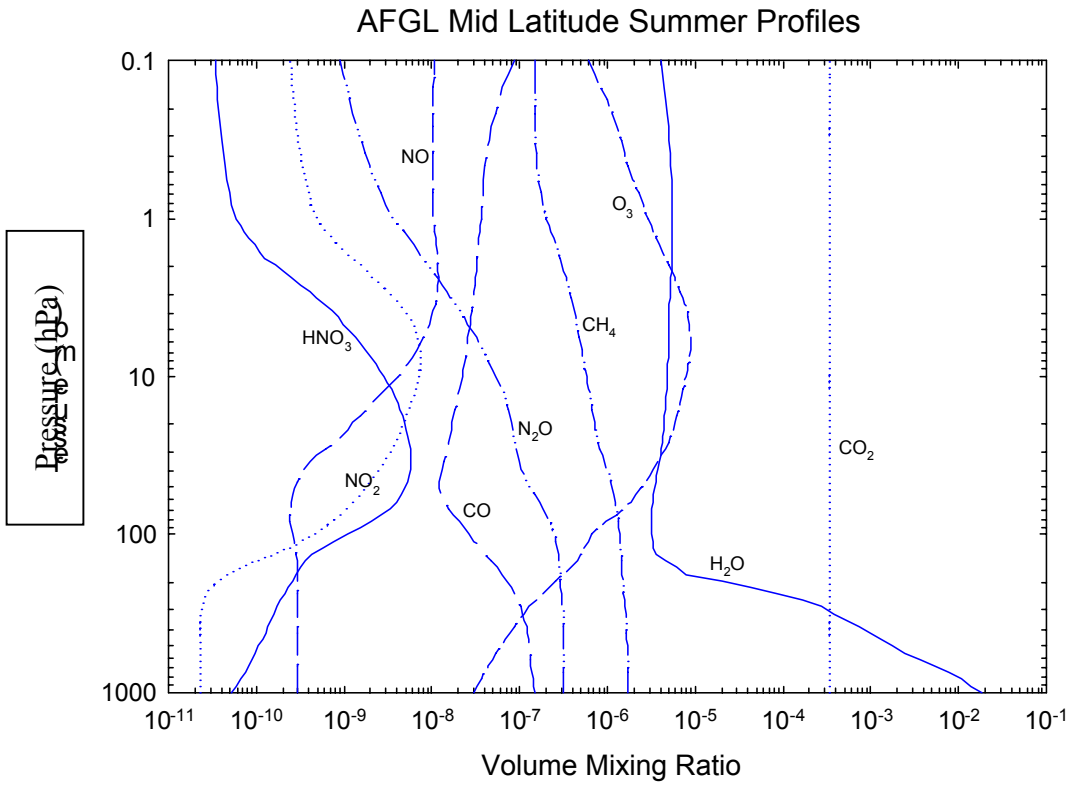

The radiance at the satellite is calculated for each tangent ray required for the FOV convolution. The tangent levels associated with all tangent rays are those of the forward model pressure grid. The zenith angle of

$$n\ R\ \sin(\theta) = \text{Constant} \tag{3.40}$$

$$n_t(R_c + z_t) = R_{cs}\sin(\theta_s) \tag{3.41}$$

$$\theta_s = \text{asin}\{\ n_t(R_c + z_t) / R_{cs}\} \tag{3.42}$$

The dependence of the radiance field on the zenith angle at the satellite, θ_S, is nonlinear and is retrieved as an element of the retrieval vector in the nonlinear retrieval procedure. The Jacobian required is obtained analytically in the course of the FOV convolution. Results from a simultaneous pointing angle / temperature retrieval are provided in Table 3-8. The method, as evaluated through simulations, has been established to be robust and provides excellent accuracy.

Relevant geometrical quantities and horizontal offsets in the direction of the satellite are provided in Table 3-9 as a function of tangent height. These offset values enable the evaluation

of the effects of using a single column for the hydrostatic equation. It may be noted that the FOV is 25 km wide in the horizontal direction perpendicular to the chief ray. The effect on the pointing / temperature retrieval due to an error in the tangent altitude obtained from the hydrostatic equation is small.

This simultaneous retrieval approach should be more critically evaluated with respect to measurement errors greater than those given by the source radiance and with respect to the expected sources of systematic error. The use of pixels in other atmospheric regimes such as the lower stratosphere needs to be explored since there would presumably be less cloud. Also to be explored is the inclusion of the pointing angle in the retrieval state vector for the global fit associated with the retrieval of the temperature field. The relative registration of the four focal plane arrays is determined by the on-board spatial calibration. It may also be tested in space by viewing sharp radiative discontinuities in the scene with both nadir and limb views. These discontinuities can be associated with discontinuities in cloud fields for both the limb and nadir mode and in surface properties (land/ocean) for the nadir view. The relative registration of the pixels is independent of the viewing mode so that there should be consistency between pixel registrations obtained from the two modes. Also to be explored is the retrieval of pointing angle using other spectral regions associated with the other focal planes to further evaluate the consistency of pointing angle among the focal plane arrays.

Table 3-8: Retrieval results for temperature and tangent point for central ray of pixel 11 with TES FOV (tangent height = 11.5 km).

Case	Parameter		Perturbation	Retrieved	Difference	Error (1 σ)
1c	Temperature	(K)	1.0	1.00	0.00	0.02
(700-800 cm-1)	Tangent Point	(m)	500.0	501.00	1.00	1.96
1d (NESR*10)	Temperature	(K)	1.0	0.97	0.03	0.20
(700-800 cm-1)	Tangent Point	(m)	500.0	506.40	6.40	19.60

Table 3-9: Quantities related to the ray trace from the tangent point to the satellite as a function of tangent height. Refraction is included in the ray trace.

Tangent Height	θ_S	$\sin(\theta_S)$	Ψ	bending	Horizontal Offset
(km)	(deg)		(deg)	(deg)	(km)
37.95	115.078	0.90574	17.137	0.003	-163.9
36.80	115.099	0.90557	17.086	0.003	-150.3
35.65	115.121	0.90541	17.035	0.004	-142.3
34.50	115.143	0.90525	16.985	0.005	-134.3
33.35	115.165	0.90509	16.936	0.006	-126.4
32.20	115.187	0.90492	16.887	0.007	-118.6
31.05	115.209	0.90476	16.839	0.008	-110.8
29.90	115.231	0.90460	16.791	0.010	-103.0
28.75	115.252	0.90444	16.744	0.012	-95.3
27.60	115.274	0.90428	16.698	0.014	-87.5

Tangent Height	θ_S	$\sin(\theta_S)$	Ψ	bending	Horizontal Offset
(km)	(deg)		(deg)	(deg)	(km)
26.45	115.296	0.90412	16.652	0.017	-79.9
25.30	115.317	0.90395	16.606	0.021	-72.2
24.15	115.339	0.90379	16.562	0.025	-64.5
23.00	115.360	0.90363	16.518	0.030	-56.8
21.85	115.382	0.90347	16.474	0.036	-49.0
20.70	115.403	0.90331	16.431	0.043	-41.2
19.55	115.424	0.90315	16.388	0.052	-33.2
18.40	115.445	0.90300	16.347	0.063	-25.2
17.25	115.466	0.90284	16.305	0.077	-17.0
16.10	115.487	0.90268	16.265	0.091	-8.7
14.95	115.508	0.90253	16.225	0.110	0.0
13.80	115.528	0.90237	16.186	0.133	9.0
12.65	115.549	0.90222	16.147	0.150	17.3
11.50	115.569	0.90207	16.109	0.167	25.3
10.35	115.589	0.90191	16.071	0.187	33.8
9.20	115.609	0.90176	16.034	0.211	42.7
8.05	115.629	0.90161	15.998	0.237	51.6
6.90	115.649	0.90146	15.962	0.266	60.8
5.75	115.668	0.90132	15.927	0.299	70.3
4.60	115.687	0.90117	15.893	0.334	80.0
3.45	115.707	0.90103	15.859	0.372	89.9
2.30	115.725	0.90089	15.826	0.416	100.4
1.15	115.744	0.90075	15.793	0.470	111.8
0.09	115.760	0.90062	15.764	0.523	122.6

3.5.1.6 Pixel Categorization for Nadir

Clouds and aerosols may impact TES measurements, and as discussed in Section 3.3.3, there are a variety of radiative transfer approaches/approximations that may be used, depending on the presence and characteristics of the clouds or aerosols. Therefore, it is imperative that there be techniques for categorizing the target scenes so that appropriate radiative transfer solution strategies can be applied.

We will use the framework of sorting the data into cases of no clouds, broken or highly inhomogeneous clouds, optically thick clouds, and optically thin clouds. The basic strategy is to examine the brightness temperatures in the atmospheric window regions and use the values and variability of the values to classify the observations. These are methods similar to those proposed for MODIS [Ackerman, *et al.,* 1998)].

The brightness temperature in the 11 micron window will be the primary quantity examined for pixel categorization. This quantity (BT11) is an brightness temperature average over the 867-900 cm^{-1} region with water lines removed. Data from this spectral region will be available in all of the observation strategies and it is comparable to long term nadir satellite measurements from instruments such as AVHRR and MODIS.

Additional L1B parameters that may be calculated are CO_2 line depths. We are studying the possibility of calculating a parameter that can be a quick indication of the reduction in the column CO_2 and therefore an indication that the measurement is not seeing to the surface.

Clear cases will be identified by instances where the BT11 value is within a threshold of the surface temperature and does not have high variability between pixels. Preliminary analysis shows that when absorption effects of the water continuum are taken into effect, a temperature threshold of about 0.5K can be used for high clouds. This threshold will result in a set of clear cases that includes all cases with 'high cloud' optical depths of less than 0.02. Analysis is underway to assess the impact of the definition of 'clear' on retrievals.

Cases of broken or highly inhomogeneous clouds will be identified by high variability in BT11 between pixels. The first approximation of this threshold will be made by examination of global datasets from MODIS. The 1km by 1km 11 micron radiances from MODIS will be converted to brightness temperature, and variability over 5km by 8km areas will be calculated. This variability data will be compared to MODIS cloud mask data over the same footprints to determine the variability threshold. This threshold will be updated after TES data is collected.

Cases of optically thick clouds will be identified by BT11 values that are significantly lower than surface temperatures and do not have high variability. Additional work is underway to develop techniques for differentiating between optically thick low clouds and moderate optical thickness high clouds that would result in the same BT11 temperatures.

Cases of optically thin clouds will be identified by BT11 values slightly lower than surface temperatures. Again, methods of implementing an adaptation of CO_2 slicing to determine cloud height are under investigation.

Another possibility, to be considered for special processing, is to perform the retrieval in the presence of clouds using the philosophy of the CO_2 slicing technique, in conjunction with the NWP temperature field, to determine the effective cloud amount and the cloud-top pressure. The cloud could then be included in the forward model with retrievable optical parameters. The basic CO_2 slicing method is described in many papers (see the description and references in Wylie, *et al.*, 1994) and involves the assumption of a single cloud layer. The cloud-top pressure is determined using the measured radiance and the estimated clear sky radiance for (at least 2) channels with CO_2 lines where the weighting functions peak at different altitudes. This type of algorithm can be tested with many existing data sets such as AES, IRIS-D, IMG and NAST-I. For TES data, in many cases, we should be able to compare the estimated cloud top pressures with CHEM OMI data products.

3.5.1.7 Pixel Categorization in the Limb

Clear pixel detection in the limb view is much more straightforward than in the nadir because the background is cold space rather than a warm surface. It can be accomplished simply by setting a radiance threshold in a window region such as 12 μm. Calculations made for ISAMS [Lambert *et al*., 1996] show limb radiance at 12 μm in the region of 10-20 km as around 0.5 $mW/m^2/sr/cm^{-1}$ in the absence of aerosol, compared with the Planck function at 200K of around

20 mW/m^2/sr/cm^{-1}. Mt. Pinatubo volcanic aerosol was shown to be optically thick in this region, so that we would expect cirrus cloud also to be optically thick.

A more sophisticated cloud detector would be the joint retrieval of temperature and aerosol extinction profiles using an onion peeling process. The lower limit of the limb retrieval would then be set as the lowest altitude where the aerosol extinction is less than some threshold.

3.5.2 Operational Support Products

Operational Support Products (OSP's) are defined as any files that are needed to perform L2 processing. There are two types of OSP's. Internal OSP's are generated by the science team for use by the different Retrieval Strategy suppliers or by ELANOR. External OSP's will be imported from external sources and used directly by the suppliers without modification. The remainder of this section is a list and brief description of some important OSP's.

3.5.2.1 Climatology

The climatological profiles for different chemical species are used to provide

- An initial guess for the retrieval of a given species as mentioned previously.
- "True State" profiles for a given species if there is a need to do a simulated retrieval
- Formulation of *a priori* covariance matrices.

Doug Kinnison at UCAR has provided to all Aura instruments a set of climatological volume mixing ratio profiles calculated using the MOZART 3-D global chemical transport model. This set of climatology profiles provided the basis for what TES will use as for climatology. The MOZART profiles were averaged into longitude and latitude bins with the size varying for different species.

In addition, model profiles for ozone and carbon monoxide from the Harvard GEOS-Chem chemical transport model (http://www-as.harvard.edu/chemistry/trop/geos) were incorporated into the TES climatology.

Earlier sets of MOZART profiles provided climatological values for use in algorithm testing and development.

3.5.2.2 Meteorological Data

The meteorological data used as inputs for the retrieval will be an external OSP. The source of the data will be the GSFC Global Modeling and Assimilation Office (GMAO). The accuracy of the meteorological data, particularly mean sea level pressure, will affect the accuracy of the retrieval products. The meteorological data needs to provide the retrieval strategy suppliers with the following parameters

- Reference Pressure: The mean sea level pressure from the meteorological data, will be used along with the digital elevation model (Section 3.3.2.2) to provide the reference surface pressure for a given target location.
- Temperature profiles and surface temperature to provide *a priori* information (including initial guess) for temperature retrievals.

- Water vapor profiles (including initial guess), to provide *a priori* information for water retrievals.

Currently there is a 14 to 28 day lag between the arrival of the GMAO data at the TES SIPS and the date for which the met data is valid. In order to maintain a consistent data record, if the GMAO data is not available for a given date, there will be no operational L2 retrievals performed on that day's worth of TES data.

3.5.2.3 A priori Climatology Covariance Matrices

The covariance matrices have been calculated using both the MOZART and GEOS-Chem model profiles. They vary with latitude (5 latitude bins). The covariance matrices are calculated on the full TES pressure level grid, resulting in 87×87 matrices.

3.5.2.4 Microwindows

Microwindows and corresponding spectral masks have been developed for all retrieval species (Section 3.5.6).

3.5.2.5 Land Characteristics and Surface Emissivity Properties Databases

These databases must be provided to calculate an *a priori* surface emissivity for retrievals over land (Section 3.3.2.1).

3.5.2.6 Other OSP's

More quantities that will need to be specified (calculated) and then provided to the suppliers include the maps and inverse maps (Section 3.5.3.2), *a priori* constraints (Section 3.5.4), forward model pressure levels (Section 3.2.3) and retrieval levels (species and latitude dependent).

3.5.3 Retrieval Vectors

3.5.3.1 Introduction

In TWPR, an atmospheric profile of a chemical species or atmospheric temperature is defined on the forward model (FM) grid as a function of log pressure. This grid is chosen so that each layer within the grid is homogeneous with respect to temperature, humidity and the trace gases. The retrieval of these profiles, however, is generally not calculated directly on the FM grid. Rather, the profile is represented by some basis in order to constrain the estimated profile. A priori information can be used to further constrain the shape to be physically reasonable. The coefficients of the profile in this basis are retrieved and then "mapped" to the forward model grid. The linear algebraic ordering of these coefficients is called the retrieval vector. This mapping may be non-linear as in the case of retrieval state vector defined on the logarithm of trace gas vmr. This non-linear mapping is chosen to insure positivity of the trace gas quantities and to reduce the dynamic range of retrieved quantitiy, e.g., an ozone profile can have 3 orders of magnitude difference between the troposphere and the stratosphere.

The retrieval vector may be selected from the following, although not all combinations will be valid.

- surface emitting temperature, for each detector
- surface spectral emissivity for a specified spectral range, for each detector
- atmospheric temperature
- constituent mixing ratio (q)
- constituent ln(q)
- aerosol extinction coefficient (or its ln) on a contiguous range of levels of the retrieval grid and for a specified spectral range
- the angle of the boresight of the spectrometer

The quantities not being retrieved at each stage will be treated as forward model parameters.

The choice of basis depends on the specific trace gas. For an initial guess refinement stage of the retrieval the basis is chosen to capture patterns of the profile that are more easily detected, e.g., the shape retrieval [Clough *et al* 2002, Bowman *et al* 2002]. Retrievals of trace gases subsequent to an initial guess refinement retrieval may use a piece-wise linear basis in mixing ratio or the logarithm of mixing ratio. In either case, the basis must also be applied to the Jacobians as well. The mathematical machinery necessary to relate the retrieval vector and its Jacobian to the full state vector and its Jacobian are described in the following section.

3.5.3.2 Mapping

The atmospheric profile is described by the atmospheric full state vector $\mathbf{x} \in \mathbb{R}^M$, the FM radiances by $\mathbf{L} \in \mathbb{R}^N$, and the Jacobian by $\mathbf{K}_x \in \mathbb{R}^{N \times M}$. The retrieval vector, $\mathbf{z} \in \mathbb{R}^{M'}$, is related to the full state vector by a mapping $\mathfrak{M} : \mathbb{R}^{M'} \to \mathbb{R}^M$ so that $\mathbf{x} = \mathfrak{M}(\mathbf{z})$. In general, $M' < M$. For simplicity, we shall restrict our attention initially to linear maps so that

$$\mathbf{x} = \mathbf{M}\mathbf{z}. \tag{3.43}$$

Equation (3.43) may also be written as

$$\mathbf{x} = \sum_{i=1}^{M'} z_i \mathbf{m}_i \tag{3.44}$$

where $z_i = [\mathbf{z}]_i$ is the ith element of the retrieval vector and $\mathbf{m}_i$ is the ith column vector of **M.** The atmospheric state vector is expressed as a linear combination of basis vectors $\mathbf{m}_i$ weighted by retrieval parameters z_i.

We also need an inverse mapping from a full state vector to a retrieval vector, which is described by

$$\tilde{\mathbf{z}} = \mathbf{M}^* \mathbf{x}. \tag{3.45}$$

Under certain conditions the inverse mapping is a pseudo-inverse of the map. These conditions will be described in more detail later.

The Jacobian of the retrieval parameters with respect to the radiances is expressed as

$$\mathbf{K}_z = \frac{\partial \mathbf{L}(\mathbf{Mz})}{\partial \mathbf{z}} \tag{3.46}$$

The chain rule can be applied to Equation (3.46) to give

$$\frac{\partial \mathbf{L}}{\partial \mathbf{z}} = \frac{\partial \mathbf{L}}{\partial \mathbf{x}} \frac{\partial \mathbf{x}}{\partial \mathbf{z}} \tag{3.47}$$

or

$$\mathbf{K}_z = \mathbf{K}_x \mathbf{M}. \tag{3.48}$$

3.5.3.3 Initialization and Update of Retrievals with Maps

The retrieval algorithm estimates the retrieval parameters that best minimize the ML or MAP cost function. The Forward Model, however, works exclusively on the FM pressure grid and can only be evaluated on the atmospheric state vector, $\mathbf{x}$. Therefore a map projects the estimated retrieval parameters to atmospheric state values. This can be done either by projecting the natural log of the atmospheric state values or the values themselves. Typically natural logs are used, although for shape retrievals and atmospheric temperature profiles the values themselves are used. So, for the typical case, an additional exponentiation will be necessary.

To start the retrieval, the initial values of the retrieval parameters must be calculated from the initial atmospheric state vector. The initial retrieval vector is related to the atmospheric state vector through the inverse mapping as described in Equation (3.45), thus

$$\ln(\mathbf{z}_0) = \mathbf{M}^* \ln(\mathbf{x}_{in}). \tag{3.49}$$

The forward model and Jacobian must be calculated on the atmospheric full state vector. Thus the initial guess retrieval vector must be mapped back to an initial guess atmospheric full state vector resulting in

$$\mathbf{x}_0 = \mathbf{M}\mathbf{z}_0 = \mathbf{M}\mathbf{M}^* \mathbf{x}_{in}, \tag{3.50}$$

where $\mathbf{x}_{in}$ is the input atmospheric full state vector. In general, the initial guess atmospheric full state vector is *not* equal to the input atmospheric full state vector, i.e. $\mathbf{M}\mathbf{M}^* \neq \mathbf{I}$.

The update to the retrieval parameters is calculated by solving Equations (3.50). The new atmospheric state vector is then

$$\ln(\mathbf{x}_{i+1}) = \mathbf{M}\ln(\mathbf{z}(1+\delta\mathbf{z})). \tag{3.51}$$

The forward model may now be recalculated at the new atmospheric state vector, $\mathbf{L}(\mathbf{x}_{i+1})$.

3.5.3.4 Nonlinear Maps based on natural log

For several atmospheric species, e.g. ozone, H_2O, the retrieval of the natural log of the volume mixing ratio (VMR) is preferable. In this case,

$$\ln \mathbf{x} = \mathbf{M}\mathbf{z}, \tag{3.52}$$

which results in the following nonlinear maps:

$$\mathfrak{M}(\bullet) = \exp(\mathbf{M}\bullet) \tag{3.53}$$

and

$$\mathfrak{M}^*(\bullet) = \mathbf{M}^* \ln(\bullet). \tag{3.54}$$

The initial guess retrieval vector and the a priori retrieval vector are now calculated as

$$\mathbf{z}_0 = \mathbf{M}^* \ln(\mathbf{x}_{in}) \tag{3.55}$$

3.5.4 A Priori Constraints

A priori is a description of what is known or believed about the state before the measurement is considered. Typically it may comprise a climatological estimate of the state plus some measure of its uncertainty, most conveniently expressed as a covariance matrix. Other possible sources include independent measurements by other observing systems, such as the NCEP analyses or forecasts.

Other constraints that may be used include positivity, and linear inequality and *ad hoc* smoothness constraints. Positivity for constituents may be imposed by using log(mixing ratio) rather than mixing ratio in the state vector. Linear inequality constraints allow physical bounds to be imposed on the range of the state vector elements, such as emissivity [Gill, Murray, and Wright, 1981]. Smoothness can be imposed by adding a quadratic form to the cost function that penalizes the first or second difference of the profile [Twomey 1963, Steck 2002] or by defining correlations between elements of the profile that decay exponentially as a function of distance [Steck, 2001].

The combination of constraints to be used will be determined by the driver table (see Section 3.5.1.1).

3.5.5 Inverse Algorithm

3.5.5.1 The additive noise model and cost function

Measured radiances in TES can be related to a forward model through the following additive noise model:

$$\mathbf{y} = \mathbf{F}(\mathbf{x}) + \mathbf{n} \tag{3.56}$$

where $\mathbf{y} \in \mathbb{R}^N$ which is a real vector of length N, is the calibrated, measured spectrum; $\mathbf{x} \in \mathbb{R}^M$ is the "full" state vector and **b** is a vector containing all the other trace gases, atmospheric temperature profile, geometry of the spacecraft, etc. necessary to define the radiative transfer from the atmosphere to the space craft. The forward model parameter vector **b** will be dropped in the subsequent derivations because these parameters are fixed for the purpose of the retrievals. However, the effects of errors in the forward model parameter vector will be discussed in Section 3.5.7. The forward model operator $\mathbf{F} : \mathbb{R}^M \rightarrow \mathbb{R}^N$ is a discretized version of Equation (3.5) that simulates a spectrum produced from the propagation of radiation through the atmosphere from the Earth to the spacecraft . The noise term $\mathbf{n} \in \mathbb{R}^N$ is assumed to be zero-mean, Gaussian white noise so that the error covariance, $\mathbf{S}_n \triangleq E[\mathbf{n}\mathbf{n}^{\mathrm{T}}]$, is $\mathbf{S}_n = \sigma^2\mathbf{I}$ where $E[\bullet]$ is the expectation operator and σ is the standard deviation of the noise.

Given the additive noise model of the measured radiances, the estimate of the full state vector, **x**, is

$$\hat{\mathbf{x}} = \mathbf{M} \cdot \min_{\mathbf{z}}(C(\mathbf{z})), \tag{3.57}$$

where the cost function is

$$C(\mathbf{z}) = \left\|\mathbf{y} - \mathbf{F}(\mathbf{M}\mathbf{z})\right\|^2_{\mathbf{S}_n^{-1}} + \left\|\mathbf{z} - \mathbf{z}_c\right\|^2_{\mathbf{\Lambda}}. \tag{3.58}$$

The mapping matrix, **M**, is defined in Equation (3.43), $\mathbf{z}_c$ is the constraint vector and $\mathbf{\Lambda}$ is the constraint matrix. The constraint vector and matrix may be based on climatology or smoothness as discussed in Section 3.5.4.

Minimization proceeds iteratively from an initial guess by means of an appropriate numerical method, until convergence is obtained as discussed in Section 3.5.5.3.

3.5.5.2 Numerical Solution

There is a wide range of numerical methods available in the literature designed for minimizing non-linear least-squares functions such as the cost function in Equation (3.57). The basic methods considered here are the Gauss-Newton method and the Levenberg-Marquardt method. Both methods implement Equation (3.58) by iteratively linearizing the cost function in Equation (3.57) with respect to the retrieval vector. We define a step in the retrieval vector as

$$\delta\mathbf{z} = \mathbf{z}_{i+1} - \mathbf{z}_i. \tag{3.59}$$

The Gauss-Newton method consists of iteratively minimizing the cost function linearized about $\mathbf{z}_i$, which can be written as

$$\mathbf{K}'\delta\mathbf{z} = \delta\mathbf{y}' \tag{3.60}$$

where

$$\mathbf{K}' = \begin{bmatrix} \mathbf{S}_n^{-1/2}\mathbf{K}_z(\mathbf{z}_i) \\ \mathbf{\Lambda}^{1/2} \end{bmatrix} \tag{3.61}$$

and

$$\delta\mathbf{y}' = \begin{bmatrix} \mathbf{S}_n^{-1/2}(\mathbf{y} - \mathbf{F}(\mathbf{M}\mathbf{z}_i) \\ \mathbf{\Lambda}^{1/2}(\mathbf{z} - \mathbf{z}_c) \end{bmatrix}. \tag{3.62}$$

The Jacobian, $\mathbf{K}_z$, in Equation (3.61) is defined in Equation (3.46) and related to the full state vector **x** in Equation (3.48). A numerically robust method for calculating a Gauss-Newton iteration to Equation (3.60) is by factoring the augmented Jacobian $\mathbf{K}'$ into the QR decomposition

$$\mathbf{QR}\delta\mathbf{z} = \delta\mathbf{y}', \tag{3.63}$$

where $\mathbf{Q} \in \mathbb{R}^{N\times N}$ is an orthogonal matrix and $\mathbf{R} \in \mathbb{R}^{N\times M}$ is an upper triangular matrix. The orthogonal matrix can be inverted implicitely and the retrieval vector can be calculated by back-solving from **R** [Bjorck,1996]. The forward model is evaluated by the updated full state vector $\mathbf{x}_{i+1} = \mathbf{M}\mathbf{z}_{i+1}$ and Equation (3.60) is solved again until convergence, which is the subject of Section 3.5.5.3.

Alternatively, the least squares solution to Equation (3.60) may also be written as

$$\delta\mathbf{z} = \left(\mathbf{K}'^{\mathrm{T}}\mathbf{K}'\right)^{-1}\mathbf{K}'^{\mathrm{T}}\delta\mathbf{y}' \tag{3.64}$$

or

$$\mathbf{z}_{i+1} = \mathbf{z}_i + (\mathbf{\Lambda} + \mathbf{K}_i^{\mathrm{T}}\mathbf{S}_n^{-1}\mathbf{K}_i)^{-1}(\mathbf{K}_i^{\mathrm{T}}\mathbf{S}_n^{-1}[\mathbf{y} - \mathbf{F}(\mathbf{M}\mathbf{z}_i)] - \mathbf{\Lambda}[\mathbf{z}_i - \mathbf{z}_c]) \tag{3.65}$$

Note that the efficiency of the iteration is enhanced if $\mathbf{S}_n$ is diagonal, particularly for cases where the measurement vector is large, as in the case of TES. However, the apodization of microwindows will introduce off-diagonal elements in $\mathbf{S}_n$ and other sources such as calibration may also cause correlations in the measurement errors. The off-diagonal elements due to apodization are easily calculated and if any other correlations are stable with time, we could perform an inversion of the error correlation matrix on an infrequent basis. This stored matrix could then be scaled using the diagonal measurement errors to provide $\mathbf{S}_n^{-1}$ for each retrieval. The retrieval sensitivity to the accuracy of the off-diagonal elements in $\mathbf{S}_n$ needs to be studied in

order to decide when off-diagonal elements can be neglected and how often the inverted correlation matrix would need to be updated to account for any time variations.

The Gauss-Newton method is satisfactory for *small residual problems* [Fletcher, 1993]. For these problems, the initial guess is in a region sufficiently close to the solution such that non-linearities in the cost function are small, as we hope to have with the initial guess refinement. If the initial guess refinement is not successful, then the Levenberg-Marquardt (LM) method will be used. This algorithm is implemented as a *trust-region* method [More', 1977]. In this method, the cost function in (3.30) is minimized subject to a constraint on the maximum step size, $\|\mathbf{z}_{i+1}-\mathbf{z}_i\| < \delta$. The *trust region radius* δ defines a sphere over which the cost function is considered linear. An LM step is calculated by solving

$$\begin{bmatrix} \mathbf{K}' \\ \gamma_i^{1/2}\mathbf{W} \end{bmatrix} \delta\mathbf{z} = \begin{pmatrix} \delta\mathbf{y}' \\ \mathbf{0} \end{pmatrix} \tag{3.66}$$

with the QR decomposition or alternatively as

$$\mathbf{z}_{i+1} = \mathbf{z}_i + (\gamma_i \mathbf{W}^{\mathrm{T}}\mathbf{W} + \mathbf{\Lambda} + \mathbf{K}_i^{\mathrm{T}}\mathbf{S}_n^{-1}\mathbf{K}_i)^{-1}(\mathbf{K}_i^{\mathrm{T}}\mathbf{S}_n^{-1}[\mathbf{y} - \mathbf{F}(\mathbf{M}\mathbf{z}_i)] - \mathbf{\Lambda}[\mathbf{z}_i - \mathbf{z}_c]) \tag{3.67}$$

where the parameter γ_i is called the LM parameter and $\mathbf{W}$ is a non-zero scaling matrix that permits the minimization over an ellipse rather than a sphere. The LM parameter is varied from step to step according to the strategy described by More':

1. Find γ_i such that the step size is within the trust region radius.
2. Check that $C(\mathbf{z}_{i+1}) < C(\mathbf{z}_i)$. If the update cost function has increased, then reduce the trust region radius and return to step 1.
3. Compare $C(\mathbf{z}_{i+1})$ with its linear approximation, $C_l(\mathbf{z}_{i+1})$.
4. Increase the trust region radius if $C(\mathbf{z}_{i+1}) \sim C_l(\mathbf{z}_{i+1})$ and decrease if $C(\mathbf{z}_{i+1}) >> C_l(\mathbf{z}_{i+1})$.
5. Return to step 1 for next iteration.

3.5.5.3 Convergence Criterion

Stopping criteria provide a set of conditions for which an iterative minimization scheme, such as the Gauss-Newton algorithm, should terminate. These criteria are distinguished from convergence criteria in that satisfying one or more of these conditions do not necessarily imply convergence. Stopping criteria discussed here are one-point and two-point criteria, which depend on the current iteration or the current iteration and the previous iteration, respectively.

We will discuss sufficient conditions for termination of the minimization algorithm. These criteria do not test for convergence *per se*. In addition, we will provide a series of tests for convergence.

3.5.5.3.1 Sufficient condition criteria

The first one-point criterion is the maximum number of iterations:

$$i \le N_{\max} \tag{3.68}$$

where *i* is the iteration number. Clearly, this criterion is a poor indicator of convergence. However, computational restrictions require the use of Equation **Error! Reference source not found.**. The quality of the retrieval can be assessed afterwards. The second one-point criterion is based on the cost function in Equation (3.58):

$$\frac{\sqrt{C(\mathbf{z})}}{\sqrt{\mathbf{N}}} \le 1-\delta \tag{3.69}$$

The value of δ is usually set to be equal to the normalized variance of the χ^2 distribution of the cost function in Equation (3.58) : $\delta = 1/(N+M)$. If the estimates of the covariance of the measurement error are correct, then continuing to iterate after Equation (3.69) has been satisfied will only "fit the noise". Nevertheless, this condition does not indicate whether a local minimum has been reached and hence does not test convergence.

3.5.5.3.2 Tests for convergence

The following criteria are used in conjunction to test for convergence [1,2]

$$\frac{\left\|\mathbf{K}^{\mathrm{T}}\mathbf{r}(\mathbf{z}_i)\right\|_2}{1+C(\mathbf{z}_i)} \le \sqrt{\varepsilon} \tag{3.70}$$

$$\frac{\left\|\mathbf{z}_i-\mathbf{z}_{i-1}\right\|_2}{1+\left\|\mathbf{z}_i\right\|_2} \le \sqrt{\varepsilon} \tag{3.71}$$

$$\frac{\left|C(\mathbf{z}_i)-C(\mathbf{z}_{i-1})\right|}{1+C(\mathbf{z}_i)} \le \varepsilon \tag{3.72}$$

where ε is the threshold value, $\mathbf{K}$ is the Jacobian, and $\mathbf{r}$

$$\mathbf{r}(\mathbf{z}_i) = \begin{pmatrix} \mathbf{S}_n^{-1/2}(\mathbf{y}-\mathbf{F}(\mathbf{z}_i)) \\ \Lambda^{1/2}(\mathbf{z}_i-\mathbf{z}_c) \end{pmatrix} \tag{3.73}$$

is the residual. Equation (3.70) insures that the derivative of the cost function, $\nabla C(\mathbf{z}) = -\mathbf{K}^{\mathrm{T}}\mathbf{r}$ is close to zero, which is a necessary condition for a local minimum. Equations (3.71) and (3.73), which are two-point stopping criteria, check that the fractional change in the state vector and cost function are going to zero. The denominator is augmented by "1+" in order to avoid a divide-by-zero situation. The value of the threshold is based on the accuracy of the Jacobian calculation.

These three condition must be simultaneously satisfied in order for the iterations in the minimization algorithm to terminate. However, Equations (3.68) and (3.69) are sufficient conditions for termination.

3.5.6 Retrieval Microwindow Selection

There are several reasons for using small regions of the spectrum (microwindows) for retrievals, including:

- Reduction in computation, because the forward model only has to generate a small interval.
- Reduction in computation due to fewer fitted parameters
- Reduction of the effect of interfering gases

The spectral size of the microwindows will range from a few wavenumbers to one hundred or more wavenumbers, depending upon the species to be retrieved. In order to achieve the maximum reduction in computing time, both the calculated and observed spectrum need to be apodized. This reduces the ringing of lines, and thus the width of the spectrum required.

Usually, different microwindows will be needed for different altitude regions, and for the nadir and limb. Generally, strong lines will be used for high altitudes, while weak lines will give more information at low altitudes.

There are at least two objective methods for microwindow selection [Rodgers 1996, von Clarmann 1999]. Candidate regions are selected for a species based on known absorption and interferences. The information content for particular points in the interval are evaluated, and selections made to maximize the information. Initial microwindows will be selected using simulated spectra, with expected instrument noise. The microwindows will be revised early in the mission based on real instrument performance.

3.5.7 Error Analysis

3.5.7.1 Linear retrieval

If the estimate is "close" to the true state, then its dependence on the choice of constraint vector, constraint matrix, and true state can be described by the linear retrieval [Rodgers 2000]:

$$\hat{\mathbf{x}} = \mathbf{x}_c + \mathbf{A}_{xx}(\mathbf{x} - \mathbf{x}_c) + \mathbf{M}\mathbf{G}_z\mathbf{n} + \sum_i \mathbf{M}\mathbf{G}_z\mathbf{K}_b^i(\mathbf{b}^i - \mathbf{b}_a^i) \qquad (3.74)$$

where $\mathbf{M}$ is the mapping matrix, $\mathbf{n}$ is the noise vector, $\mathbf{x}$ is the true full state vector, $\mathbf{x}_c = \mathbf{M}\mathbf{z}_c$ is the *a priori* state vector. The vector $\mathbf{b}$ is the true state for those parameters that also affect the modeled radiance, e.g., concentrations of interfering gas(3.74)es, calibration, etc. The vector $\mathbf{b_a}$ is the corresponding *a priori* values for the vector $\mathbf{b}$. The Jacobian, $\mathbf{K}_b = \frac{\partial \mathbf{F}}{\partial \mathbf{b}}$, describes the dependency of the forward model radiance, $\mathbf{F}$, on the vector $\mathbf{b}$. The $\mathbf{G}_z$ is the gain matrix which is defined by:

$$\mathbf{G}_z = \frac{\partial \mathbf{z}}{\partial \mathbf{F}} = \left(\mathbf{K}_z{}^{\mathrm{T}}\mathbf{S}_{\mathrm{n}}^{-1}\mathbf{K}_z + \Lambda_z\right)^{-1}\mathbf{K}_z{}^{\mathrm{T}}\mathbf{S}_{\mathrm{n}}^{-1}. \tag{3.75}$$

The retrieval Jacobian, $\mathbf{K}_z$, is defined in Equation (3.48) and repeated here:

$$\mathbf{K}_z = \frac{\partial \mathbf{F}}{\partial \mathbf{x}}\frac{\partial \mathbf{x}}{\partial \mathbf{z}} = \mathbf{K}_x\mathbf{M}. \tag{3.76}$$

Equation (3.74) is a valid approximation to the minimization of Equation (3.58) when the estimate is close to the true state

$$\mathbf{K}_x[\mathbf{x} - \hat{\mathbf{x}}] \approx \mathbf{F}(\mathbf{x},\mathbf{b}) - \mathbf{F}(\hat{\mathbf{x}},\mathbf{b}) \tag{3.77}$$

The averaging kernel matrix or resolution matrix, $\mathbf{A}_{\mathrm{xx}} = \frac{\partial \hat{\mathbf{x}}}{\partial \mathbf{x}}$ is the sensitivity of the retrieval to the true state of the atmosphere and is computed by the following equation:

$$\mathbf{A}_{\mathrm{xx}} = \frac{\partial \hat{\mathbf{x}}}{\partial \mathbf{x}} = \frac{\partial \hat{\mathbf{x}}}{\partial \mathbf{z}}\frac{\partial \mathbf{z}}{\partial \mathbf{F}}\frac{\partial \mathbf{F}}{\partial \mathbf{x}} = \mathbf{M}\mathbf{G}_z\mathbf{K}_{\mathrm{x}}, \tag{3.78}$$

The averaging kernel matrix is used to define the "resolution" of the retrieval. The vertical resolution of an atmospheric retrieval, defined on a pressure (or altitude grid), can be derived from the rows of the averaging kernel matrix, $\partial \hat{x}_i / \partial \mathbf{x}$, which define the relative contribution of each element of the true state to the estimate at a particular pressure (or altitude). The resolution is then defined as the full-width-half-maximum of the rows of the averaging kernel.

The averaging kernel matrix is also used to compute the degrees of freedom for signal (dofs) of the retrieval [Rodgers 2000], which is defined as:

$$\text{dofs} = \mathrm{tr}[\mathbf{A}_{xx}]. \tag{3.79}$$

The degrees of freedom for signal of the retrieval may be interpreted as the number of statistically independent elements of the estimate.

3.5.7.2 Error Analysis and Information Content

The error in the estimate is defined as the difference between true state and the estimate:

$$\hat{\mathbf{x}} = \mathbf{x} - \hat{\mathbf{x}} \tag{3.80}$$

Substituting Equation (3.74) into Equation (3.81) leads to

$$\hat{\mathbf{x}} - \mathbf{x} = \underbrace{(\mathbf{I} - \mathbf{A}_{xx})(\mathbf{x} - \mathbf{x}_c)}_{\text{smoothing error}} + \underbrace{\mathbf{M}\mathbf{G}_z\mathbf{n}}_{\text{measurement error}} + \underbrace{\sum_i \mathbf{M}\mathbf{G}_z\mathbf{K}_b^i(\mathbf{b}^i - \mathbf{b}_a^i)}_{\text{systematic errors}} \qquad (3.81)$$

The right hand side of this equation is composed of three terms. The first term results from applying constraints to the estimate of retrieval state vector. These constraints can be a combination of "hard" constraints (e.g. representing the profile on a coarse pressure grid), or "soft" constraints (e.g. adding a quadratic penalty function to Equation (3.75)) in order to ensure an acceptable regularization. This first term is the so-called "smoothing" error [Rodgers 2000]. Physically, the smoothing error describes the uncertainty due to un-resolved fine structure. The second term (measurement error) transforms the random instrument spectral error to an error on the full state vector. The third term transforms errors from forward model parameters to an error on the full state vector, for brevity we describe these terms as systematic errors, although some of the errors such as temperature and water can change with each retrieval.

The mean of the error vector defined on the full-state grid (i.e., the grid chosen for the full-state vector) is:

$$E[\hat{\mathbf{x}} - \mathbf{x}] = (\mathbf{I} - \mathbf{A}_{xx})(\bar{\mathbf{x}} - \mathbf{x}_c) \qquad (3.82)$$

where $\bar{\mathbf{x}} = E[\mathbf{x}]$. Equation (3.82) is also the mean of the smoothing error and hence represents the bias introduced by the constraint vector and constraint matrix. In the case where the constraint vector is equal to the mean of the "true" state, then the estimate is un-biased. We have assumed a zero-mean measurement noise vector and systematic error for Equation(3.81). The total error covariance matrix after a measurement has been performed is:

$$\mathbf{S}_{\hat{x}} = (\mathbf{A}_{xx} - \mathbf{I})\mathbf{S}_a(\mathbf{A}_{xx} - \mathbf{I})^T + \mathbf{M}\mathbf{G}_z\mathbf{S}_n\mathbf{G}_z^n\mathbf{M}^T + \sum_i \mathbf{M}\mathbf{G}_z\mathbf{K}_b^i\mathbf{S}_b^i(\mathbf{M}\mathbf{G}_z\mathbf{K}_b^i)^T \qquad (3.83)$$

where $\mathbf{S}_{\hat{x}} = \mathrm{E}[(\hat{\mathbf{x}} - \bar{\hat{\mathbf{x}}})(\hat{\mathbf{x}} - \bar{\hat{\mathbf{x}}})^T]$, $\bar{\hat{\mathbf{x}}} = E[\hat{\mathbf{x}}]$, $\mathbf{S}_a = E[(\mathbf{x} - \bar{\mathbf{x}})(\mathbf{x} - \bar{\mathbf{x}})^T]$, and $\mathbf{S}_b = E[(\mathbf{b} - \bar{\mathbf{b}})(\mathbf{b} - \bar{\mathbf{b}})^T]$. The smoothing error covariance matrix is composed of the averaging kernel and the covariance of the state vector. Hence, the smoothing error will decrease as the resolution of the retrieval increases, i.e., the averaging kernel will approximate the identity matrix. The systematic errors that have been considered are errors from previously retrieved atmospheric trace gas species, atmospheric temperature, surface parameters (surface temperature and emissivity), and spectroscopic line errors. The quantitative description of expected errors for TES nadir retrievals are presented in Worden *et al.*, 2004.

3.6 FINAL FULL SPECTRUM CALCULATION

In order to search for unmodeled species in our data, we will examine the difference between the complete forward model generated from our retrieved atmospheric state and the full TES measured spectrum. The final forward model is calculated using the full state vector constructed from the microwindow retrievals. Unmodeled species will appear as deviations in the residual that are above the noise level and have characteristic spectral features that can be analyzed using techniques such as Fourier analysis, wavelet transforms or spectral matched filtering.

For land nadir views, in order to calculate a residual spectrum, we will also need to retrieve surface spectral emissivity parameters since these cannot be completely provided from the microwindow retrievals. This requires saving the transmission and downwelling radiance from the atmospheric radiative transfer calculation but the Jacobians of the atmospheric parameters would not need to be calculated or stored.

For limb views this full spectrum calculation could become prohibitive if performed for each target. We may therefore only perform it as needed for diagnostics (e.g., TBD per Global Survey). For detection of unmodeled species, the residual calculation could be performed more often but on reduced spectral ranges that are larger than microwindows but smaller than the full filter frequency ranges.

3.7 DATA QUALITY & RESIDUALS

Data quality is assessed at every level of processing (1A, 1B, 2, 3 ....) and the assessments passed forward to all subsequent steps (unless the error halts the Product Generation Executive [PGE]). For completeness, therefore, this section contains all error conditions from all levels, stated in the form of requirements. A full discussion can be found in JPL D-20322: *Science & Operational Algorithm Quality Assessment and Diagnostic Requirements*, V1.2, June 29, 2001.

Note, however, that this section covers only the science requirements. “Software Mechanics” (e.g., exception handling) are treated elsewhere.

3.7.1 Level 1A

1: Data streams with missing packets shall be placed in a holding area and, if the missing packets do not appear within TBD (24) hours, the associated interferograms shall be rejected.

2: Interferograms whose total length is less than expected by TBD (1%) shall be rejected..

3: All interferograms containing absolute DN values in excess of TBD (30,000) shall be flagged as having “possible A-D overflow”.

4: All interferograms containing date or time errors shall be flagged as having “possible date/time error’.

5: The Run Counter is a unique identifier (beginning at 1) for major data blocks such as a 16-orbit Global Survey. It is continuously incremented for the lifetime of the mission.

All interferograms with an erroneous Run Count shall be flagged as having a “run count error” and the PGE halted.

6: The Sequence Counter identifies data granules such as an 81.2 second Global Survey sequence. It is reset at the beginning of each Run.

All interferograms with an erroneous Sequence Count shall be flagged as having a “sequence

count error" and the PGE halted.

7: The Scan Counter identifies the individual scans within a sequence (#7 for a Global Survey sequence) and is reset at the start of each Sequence.

All interferograms with an erroneous Scan Count shall be flagged as having a "scan count error" and processing halted.

8: All interferograms with erroneous filter wheel settings shall be rejected.

9: All interferograms, except for "cold space" calibrations, with maximum absolute DN values less than 16,000 shall be flagged as having "A-D underflow".

10: All interferograms for which persistent indications of either attitude or attitude rate errors are found shall be rejected.

11: All interferograms for which the PCS pitch & roll angles exceed acceptable bounds shall be rejected.

12: All interferograms for which the mean scan speed is outside 1.0559 ∀ 0.317 cm/sec shall be flagged as having an "incorrect scan speed".

13: All interferograms for which the scan direction is not that expected shall be flagged as having an "incorrect scan direction".

14: All interferograms for which the scan speed variations exceed TBD (3%) shall be flagged as having an "excess scan speed variation".

15: All interferograms for which the scan speed variations exceed TBD (4%) shall be rejected.

16: All blackbody calibration interferograms for which the indicated blackbody temperatures are not as expected shall be rejected.

17: All interferograms for which the cold reference plate temperature differs from TBD (180K) by more than TBD (2K) shall be rejected.

18: All interferograms acquired while any instrument temperature has an incorrect or unexpected value but within the "yellow" range shall be flagged as having a "possible instrument temperature out of range".

19: All interferograms acquired while any instrument temperature has an incorrect or unexpected value outside the "yellow" range shall be rejected.

3.7.2 Level 1B

1: All interferograms containing amplitudes more than TBD (10) times greater than neighboring

values (except near Zero Path Difference) shall be flagged as having “possible spikes in interferogram”.

2: Spectra having offsets in excess of TBD (1Φ) shall be flagged as having “significant baseline offset in spectrum”.

3: If the area under the spectrum does not meet expectations within TBD (5%) then the spectrum shall be flagged as having an “incorrect gain or instrument is contaminated”.

4: If the peak brightness temperature does not meet expectations the spectrum shall be flagged as “probable cloud or aerosol in the field of view”.

5: If the nadir pixel-to-pixel brightness temperature variations exceed TBD (1K) then the PGE shall be halted and the data flagged as having “excess inter-pixel variability”.

6: If correlation tests on the imaginary part of the spectrum following phase correction show unexplained peaks in excess of TBD (5Φ) the spectrum shall be rejected.

7: Spectra having NESRs more than TBD (5%) above expectations shall be flagged as having “excess noise or reduced signal”.

3.7.3 Level 2

1: Retrievals that do not converge in TBD (3) iterations shall be stopped and rejected.

2: If the final retrieval step size is greater than TBD (0.1%) of the parameter value the retrieval shall be flagged as having “probable convergence failure” and the parameter name logged.

3: Retrievals that converge with a significance level greater than TBD (99%) shall be flagged as having a ‘‘significant disagreement with the measurement’’, and the parameter name logged.

4: If a full climatology is available for a particular species then retrievals with a significance level greater than TBD (99%), shall be flagged as having a ‘‘significant disagreement with the climatology’’.

5: Retrievals that go negative or show unsatisfactory smoothness (“jack-knifing”) in which consecutive values in a profile oscillate about a mean by more than TBD (3Φ) shall be flagged as having “negative or jack-knifed profile”.

6: Retrievals wherein the trace of the Averaging Kernel matrix is less than TBD (1) shall be flagged as having ‘‘little information content’’.

7: Retrievals exhibiting peak residuals (spectrum - final forward model) greater than TBD (5Φ) above the RMS noise level shall be flagged as having “excess error propagation or unmodeled species”.

8: Residuals having a mean offset greater than TBD (1Φ) shall be flagged as having "significant offset in the mean residual".

3.7.4 Level 3

9: Associated limb and nadir retrievals that differ by more than TBD (2x the sum of the error bars) shall be flagged as having "inconsistent limb & nadir profiles" and the parameter name logged.

3.7.5 Archiving

Observations that complete all stages with acceptable flags will be released to the archive. The data will be accompanied by the diagnostics described in Section 2.

4 ALGORITHM VERIFICATION

4.1 END-TO-END CLOSURE EXPERIMENTS

The purpose of the end-to-end closure experiments using the TES reference and operational software is to test the robustness of TES level 2 retrieval algorithms and the operational software and to identify any problems either in the algorithm or in coding. This procedure will also be helpful for algorithm validations. A single step end-to-end simulation would be to add noise to the model radiance and then to execute a step retrieval defined in the TES retrieval strategies. A full end-to-end closure experiment would be to generate a full four-day global survey set of radiances with added noise and clouds and then to carry out the four-day retrieval processing.

Establishing a profile/parameter database which consists collections of measured atmospheric temperature and constituent profiles and surface parameter data by all means of observations, sonde, balloon, aircraft, satellite, etc. is one of the key activities for the pre-launch closure experiments. These profiles/parameters along with model simulated profiles allow us to compile the baseline initial guesses and the *a priori* (see Sections 3.5.2.1 and 3.5.2.3), to simulate the observed spectral radiance, and to evaluate the retrieval results for all the possible atmospheric conditions including extreme cases. Global cloud coverage data will also be obtained so that the simulated TES global pixel measurements will be more realistic.

The end-to-end closure experiments will follow three procedures: (1) simulate the TES observations using collected measurement profiles/surface parameters/cloud coverage as the true atmospheric full state with added noise, (2) generate TES retrieval products using a defined initial guess, and (3) examine and evaluate the retrieval results and error analysis by comparing with the "smoothed true profiles" and their statistical variance. Since the level 2 software will be developed in steps from a single profile retrieval to automated four-day data retrieval, the end-to-end experiment can be performed at each step.

4.2 VALIDATION

Validation, in the sense used here, differs from validation of the TES measurements in that we will use pre-existing data that have already been analyzed by others. The objective is to ensure that the TES algorithm either produces identical results or there are plausible reasons why it does not. Measurement validation will employ near-concurrent and co-located measurements and is not further discussed in this document (although, of course, it is a crucial part of the overall TES experiment).

Data sources currently identified that are (or will be) appropriate for this purpose are

1) Airborne Emission Spectrometer (AES). AES operates in both a downlooking mode from a variety of aircraft and uplooking from the surface. It was specifically designed to cover the same spectral region at the same resolution as TES and is therefore a prime data source for validation exercises. Downlooking data are very similar to the TES nadir mode and uplooking data are a useful surrogate for TES limb data.

2) AERI (Atmospheric Emitted Radiation Interferometer). AERI is a well calibrated, 1 cm^{-1} spectral resolution, uplooking , Michelson interferometer covering the range 550 to 1700 and 2000 to 2500 cm^{-1}. Several copies of the instrument are operational – the one of primary interest for TES validation is located at the Central facility of the ARM Cloud And Radiation Test (CART) site in northern Oklahoma. The AERI-X (eXtended resolution AERI) is also located at the central facility. It has 0.1 cm^{-1} spectral resolution, but only covers 550 to 1600 cm^{-1}. The ARM program provides good temperature and water vapor information about the atmosphere overhead. Information about ozone and other stratospheric gases, as well as aerosol optical depth, is available from solar absorption instruments at the site.

3) HIS (High resolution Interferometric Sounder). HIS is an autonomous FTS that flies on the ER2 in a variety of campaigns with the goal of temperature and water vapor sounding. Some of the more recent campaigns have been in support of tropospheric chemistry missions, where independent measurements may also be available. Although the spectral resolution is lower, the data are from an altitude that is more "space-like" than the AES data.

4) IMG (Interferometric Monitor of Greenhouse Gases). IMG, a nadir sounder developed by the Japanese, flew on the ADEOS mission (which failed in June 1997). Nevertheless, it represents the only available source of real space-based data with spectral coverage and resolution very close to that of TES. Some tests using IMG data are already ongoing and more are planned.

5) MIPAS (Michelson Interferometer for Passive Atmospheric Sounding). MIPAS will fly on the ENVISAT mission at least one year before TES. It is a limb sounder with slightly poorer spectral resolution than TES but will nevertheless be the only available source of space-based limb emission data prior to TES, so it will be a very valuable validation tool.

6) NAST-I (NPOESS Aircraft Sounder Testbed – Interferometer). NAST-I is a nadir-viewing instrument that has flown on several ER2 missions, including CAMEX-3, with correlative radiosonde measurements. It has a spectral resolution of 0.25 cm^{-1} covering the spectral regime 590-2810 cm^{-1}. As a testbed to the NPOESS candidate instruments, it has been used to simulate "space-like" ground coverage views for the validation of key meteorological species.

5 REFERENCES

1 INTRODUCTION

Execution Phase Project Plan for the Earth Observing System (EOS). GSFC 170-01-01, Rev. A, May 1995.

Mission to Planet Earth Strategic Enterprise Plan 1996-2002. NASA HQ MTPE, May 1996.

Tropospheric Emission Spectrometer: Scientific Objectives & Approach, Goals & Requirements. JPL D-11294, Rev. 5.0, May 1996.

2 BACKGROUND

Rothman, L.S., C.P. Rinsland, A. Goldman, S.T. Massie, D.P. Edwards, J.-M. Flaud, A. Perrin, C. Camy-Peyret, V. Dana, J.-Y. Mandin, J. Schroeder, A. McCann, R.R. Gamache, R.B. Wattson, K. Yoshino, K.V. Chance, K.W. Jucks, L.R. Brown, V. Nemtchinov, and P. Varanasi, The HITRAN Molecular Spectroscopic Database and HAWKS (HITRAN Atmospheric Workstation): 1996 Edition, *J. Quant. Spectrosc. Radiat. Transfer*, *60,* 665-710, 1998.

TES Level 1B ATBD, JPL D-16479, October 1, 1999.

3 ALGORITHM DESCRIPTION

3.1 ALGORITHM OVERVIEW

TES Level 1B Algorithm Theoretical Basis Document, JPL D-16479, 1999.

3.2.4 Spectral Grids

Clough, S.A. and F.X. Kneizys, Convolution algorithm for the lorentz function. *Applied Optics, 18,* 2329, 1979.

3.3.1.6 Atmospheric Radiance

Clough, S.A., M.J. Iacono, and J.-L. Moncet, Line-by-line calculation of atmospheric fluxes and cooling rates: Application to water vapor. *J. Geophys. Res., 97,* 15761-15785, 1992.

3.3.1.8 Radiative Transfer for the Solar Contribution

Rinsland, C.P., G.K. Yie, M.R. Gunson, R. Zander, and M.C. Abrams, Mid-infrared extinction by sulfate aerosols from the Mt. Pinatubo eruption*, J. Quant. Spectrosc. Radiat. Transfer, 52,* 241-252, 1994.

3.3.1.9 Surface Contribution

Chandrasekhar, S., *Radiative Transfer*, Dover Publications, 1960.

Goody, R.M and Y.L. Yung, *Atmospheric Radiation, Theoretical Basis,* Second Edition, Oxford University Press, 1989.

3.3.2.1 Surface Radiative Properties

Smith, W. L., R. O. Knuteson, H. E. Revercomb, W. Feltz, H.B. Howell, W.P. Menzel, N. Nalli, O. Brown, J. Brown, P. Minnett, and W. McKeown, Observations of the Infrared Radiative Properties of the Ocean - Implications for the Measurement of Sea Surface Temperature via Satellite Remote Sensing, *Bull. Amer. Meteor. Soc.,* January 1996.

Masuda, K.T., Takashima and Y. Takayama: Emissivity of pure and sea waters for the model sea surface in the infrared window regions, *Remote Sens. Environ., 24,* 313-329, 1988.

Wu, X. and W.L. Smith, "Emissivity of rough sea surface for 8-13 um: modeling and verification", *Appl. Opt.* 36, 2609-2619, 1997.

3.3.3 Radiative Transfer for Clouds and Aerosols

G. Echle, T. von Clarmann, H. Oelhaf, 1998, Optical and microphysical parameters of the Mt. Pinatubo aerosol as determined from MIPAS-B mid-IR limb emission spectra, *J. Geophys. Res*, D15, 19193-19211.

Moncet, J.-L. and S.A. Clough (1997): Accelerated monochromatic radiative transfer for scattering atmospheres: Application of a new model to spectral radiance observations. *J. Geophys. Res.,* 102, 21,853-21,866.

3.3.4 Solar Source Function

Gunson, M.R., M.M. Abbas, M.C. Abrams, M. Allan, L.R. Brown, T.L. Brown, A.Y. Chang, A. Goldman, F.W. Irion, L.L. Lowes, E. Mahieu, G.L. Manney, H.A. Michelsen, M.J. Newchurch, C.P. Rinsland, R.J. Salawitch, G.P. Stiller, G.C. Toon, Y.L. Yung, and R. Zander, The Atmospheric Trace Molecule Spectroscopy (ATMOS) experiment: Deployment on the ATLAS Space Shuttle missions, *Geophys. Res. Lett., 23*, 2333-2336, 1996.

Kurucz, R.L., The solar spectrum: Atlases and line identifications, in *Laboratory and Astronomical High Resolution Spectra, 81*, edited by A.J. Sauval, R. Blomme, and N. Grevesse, Astron. Soc. of the Pacific Coast, 17-31, 1995.

Kurucz, R.L., Synthetic infrared spectra, in *Infrared Solar Physics, IAU Symp. 154,* edited by D.M. Rabin and J.T. Jefferies, Kluwer Acad., Norwell, MA, 1992a.

Kurucz, R.L., Atomic and molecular data for opacity calculations, *Revista Mexicana de Astronomia y Astrofisica, 23*, 45-48, 1992b.

Kurucz, R.L., Finding the missing solar ultraviolet opacity, *Revista Mexicana de Astronomia y Astrofisica, 23*, 181-186, 1992c.

Kurucz, R.L., Remaining line opacity problems for the solar spectrum, *Revista Mexicana de Astronomia y Astrofisica, 23*, 187-194, 1992d.

Kurucz, R.L., I. Furenlid, J. Brault, and L. Testerman, *Solar Flux Atlas from 296 to 1300 nm*, 240 pp., National Solar Observatory, Sunspot, New Mexico, 1984.

3.3.5 Instrumental Line Shape Spectral Convolution and Apodization

Bowman, K. W, H. M. Worden, and R. Beer, Instrument line-shape modeling and correction for off-axis detectors in Fourier-transform spectrometry, *Applied Optics*, *39*, 3765-3773, 2000.

Beer, R. et al."Instrument Calibration Report, Volumes 1 & 2",
JPL Internal Document, D-26533, September 2003.

Gallery, W. O, and S. A. Clough, FFTSCAN: A program for spectral smoothing using Fourier transforms. PL-TR-92-2131, Phillips Laboratory, Hanscom AFB, MA 01731-3010.

Norton, R. and R. Beer, New apodizing functions for Fourier spectrometry, *J. Opt. Soc. Am*. *66*, 259-264, 1976.

3.3.7.1 ABSCO Table Generation (Using LBLRTM)

Anderson, G.P., S.A. Clough, F.X. Kneizys, J.H. Chetwynd, and E.P. Shettle, *AFGL atmospheric constituent profiles (0-120 km). AFGL-TR-86-0110,* 1986.

National Aeronautics and Space Administration, (1976). *U.S. Standard Atmosphere Supplements*, U.S. Government Printing Office, Washington, D.C., 1976.

3.3.7.2 TES Line-by-Line Optical Depth Code

Armstong, B. H., Spectrum line profiles: The Voigt Function, *J. Quant. Spect. Rad. Trans., 7,* 61-88, 1967.

Clough, S.A. and M.J. Iacono (1995): Line-by-Line Calculations of Atmospheric Fluxes and Cooling Rates II: Application to Carbon Dioxide, Ozone, Methane, Nitrous Oxide, and the Halocarbons. *J. Geophys. Res., 100,* 16,519-16,535.

Clough, S.A., M.J. Iacono, and J.-L. Moncet, Line-by-line calculation of atmospheric fluxes and cooling rates: Application to water vapor. *J. Geophys. Res., 97,* 15761-15785, 1992.

Hoke, M. L., S. A. Clough, W. Lafferty, and B. Olson, Line coupling in oxygen and carbon dioxide, in *IRS '88: Current Problems in Atmospheric Radiation*, edited by J. Lenoble and J. F. Geleyn, pp. 368-370, A. Deepak Publishing, Hampton,VA, 1989.

Mlawer, E.J., S.J. Taubman, P.D. Brown, M.J. Iacono and S.A. Clough, Radiative Transfer for Inhomogeneous Atmospheres: RRTM, a Validated correlated-k model for the longwave. *J. Geophys. Res., 102, 16*,663-16,682, 1997.

Rothman, L. S., R. R. Gamache, R. Tipping, C. P. Rinsland, M. A. H. Smith, D. C. Benner, V. Malathy Devi, J.-M. Flaud, C. Camy-Peyret, A. Goldman, S. T. Massie, L. R. Brown, and R. A.

Toth, HITRAN molecular database: Edition of 1991 and 1992, *J. Quant. Spectrosc. Radiat. Transfer, 48,* 469-507, 1992.

Strow, L.L., D. C. Tobin, and S. Hannon, A compilation of first-order line mixing coefficients for CO2 Q-branches, *J. Quant. Spect. Rad. Trans., 52,* 281-294, 1994.

Tjemkes, S.A., T. Patterson, R. Rizzi, M.W. Shephard, S.A. Clough, M. Matricardi, J. Haigh, M. Hopfner, S. Payan, A. Trotsenko, N. Scott, P. Rayer, J. Taylor, C. Clerbaux, L.L. Strow, S. DeSouza-Machado, D. Tobin, and R. Knuteson, The ISSWG Line-by-line Intercomparison Experiment, *Submitted to J. Quant. Spect. Rad. Trans,* 2002.

Tobin, D. C., F. A. Best, P. D. Brown, S. A. Clough, R. G. Dedecker, R. G. Ellingson, R. K. Garcia1, H. B. Howell, R. O. Knuteson, E. J. Mlawer, H. E. Revercomb, J. F. Short, P. F. W van Delst, and V. P. Walden, Downwelling Spectral Radiance Observations at the SHEBA Ice Station: Water Vapor Continuum Measurements from 17-26 micrometer*, J. Geophys. Res*., 1999, in press.

3.3.8 ABSCO Databases

National Aeronautics and Space Administration, (1976). *U.S. Standard Atmosphere Supplements*, U.S. Government Printing Office, Washington, D.C., 1976.

3.3.8.1 Line Parameters

Brown, L. R., M. R. Gunson, R. A. Toth, F. W. Irion, C. P. Rinsland, and A. Goldman, The 1995 Atmospheric Trace Molecule Spectroscopy (ATMOS) Linelist. *Appl. Opt.*, *35*, 2828-2848, 1996.

Rothman, L.S., C.P. Rinsland, A. Goldman, S.T. Massie, D.P. Edwards, J.-M. Flaud, A. Perrin, C. Camy-Peyret, V. Dana, J.-Y. Mandin, J. Schroeder, A. McCann, R.R. Gamache, R.B. Wattson, K. Yoshino, K.V. Chance, K.W. Jucks, L.R. Brown, V. Nemtchinov, and P. Varanasi, The HITRAN Molecular Spectroscopic Database and HAWKS (HITRAN Atmospheric Workstation): 1996 Edition, *J. Quant. Spectrosc. Radiat. Transfer*, *60,* 665-710, 1998.

3.3.8.2 Cross-Sections

Ballard, J., W.B. Johnston, M.R. Gunson, and P.T. Wassel, Absolute absorption coefficients of $ClONO_2$ infrared bands at stratospheric temperatures, *J. Geophys. Res. 93*, 1659-1665, 1988.

Camy-Peyret, C., J.-M. Flaud, L. Lechuga-Fossat, C. Laverdet and G. Le Bras, The Absorption of Gaseous Dinitrogen Pentoxide in the 8.1 and 5.7 μm Spectral Regions, *Chem. Phys. Lett. 139*, 345-349, 1987.

Clerbaux, C., R. Colin, P.C. Simon and C. Granier, Infrared Cross Sections and Global Warming Potentials of 10 Alternative Hydrohalocarbons, *J. Geophys. Res. 98*, 10491-10497, 1993.

Cantrell, C.A., J.A. Davidson, A.H. McDaniel, R.E. Shetter, and J.G. Calvert, *Chem. Phys. Lett. 148*, 358-363, 1988; Erratum *Chem. Phys. Lett. 152*, 274, 1988.

Jacquinet-Husson, N., E. Arièl, J. Ballard, A. Barbe, L.R. Brown, B. Bonnet, C. Camy-Peyret, J.P. Champion, A. ChÈdin, A. Chursin, C. Clerbaux, G. Duxbury, J.M. Flaud, N. FourriÈ, A. Fayt, G. Graner, R. Gamache, A. Goldman, Vl. Golovko, G. Guelachvilli, J.M. Hartmann, J.C. Hillico, G. LefËvre, O.V. Naumenko, V. Nemtchinov, D.A. Newnham, A. Nikitin, J. Orphal, A. Perrin, D.C. Reuter, L. Rosenmann, L.S. Rothman, N.A. Scott, J. Selby, L.N. Sinitsa, J.M. Sirota, A.M. Smith, K.M. Smith, Vl.G. Tyuterev, R.H. Tipping, S. Urban, P. Varanasi, M. Weber, The 1997 Spectroscopic GEISA Databank, *J. Quant. Spectrosc. Radiat. Transfer*, in press, 1998.

Li, Z., and P. Varanasi, Measurement of the Absorption Cross-Sections of CFC-11 at Conditions Representing Various Model Atmospheres, *J. Quant. Spectrosc. Radiat. Transfer, 52,* 137-144, 1994.

Massie, S.T., A. Goldman, D.G. Murcray and J.C. Gille, Approximate absorption cross sections of F12, F11, $ClONO_2$, HNO_3, CCl_4, CF_4, F21, F113, F114, and HNO_3, *Appl. Opt., 24*, 3426-3427, 1985.

Massie, S.T., A. Goldman, A.H. McDaniel, C.A. Cantrell, J.A. Davidson, R.E. Shetter, and J.G. Calvert, Temperature Dependent Infrared Cross Sections for CFC-11, CFC-12, CFC-13, CFC-14, CFC-22, CFC-113, CFC-114, and CFC-115, *NCAR Technical Note/TN-358+STR*, 1991.

Massie, S.T., and A. Goldman, Absorption Parameters of very Dense Molecular Spectra for the HITRAN Compilation, *J. Quant. Spectrosc. Radiat. Transfer, 48*, 713-719, 1992.

McDaniel, A.H., C.A. Cantrell, J.A. Davidson, R.E. Shetter, and J.G. Calvert, The Temperature Dependent, Infrared Absorption Cross-Sections for the Chlorofluorocarbons: CFC-11, CFC-12, CFC-13, CFC-14, CFC-22, CFC-113, CFC-114, and CFC-115, *J. Atmos. Chem., 12*, 211-227, 1991.

Orlando, J.J., G.S. Tyndall, A. Huang, and J.G. Calvert, Temperature Dependence of the Infrared Absorption Cross Sections of the Carbon Tetrachloride, *Geophys. Res. Lett., 19*, 1005-1008, 1992.

Orphal, J., M. Morillon-Chapey, and G. Guelachvili, High-Resolution Absorption Cross Sections of Chlorine Nitrate in the ν_2 Band Region Around 1292 cm^{-1} at Stratospheric Temperatures, *J. Geophys. Res., 99*, 14,549-14,555, 1994.

Rothman, L.S., C.P. Rinsland, A. Goldman, S.T. Massie, D.P. Edwards, J.-M. Flaud, A. Perrin, C. Camy-Peyret, V. Dana, J.-Y. Mandin, J. Schroeder, A. McCann, R.R. Gamache, R.B. Wattson, K. Yoshino, K.V. Chance, K.W. Jucks, L.R. Brown, V. Nemtchinov, and P. Varanasi, The HITRAN Molecular Spectroscopic Database and HAWKS (HITRAN Atmospheric Workstation): 1996 Edition, *J. Quant. Spectrosc. Radiat. Transfer*, *60,* 665-710, 1998.

Smith, K., D. Newnham, M. Page, J. Ballard, and G. Duxbury, Infrared Band Strengths and Absorption Cross-Sections of HFC-32 Vapor, *J. Quant. Spectrosc. Radiat. Transfer, 56*, 73-82, 1996.

Smith, K., D. Newnham, M. Page, J. Ballard, and G. Duxbury, Infrared Absorption Cross-Sections and Integrated Absorption Intensities of HFC-134 and HFC-143a Vapour, *J. Quant. Spectrosc. Radiat. Transfer, 59*, 437-451, 1998.

Varanasi, P., A. Gopalan, and J.F. Brannon Jr., Infrared Absorption Coefficient Data on SF_6 Applicable to Atmospheric Remote Sensing, *J. Quant. Spectrosc. Radiat. Transfer, 48*, 141-145, 1992a.

Varanasi, P., Absorption Coefficients of CFC-11 and CFC-12 needed for Atmospheric Remote Sensing and Global Warming Studies, *J. Quant. Spectrosc. Radiat. Transfer, 48*, 205-219, 1992b.

Varanasi, P., Absorption Spectra of HCFC-22 around 829 cm^{-1} at Atmospheric Conditions, *J. Quant. Spectrosc. Radiat. Transfer, 47*, 251-255, 1992c.

Varanasi, P., and V. Nemtchinov, Thermal Infrared Absorption Coefficients of CFC-12 at Atmospheric Conditions, *J. Quant. Spectrosc. Radiat. Transfer, 51*, 679-687, 1994.

Varanasi, P., Z. Li, V. Nemtchinov, and A. Cherukuri, Spectral Absorption-Coefficient Data on HCFC-22 and SF_6 for Remote-Sensing Applications, *J. Quant. Spectrosc. Radiat. Transfer, 52*, 323-332, 1994.

Goody, R.M and Y.L. Yung, *Atmospheric Radiation, Theoretical Basis,* Second Edition, Oxford University Press, 1989.

3.3.8.3 Aerosols

Massie, S. T., Indices of refraction for the HITRAN compilation, *J. Quant. Spectrosc. Radiat. Transfer, 52,* 501-513, 1994.

Rinsland, C. P., G. K. Yue, M. R. Gunson, R. Zander, and M. C. Abrams, Mid-infrared extinction by sulfate aerosols from Mt. Pinatubo eruption*, J. Quant. Spectrosc. Radiat. Transfer, 52,* 241-252, 1994.

Rothman, L.S., C.P. Rinsland, A. Goldman, S.T. Massie, D.P. Edwards, J.-M. Flaud, A. Perrin, C. Camy-Peyret, V. Dana, J.-Y. Mandin, J. Schroeder, A. McCann, R.R. Gamache, R.B. Wattson, K. Yoshino, K.V. Chance, K.W. Jucks, L.R. Brown, V. Nemtchinov, and P. Varanasi, The HITRAN Molecular Spectroscopic Database and HAWKS (HITRAN Atmospheric Workstation): 1996 Edition, *J. Quant. Spectrosc. Radiat. Transfer*, *60,* 665-710, 1998.

3.3.8.4MT_CKD Continuum

Clough, S. A., F. X. Kneizys, and R. W. Davies: Line shape and the water vapor continuum, *Atmos. Res., 23,* 229-241, 1980.

Clough, S.A. and M.J. Iacono, Line-by-Line Calculations of Atmospheric Fluxes and Cooling Rates II: Application to Carbon Dioxide, Ozone, Methane, Nitrous Oxide, and the Halocarbons. *J. Geophys. Res., 100,* 16,519-16,535, 1995.

Clough, S.A., The water vapor continuum and its role in remote sensing, *in Optical Remote Sensing of the Atmosphere, Vol. 2, 1995, OSA Technical Digest Series ,* Optical Society of America, Washington, DC, pp. 76-81, 1995.

Clough, S.A., M.J. Iacono, J.-L. Moncet, Line-by-Line Calculation of Atmospheric Fluxes and Cooling Rates: Application to Water Vapor. *J. Geophys. Res., 97,* 15761-15785, 1992.

Clough, S.A., F.X. Kneizys, and R. W. Davies, Line shape and the water vapor continuum. *Atmospheric Research, 23,* 229-241, 1989.

Han, Y., J.A. Shaw, J.H.Churnside, P.D. Brown and S. A. Clough, Infrared spectral Radiance measurements in the tropical Pacific atmosphere, *J. Geophys. Res.,102,* 4,353-4,356, 1997.

Lafferty, W.J., A.M. Solodov,A. Weber, W.B. Olson and J._M. Hartmann, Infrared collision-induced absorption by N_2 near 4.3 microns for atmospheric applications: measurements and empirical modeling, Appl. Optics, 35, 5911-5917, (1996).

Mlawer, E.J., S.A. Clough, and D.C. Tobin, A new water vapor continuum: MT_CKD, in preparation, 2003.

Thibault, F., V. Menoux, R. Le Doucen, L. Rosenman, J.-M. Hartmann, and Ch. Boulet Infrared collision-induced absorption by O_2 near 6.4 microns for atmospheric applications: measurements and empirical modeling, *Appl. Optics, 35,* 5911-5917, 1996.

Tobin, D.C., F.A. Best, P.D. Brown, S.A. Clough, R.G. Dedecker, R.G. Ellingson, R.K. Garcia, H.B. Howell, R.O. Knuteson, E.J. Mlawer, H.E. Revercomb, J.F. Short, P.F. van Delst, and V.P. Walden, Downwelling Spectral Radiance Observations at the SHEBA Ice Station: Water Vapor Continuum Measurements from 17-26 micrometer, *J. Geophys. Res*., **104***,* 2081-2092, 1999.

Tobin, D.C., L.L. Strow, W.J. Lafferty and W.B. Olson, Experimental investigation of the self- and N_2-broadened continuum within the ν_2 band of water vapor, *Appl. Opt., 35,* 4274-4734, 1996.

3.5 RETRIEVAL

Fletcher, R., *Practical Methods of Optimization, 2nd Edition*, John Wiley & Sons, 1993.

Gill, P. E., W. Murray, and M. H. Wright, *Practical Optimization,* Academic Press, 1981.

Lambert, A., R.G. Grainger, J.J. Remedios, W.J. Reburn, C.D. Rodgers, F.W. Taylor, J.L. Mergenthaler, J.B. Kumer, S.T. Massie and T. Deshler, Validation of Aerosol Measurements by the Improved Stratospheric And Mesospheric Sounder, *J. Geophys. Res*., *101*, 9811-9830, 1996.

Press, W. H., B. P. Flannery, S. A. Teukolsky, and W. T. Vetterling, *Numerical Recipes*, Cambridge University Press, New York, 1989.

Twomey, S. On the numerical solution of Fredholm integral equations of the first kind by the inversion of the linear system produced by quadrature. *J. Ass. Comput. Mach*., *10*, p 97, 1963.

Wylie, D.P., W.P. Menzel, H.M. Woolf, and K.I. Strabala: Four Years of Global Cirrus Cloud Statistics Using HIRS. *J. Climate*, *7*, 1972-1986, 1994.

3.5.1.4 Initial Guess Refinement

Bowman, K. W., Worden, J.R., Steck, T., Worden, H.M., Clough, S.A., Rodgers, C.D., "Capturing Time and Vertical Variability of Tropospheric Ozone: A Study using TES Nadir Retrievals", JGR-Atmospheres, in press

Clough S. A., Worden, J.R., Brown, P.D., Shepard, M.W., Rinsland, C.P., Beer,R. "Retrieval of tropospheric ozone from simulations of limb spectral radiances as observed from space.", JGR-atmospheres, in press

3.5.1.5 Strategy for Limb Pointing Retrieval

Anderson, G.P., S.A. Clough, F.X. Kneizys, J.H. Chetwynd, and E.P. Shettle*, AFGL atmospheric constituent profiles (0-120 km). AFGL-TR-86-0110*, 1986.

3.5.1.6 Pixel Categorization for Nadir

Wylie, D.P., W.P. Menzel, H.M. Woolf, and K.I. Strabala, 1994: Four Years of Global Cirrus Cloud Statistics Using HIRS. *J. Climate*, **7**, 1972-1986.

Ackerman, S.A., K. Strabala, W.P. Menzel, R.A. Frey, C.C. Moeller and L.E. Gumley, "Discriminating clear sky from clouds with MODIS", *J. Geophys. Res*., 103, 32141-32157, 1998

3.5.2 Operational Support Products

Horowitz, L., et al., A global simulation of tropospheric ozone and related tracers: Description and evaluation of MOZART, version 2, *J. Geophys. Res., 108(D24)*, 4784, doi:10.1029/2002JD002853, 24 December 2003.

Global Modeling and Assimilation Office, Goddard Space Flight Center, Greenbelt, Maryland, File Specification for GEOS-DAS Gridded Output Version 5.3, March 30, 2004.

3.5.4 A Priori Constraints

T. Steck, "Methods for determining regularization for atmospheric retrieval problems",

Applied Optics, Vol. 41, No. 9, March 2002. pp 1788.

T. Steck and T. von Clarmann, "Constrained profile retrieval applied to the observation mode of the Michelson Interferometer for Passive Atmospheric Sounding".
Applied Optics, Vol. 40, No. 21, pp 3559

3.5.5.1 The additive noise model and cost function

Papoulis, A., *Probability, Random Variables, and Stochastic Processes*, McGraw-Hill, New York, 1984.

.3.5.5.2 Numerical Solution

Moré, J. Jorge, The Levenberg-Marquardt Algorithm: Theory and Implementation*, Numerical Analysis: Proceedings, Biennial Conference*, Dundee, 1977.

Marquardt, D., An algorithm for least squares estimation of nonlinear parameters., J. Soc. Indust. Appl. Math 11:431-441,1963.

3.5.5.3 Convergence Criterion

Richard Aster, Brian Borchers, and Clifford Thurber. *Parameter Estimation and Inverse Problems,* Academic Press, 2004.

Stephen Nash and Ariela Sofer. *Linear and Nonlinear Programming.* McGraw-Hill, New York, 1996.

3.5.6 Retrieval Microwindow Selection

Rodgers, C. D. Information content and optimisation of high spectral resolution measurements, SPIE, Vol *2830*, *Optical Spectroscopic Techniques and Instrumentation for Atmospheric and Space Research II*, Paul B. Hays and Jinxue Wang, eds., 136-147, 1996.

von Clarmann, T and G. Echle, Selection of optimized microwindows for atmospheric spectroscopy, *Appl Opt.*, *37*, 7661-7669, 1998.

3.5.7 Error Analysis

Worden, J., S. S. Kulawik, M. W. Shephard, S. A. Clough, H. Worden, K. Bowman, and A. Goldman (2004), Predicted errors of tropospheric emission spectrometer nadir retrievals from spectral window selection, *J. Geophys. Res.*, *109*, D09308, doi:10.1029/2004JD004522.